X-ray tomography and serial sectioning investigation of creep damage in copper

Kévin Abbasi

▶ **To cite this version:**

Kévin Abbasi. X-ray tomography and serial sectioning investigation of creep damage in copper. Other. Ecole Nationale Supérieure des Mines de Saint-Etienne, 2013. English. NNT : 2013EMSE0706 . tel-00966919

HAL Id: tel-00966919

https://theses.hal.science/tel-00966919

Submitted on 27 Mar 2014

HAL is a multi-disciplinary open access archive for the deposit and dissemination of scientific research documents, whether they are published or not. The documents may come from teaching and research institutions in France or abroad, or from public or private research centers.

L'archive ouverte pluridisciplinaire **HAL**, est destinée au dépôt et à la diffusion de documents scientifiques de niveau recherche, publiés ou non, émanant des établissements d'enseignement et de recherche français ou étrangers, des laboratoires publics ou privés.

Ecole Nationale Supérieure des Mines
SAINT-ETIENNE

NNT : 2013 EMSE 0706

THÈSE

présentée par

Kévin ABBASI

pour obtenir le grade de
Docteur de l'École Nationale Supérieure des Mines de Saint-Étienne

Spécialité : Sciences et Génie des Matériaux

ETUDE DE L'ENDOMMAGEMENT EN FLUAGE DE CUIVRE PAR TOMOGRAPHIE A RAYONS X ET POLISSAGES SUCCESSIFS

soutenue à Saint-Etienne, le 4 Octobre 2013

Membres du jury

Président :	Yves BIENVENU	Professeur, Mines ParisTech
Rapporteurs :	Eric MAIRE	Directeur de recherche, INSA de Lyon
	Guillermo REQUENA	Professeur, TU Wien, Autriche
Examinateur(s) :	Nathalie GEY	Chargé de recherche, Université de Lorraine
Directeur(s) de thèse :	András BORBELY	Maitre de recherche, EMSE-SE

Spécialités doctorales :	Responsables :
SCIENCES ET GENIE DES MATERIAUX	K. Wolski Directeur de recherche
MECANIQUE ET INGENIERIE	S. Drapier, professeur
GENIE DES PROCEDES	F. Gruy, Maître de recherche
SCIENCES DE LA TERRE	B. Guy, Directeur de recherche
SCIENCES ET GENIE DE L'ENVIRONNEMENT	D. Graillot, Directeur de recherche
MATHEMATIQUES APPLIQUEES	O. Roustant, Maître-assistant
INFORMATIQUE	O. Boissier, Professeur
IMAGE, VISION, SIGNAL	JC. Pinoli, Professeur
GENIE INDUSTRIEL	A. Dolgui, Professeur
MICROELECTRONIQUE	

EMSE : Enseignants-chercheurs et chercheurs autorisés à diriger des thèses de doctorat (titulaires d'un doctorat d'État ou d'une HDR)

AVRIL	Stéphane	PR2	Mécanique et ingénierie	CIS
BATTON-HUBERT	Mireille	PR2	Sciences et génie de l'environnement	FAYOL
BENABEN	Patrick	PR1	Sciences et génie des matériaux	CMP
BERNACHE-ASSOLLANT	Didier	PR0	Génie des Procédés	CIS
BIGOT	Jean Pierre	MR(DR2)	Génie des Procédés	SPIN
BILAL	Essaid	DR	Sciences de la Terre	SPIN
BOISSIER	Olivier	PR1	Informatique	FAYOL
BORBELY	Andras	MR(DR2)	Sciences et génie de l'environnement	SMS
BOUCHER	Xavier	PR2	Génie Industriel	FAYOL
BRODHAG	Christian	DR	Sciences et génie de l'environnement	FAYOL
BURLAT	Patrick	PR2	Génie Industriel	FAYOL
COURNIL	Michel	PR0	Génie des Procédés	DIR
DARRIEULAT	Michel	IGM	Sciences et génie des matériaux	SMS
DAUZERE-PERES	Stéphane	PR1	Génie Industriel	CMP
DEBAYLE	Johan	CR	Image Vision Signal	CIS
DELAFOSSE	David	PR1	Sciences et génie des matériaux	SMS
DESRAYAUD	Christophe	PR2	Mécanique et ingénierie	SMS
DOLGUI	Alexandre	PR0	Génie Industriel	FAYOL
DRAPIER	Sylvain	PR1	Mécanique et ingénierie	SMS
FEILLET	Dominique	PR2	Génie Industriel	CMP
FOREST	Bernard	PR1	Sciences et génie des matériaux	CIS
FORMISYN	Pascal	PR0	Sciences et génie de l'environnement	DIR
FRACZKIEWICZ	Anna	DR	Sciences et génie des matériaux	SMS
GARCIA	Daniel	MR(DR2)	Génie des Procédés	SPIN
GERINGER	Jean	MA(MDC)	Sciences et génie des matériaux	CIS
GIRARDOT	Jean-jacques	MR(DR2)	Informatique	FAYOL
GOEURIOT	Dominique	DR	Sciences et génie des matériaux	SMS
GRAILLOT	Didier	DR	Sciences et génie de l'environnement	SPIN
GROSSEAU	Philippe	DR	Génie des Procédés	SPIN
GRUY	Frédéric	PR1	Génie des Procédés	SPIN
GUY	Bernard	DR	Sciences de la Terre	SPIN
GUYONNET	René	DR	Génie des Procédés	SPIN
HAN	Woo-Suck	CR	Mécanique et ingénierie	SMS
HERRI	Jean Michel	PR1	Génie des Procédés	SPIN
INAL	Karim	PR2	Microélectronique	CMP
KERMOUCHE	Guillaume	PR2	Mécanique et Ingénierie	SMS
KLOCKER	Helmut	DR	Sciences et génie des matériaux	SMS
LAFOREST	Valérie	MR(DR2)	Sciences et génie de l'environnement	FAYOL
LERICHE	Rodolphe	CR	Mécanique et ingénierie	FAYOL
LI	Jean Michel		Microélectronique	CMP
MALLIARAS	Georges	PR1	Microélectronique	CMP
MOLIMARD	Jérôme	PR2	Mécanique et ingénierie	CIS
MONTHEILLET	Franck	DR	Sciences et génie des matériaux	SMS
PERIER-CAMBY	Laurent	PR2	Génie des Procédés	DFG
PIJOLAT	Christophe	PR0	Génie des Procédés	SPIN
PIJOLAT	Michèle	PR1	Génie des Procédés	SPIN
PINOLI	Jean Charles	PR0	Image Vision Signal	CIS
POURCHEZ	Jérémy	CR	Génie des Procédés	CIS
ROUSTANT	Olivier	MA(MDC)		FAYOL
STOLARZ	Jacques	CR	Sciences et génie des matériaux	SMS
SZAFNICKI	Konrad	MR(DR2)	Sciences et génie de l'environnement	CMP
TRIA	Assia		Microélectronique	CMP
VALDIVIESO	François	MA(MDC)	Sciences et génie des matériaux	SMS
VIRICELLE	Jean Paul	MR(DR2)	Génie des Procédés	SPIN
WOLSKI	Krzystof	DR	Sciences et génie des matériaux	SMS
XIE	Xiaolan	PR1	Informatique	CIS

ENISE : Enseignants-chercheurs et chercheurs autorisés à diriger des thèses de doctorat (titulaires d'un doctorat d'État ou d'une HDR)

BERGHEAU	Jean-Michel	PU	Mécanique et Ingénierie	ENISE
BERTRAND	Philippe	MCF	Génie des procédés	ENISE
DUBUJET	Philippe	PU	Mécanique et Ingénierie	ENISE
FORTUNIER	Roland	PR	Sciences et Génie des matériaux	ENISE
GUSSAROV	Andrey	Enseignant contractuel	Génie des procédés	ENISE
HAMDI	Hédi	MCF	Mécanique et Ingénierie	ENISE
LYONNET	Patrick	PU	Mécanique et Ingénierie	ENISE
RECH	Joël	MCF	Mécanique et Ingénierie	ENISE
SMUROV	Igor	PU	Mécanique et Ingénierie	ENISE
TOSCANO	Rosario	MCF	Mécanique et Ingénierie	ENISE
ZAHOUANI	Hassan	PU	Mécanique et Ingénierie	ENISE

Mise à jour : 07/04/2013

PR 0	Professeur classe exceptionnelle
PR 1	Professeur 1ère classe
PR 2	Professeur 2ème classe
PU	Professeur des Universités
MA (MDC)	Maître assistant
DR	Directeur de recherche

Ing.	Ingénieur
MCF	Maître de conférences
MR (DR2)	Maître de recherche
CR	Chargé de recherche
EC	Enseignant-chercheur
IGM	Ingénieur général des mines

SMS	Sciences des Matériaux et des Structures
SPIN	Sciences des Processus Industriels et Naturels
FAYOL	Institut Henri Fayol
CMP	Centre de Microélectronique de Provence
CIS	Centre Ingénierie et Santé

X-ray tomography and serial sectioning investigation of creep damage in copper

Centre SMS, CNRS UMR 5307

Ecole National Supérieur des Mines de Saint Etienne

158, Cours Fauriel, 42023 Saint-Etienne Cedex 2, France

2013

REMERCIEMENTS

Cette thèse a été réalisée au sein du département Microstructures et Propriétés Mécaniques du centre Sciences des Matériaux et des Structures de l'Ecole National Supérieur des Mines de Saint Etienne, sous la direction de András BORBÉLY. Je le remercie chaleureusement de m'avoir fait confiance pour mener à bien ce travail. Sa disponibilité et son enthousiasme ont été des atouts précieux, y compris dans les moments les plus difficiles.

Je tiens à remercier le professeur Yves BIENVENU pour avoir accepté de participer et présider mon jury de soutenance de thèse. Je voudrais témoigner ma reconnaissance à Eric MAIRE et Guillermo REQUENA pour avoir porté un regard approfondi sur ce manuscrit et pour la discussion qui en a suivi. Je souhaite également remercier Nathalie GEY pour avoir contribué activement à l'examen de ce travail.

Je remercie tout particulièrement mes deux coéquipiers ; Krzysztof DZIECIOL mon tuteur de programmation qui m'a initié aux principes de tomographie et puis Loïc RENVERSADE, avec qui j'avais le plaisir de travailler pendant un an. Merci également à Mathieu LENCI pour ces conseils d'utilisation de la machine de fluage; à Claire MAURICE pour ces conseils d'utilisation de l'EBSD ; à Romain QUEY pour ces conseils et son programme des calculs d'orientation 'ORILIB' et finalement à Cécilia POLETTI pour toutes les discussions constructifs qu'on avait avant de finaliser ces travaux.

Pendant plusieurs années j'ai eu la chance de pouvoir m'appuyer sur les compétences de nombreux intervenants au sein du centre. J'ai eu grand plaisir à collaborer avec Paul JOUFFREY, Sergio SAO-JOAO et Marilyne MONDON; les nombreuses heures passées au MEB n'auraient été pareilles sans leur bonne humeur, leur dynamisme et leur patience. Merci également à Yoann GARNIER et Claire ROUME pour leur disponibilité et leurs gentillesses constantes pendant les essais de fluage. La réalisation des longues heures des travaux métallographiques n'étaient surement pas possible sans la gentilles de Gilles BLANC, son impeccable labo qui est un exemple de la propreté et de la discipline. Je tiens aussi à remercier Annie, Delphine et Max de labo chimie ; Pauline, Séverine et Claude de labo Essais méca ; Olivier et Thierry de service informatique; Maude et Huguette de labo RX ; Olivier de labo Tomo ; Mark, Gilles et Bernard de l'Atelier ; Christoph et Sébastien de labo céramique ; Nicolas de labo Biomécanique ; Muriel de secrétariat.

Je remercie mes nombreux amis doctorants pour leur amitié et leur soutien. Une grande pensé à notre groupe d'amitié Flavien, My-Thu, Jean Baptiste, Vincent, Adhish, Alix, Mélanie, Karolina, Tanguy, Etienne, Grégoire, Frederic, Amélie et Robin ; à ceux qui était là avant mon arrivée Rémi, Adeline, Christoph, Laurent, Chrystelle, Olivier et Nathalia; à ceux qui sont arrivés par la suite Améth, Aly, Fiona, Amévi, Diego, Lisa, Patritzia, Monika et Jaroslav.

Merci à tous ceux que je n'ai pas pu citer mais qui se reconnaîtront pour tous les bons moments de travail ou de convivialité partagés !

Enfin, je ne peux terminer sans remercier toute ma famille, mes parents, ma sœur Roshanak et mon frère Reza (les deux derniers qui m'ont offert le plaisir d'être accompagné par des membres de la famille pendant ma soutenance). Et bien sûr je dois aussi remercier mes amis le plus chers pour leurs encouragements et leur confiance.

Short forms / Abréviations

SEM	Scanning electron microscopy	Microscope électronique à balayage
TEM	Transmission electron microscopy	Microscope électronique en transmission
EDX	Energy dispersive X-rays	Analyse dispersive en énergie
FE-SEM	Field emission SEM	MEB à effet de champ
SE-SEM	SEM imaging by secondary electrons	Imagerie MEB par électrons secondaires
BSE-SEM	SEM imaging by backscattered electrons	Imagerie MEB par électrons rétrodiffusés
EBSD	Electron backscatter diffraction	Diffraction d'électrons rétrodiffusés
EBSP	Electron backscatter diffraction pattern	Diagramme de diffraction d'électrons rétrodiffusés
BKP	Backscattered Kikuchi pattern	Bandes de Kikuchi
MAD	Mean angular deviation	Déviation angulaire moyenne
BC	Band contrast	Contraste de bande
BS	Band slope	Gradient de bande
OR	Orientation relationship	Relation d'orientation
GBS	Grain boundary sliding	Glissement des joints de grain
GB	Grain boundary	Joint de grains
CSL	Coincidence site lattice	Maille de coïncidence
f.c.c	Face centered cubic	Cubique à faces centrées
ESRF	European synchrotron radiation facility	Installation Européenne de Rayonnement Synchrotron
CT	Computed tomography	Tomographie calculée par ordinateur
3DXRD	Three dimensional X-ray diffraction	Diffraction trois dimensions des rayons X
HEDM	High energy X-ray diffraction microscopy	Microscopie à diffraction des rayons X a haute énergie
DCT	Diffraction contrast tomography	Tomographie par contraste de diffraction
BIB	Broad ion beam sputtering	Pulvérisation par faisceau d'ions large
FIB	Focused ion beam sputtering	Pulvérisation par faisceau d'ions focalisé
CMP	Chemical Mechanical Planarization	Planarisation mécano-chimique
LVDT	Linear variable differential transformer	Transformateur différentiel à variation linéaire.
CCD	Charge-coupled device	dispositif à transfert de charge
PC	Phase correlation	Corrélation de phase
CPS	Cross power spectrum	Densité spectrale d'interaction

Table of contents

Short forms / Abréviations 5
Table of contents 7
I Introduction 11
I.1 Background 11
I.2 Structure of the manuscript 13
I.3 Preliminary works 14
II State of the art 15
II.1 Creep of metals and alloys 15
II.1.1 Creep damage 15
II.1.2 Nucleation of Creep Voids 16
II.1.3 Mechanisms of creep void growth 19
II.2 Damage observations 23
II.2.1 Transition from traditional 2D to modern 3D observations 24
II.2.2 Non-destructive methods 25
II.2.3 Destructive methods 25
II.2.4 Coupling methods 27
II.3 Experimental results on creep damage 28
II.3.1 Creep voids: From visualization to quantification 28
II.3.2 Creep voids: Correlation to local crystallography 30
II.3.3 Creep voids: quantification of boundaries having a pore 31
II.4 Objectives of this thesis 31
III Experimental Techniques 33
III.1 Thermomechanical treatments 33
III.1.1 Material 33
III.1.2 In situ creep test 33
III.1.3 Creep test under high vacuum 34
III.2 Characterization techniques 35
III.2.1 Computed tomography 35
III.2.2 Scanning electron microscopy observations 40
III.2.3 Surface topography – Optical Profilometer 43
III.3 Crystallographic orientation 45
III.3.1 Electron backscatter diffraction (EBSD) 46
III.3.2 Orientation determination 47

III.3.3 Orientation calculations 48
III.3.4 Standard resolution EBSD measurements 51
IV Non-destructive damage quantification 53
IV.1 Introduction 53
IV.2 Experimental details 53
IV.3 Data treatment 54
IV.3.1 Correlating the reconstructed volumes 55
IV.4 Results 57
IV.4.1 Global (slice) registration 57
IV.4.2 Local strain rate 58
IV.4.3 Damage localization 59
IV.4.4 Similarity to final stage 60
IV.4.5 Simulation of damage distribution according to model of Cocks and Ashby 61
IV.5 Discussion of in situ tomography results 63
IV.6 Conclusions 64
V Destructive damage quantification 65
V.1 Introduction 65
V.1.1 Conventional serial sectioning 65
V.1.2 The problems of conventional sectioning methods 66
V.2 Experimental procedure 67
V.2.1 Sample preparation for serial sectioning 67
V.2.2 Material removal 68
V.2.3 Analyzing the sections 70
V.2.4 Measuring the thickness of the removed material 70
V.2.5 Serial sectioning cycle 77
V.3 Computing procedure 77
V.3.1 Data alignment 77
V.3.2 Three dimensional creep voids 79
V.3.3 The three-dimensional grain structure 83
V.3.4 Coupling the microstructure with crystallographic orientation 87
VI Serial sectioning: application to creep voids 89
VI.1 Introduction 89
VI.2 Thermo mechanical solicitations 89
VI.2.1 Creep tests 89
VI.2.2 Texture evolution during creep 90
VI.3 Microstructure analysis 91

VI.3.1 Quantification of creep void shape 92
VI.4 3D grain properties 94
VI.4.1 Grain volumes 94
VI.4.2 Crystallographic orientation 95
VI.4.3 3D grain boundaries 97
VI.5 Correlation between microstructure and grain crystallography 99
VI.5.1 Strategy of correlation 99
VI.5.2 Pore types 100
VI.5.3 Probability of different creep void types 101
VI.5.4 Effect of local crystallography on creep damage 102
VI.6 Conclusion to serial sectioning 107
VII Conclusions and perspectives 109
References 111

I Introduction

I.1 Background

Steam power plants produce an important part of the electricity around the world. Hot gasses from fossil fired combustion or waste heat source from gas turbines convert water into superheated steam. By increasing the working steam temperature and pressure the efficiency of the unit increases, which lowers fuel consumption and the environmental impact. The high temperature strength is strongly related to the creep deformation in components. Creep is the plastic deformation that a material undergoes when subjected to a constant stress. Power plant materials have to resist stresses and temperatures during long-term conditions in order to avoid creep failure. The life-time of a power plant unit can be as long as 30 years. In order to estimate the long-term creep strength, basic understanding of the involved mechanisms is essential. Figure I-1 presents a classic medium term creep rupture in a re-heater.

Figure I-1 A classic medium term creep rupture in a re-heater [1].

The service lifetime of these components may be shortened by the premature onset of creep cavitation. A considerable number of studies on creep damage accumulation have been carried out for more than 50 years. Significant progress in the field has been particularly reported in the 1970's as a result of the advances in understanding processes governing the kinetics of creep cavity growth. Thus, several consecutive relationships have been developed to model the growth of voids by grain-boundary diffusion, surface diffusion, power-law creep and the combination of these mechanisms.

Creep rupture by cavity nucleation, growth and coalescence is an important failure mechanism of high temperature components. Due to the economical importance of the phenomenon much attention has been given to understand these mechanisms and in particular to the influence of the microstructure on creep and creep damage. Figure I-2 shows an example of the effect of microstructure to creep resistance of a turbine blade. The creep damage resistance of the turbine blade increases as its microstructure changes from an equi-axed granular structure towards a columnar and single crystal structure.

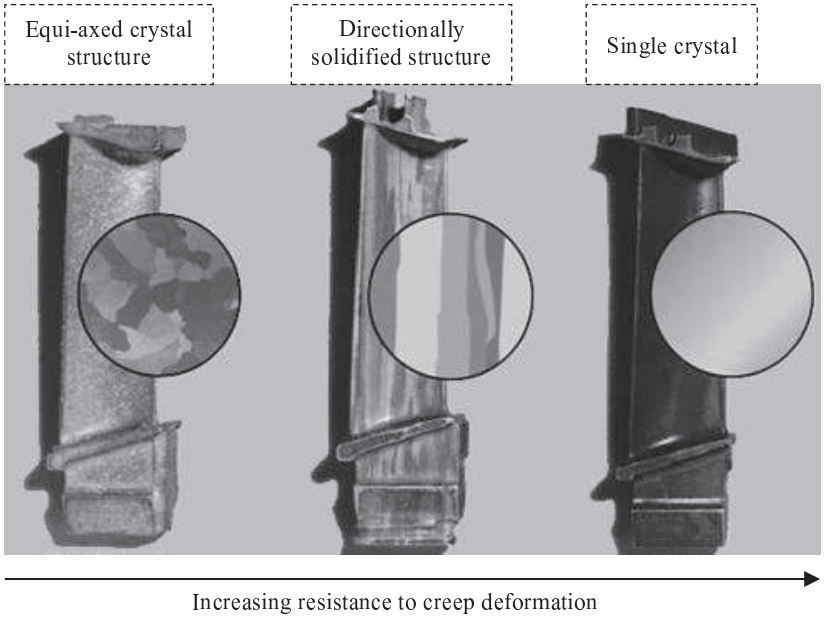

Figure I-2 Influence of microstructure on creep damage resistance

In order to understand better the relationship between the microstructure and creep damage, quantitative inspection of damage in three dimensions (3D) is required. Visualization and characterization of microstructure in 3D is extremely useful to understand morphological factors of phases or grains influencing the damage. Based on stereological arguments it is sometimes possible to describe the 3D microstructure from 2D sections, but this is not always correct because a 2D section does not contain all the information of the true 3D geometry. So the detailed information concerning topological aspects of microstructure such as connectivity or void shape cannot be obtained from independent sections. Therefore, direct observations of 3D microstructure are of interest. Various methods have been developed for this purpose:

1) Non-destructive methods such as computed tomography (CT).
2) Destructive methods such as serial sectioning, based on the gradual removal of material layers to obtain a series of scanning electron or optical microscopy images.

The purpose of this work is to apply two complementary techniques synchrotron tomography and destructive serial sectioning to characterize creep damage in copper. The non-destructive nature of synchrotron tomography allows performing in situ tests and a deterministic quantification of damage evolution that can be compared with existing damage evolution models. Since tomography is insensitive to crystallographic orientation a major information regarding the correlation between creep cavities and the type of grain boundaries (GBs) where they are located is missing. Such an information is evidently more pertinent and may allow the development of better damage models. Therefore, a second approach an improved serial sectioning method was developed and applied to characterization of creep deformed samples. Combining SEM images and electron backscatter diffraction (EBSD) measurements, damage could be finally correlated to local crystallography.

I.2 Structure of the manuscript

The manuscript is composed of the following chapters:

- Chapter § II: A literature review is devoted to observations and models describing high temperature creep damage. Then the reviews proposing different observation methods are discussed, which are able to provide three dimensional information about structure and texture. Finally, conclusions of reviews are presented which correlate the creep damage to local crystallography. At the end of the chapter the objectives of the work are stated.
- Chapter § III: presents the experimental techniques used for this work. We are detailing the thermo-mechanical treatments applied to the samples. Then the characterization techniques capable to measure the damaged state are discussed. Finally we describe the details for capturing and analyzing local crystallography using the EBSD method.
- Chapter § IV: presents the in situ performed creep test together with the synchrotron X-ray tomography observations. Then the analysis technique is developed and finally the reconstructed data along with modeling are presented.
- Chapter § V: This part is devoted to the experimental and computing procedure utilized to acquire and correlate the microstructure data within the serial sectioning method. Fundamental improvements were done to the conventional procedure to improve the quality and the resolution of the reconstruction. The crystallographic analysis by EBSD is then combined with serial sectioning to obtain information about local crystallography around voids.
- Chapter § VI: Presents the results obtained from the serial sectioning procedure. The results are compared for two samples creep deformed under two different conditions from the point of view of cavity growth mechanisms: i) at high temperature and low stress where the GB diffusion growth mechanism is dominant and ii) at lower temperature and high stress where growth by creep plasticity is the dominant.
- Chapter § VII: A general conclusion of the work done in this thesis is presented together with perspectives.

I.3 Preliminary works

This thesis was preceded by the following publication:

R. Abbasi, L. Renversade, K. Dzieciol, A. Borbély, and A. R. Kaysser-Pyzalla, “Damage fluctuations in creep deformed copper studied with synchrotron X-ray microtomography,” International Journal of Materials Research (formerly Zeitschrift für Metallkunde), vol. 103, no. 02, pp. 228–233, Feb. 2012.

II State of the art

II.1 Creep of metals and alloys

The efficiency of electricity-generating power plants in general and gas turbines in particular, increases with increasing service temperature. This requires components with enhanced high-temperature creep-strength and the knowledge of damage evolution during creep permitting the prediction of their service lifetime, which is usually restricted by nucleation and growth of creep cavities.

During the deformation of a solid at high temperature its microstructure changes. Holes may nucleate and grow inside the solid; its grain size may increase or decrease due to dynamic recrystallization. Precipitates or second phase dispersoids within it may coarsen or dissolve and substructure introduced by prior working may be destroyed. All these changes are referred as "creep damage" that usually accelerates the creep-rate, which in turn accelerates the rate of damage development. In this thesis, however, creep damage refers only to creep cavities.

II.1.1 Creep damage

Creep of materials is described to be the time dependent plasticity under fixed stress (below the yield stress) at elevated temperature, often greater than $0.5\,T_m$, where T_m is the absolute melting temperature. The elementary test to study creep deformation and failure is the uniaxial creep test.

When the sample is subjected to a constant load (or a constant stress), and the elongation is measured as a function of time. The creep test is composed of two steps: charging and the creep deformation itself. The charging step induces an instantaneous defamation noted as ε_i. The plasticity under deformation conditions of high temperature and constant stress is usually described by the two following curves:

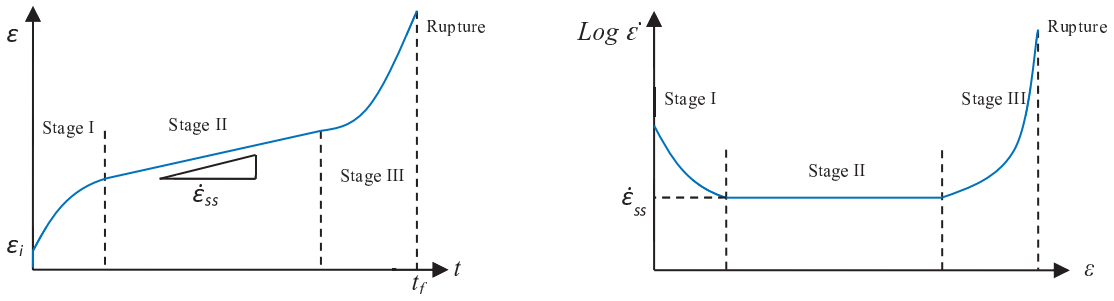

Figure II-1 Creep curves

In general the creep curve can be divided in the following three stages:

- Primary creep or stage I, when the creep rate (or deformation rate) decreases with the time, indicating the increase of the material resistance against plastic deformation. This is due to a strengthening mechanism.
- Secondary creep or stage II, which is also, called the steady-state., when the strain rate ($\dot{\varepsilon}_{ss}$) is nearly constant.

- Tertiary creep or stage III, when the creep rate increases leading to rupture. This increase in the creep rate is usually linked to damage evolution in the microstructure.

Creep life time under constant stress can be described by the Monkman-Grant relationship [2], which states the fracture is controlled by the steady-state creep rate, $\dot{\varepsilon_{ss}}$:

$$\dot{\varepsilon}_{ss}^{m} t_f = k_{MG} \qquad \text{Equation II-1}$$

where k_{MG} is the Monkman-Grant constant and m is a constant typically about 1.0. This relationship was already confirmed experimentally for metals and alloys, and it's independence of stress and temperature has been demonstrated several times [3], [4].

There are a variety of reviews on creep fracture by Needleman and Rice [5], Cocks and Ashby [6] and particularly the books by Riedel [7] and Kassner [8]. This chapter will review the most recent works. Fracture by cavitation will be discussed in two steps, nucleation and subsequent growth. Nucleation mechanisms are described first followed by the mechanisms of void growth.

II.1.2 Nucleation of Creep Voids

It is still not well established by which mechanism cavities nucleate. It has generally been observed that cavities frequently nucleate on **grain boundaries**, particularly on those transverse to a tensile stress. If grain boundaries slide easily, as they do in pure metals, they focus stress on **triple junctions**, which will be highly favorite sites for cavity nucleation. **Slip bands** are the other possible nucleation sites as reported by Afshar and Biscondi [9]. Dislocation motion during plastic deformation is concentrated in more or less pronounced slip bands within the grain. If such a slip band impinges on a grain boundary, it causes a high stress concentration which might nucleate a cavity. However, in most commercial materials, the most common cavity nucleation sites are **second phase particles** in grain boundaries.

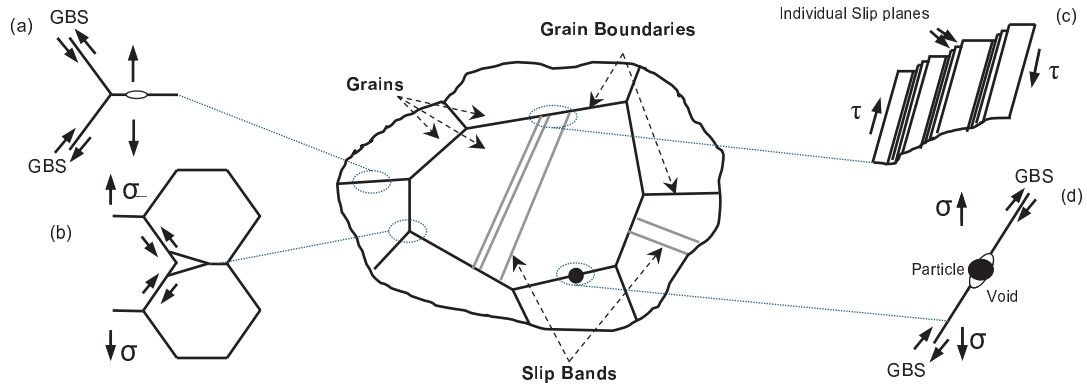

Figure II-2 Nucleation sites at (a) GBs transverse to the tensile stress axis (b) triple junction of grains (c) slip bands (d) second phase particles

In order to better understand the creep mechanisms and rupture we should take a look at the role of microstructure when it is subjected to external stress.

It is described by Edward and Ashby [10] that under certain creep conditions the grain boundaries in polycrystals can slide on each other. The process of GB Sliding (GBS) involves the movement of individual grains, which slide over each other with the movement taking place at, or in a zone immediately adjacent to their common boundary.

As illustrated in the Figure II-3 this sliding can be accommodated in various ways: elastically (Grain1), by diffusion leading to diffusional flow (Grain2) or by non-uniform creep or plastic flow of the grains themselves (Grain3):

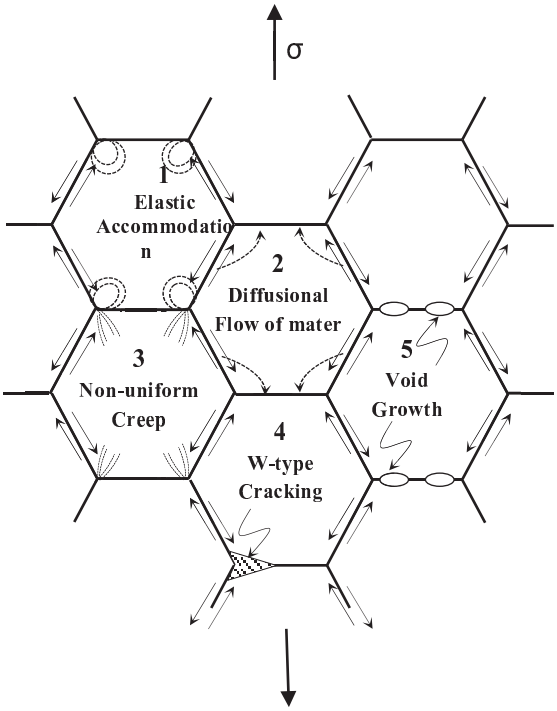

Figure II-3 Grain boundary sliding concentrates stress on grain boundaries which lie normal to the tensile stress. It can be accommodated (1) elastically (2) by diffusion or (3) by plasticity or creep. If it is not, cracks (4) or holes (5) appear and grow at the boundaries on which the stress is concentrated. (adapted from:[10])

If the incompatibility created by sliding is not accommodated in any of these ways, holes or cracks will appear at grain boundaries, which was found by experimental observations. Two main pore types were evidenced: w-type cracks (wedge-type) and r-type voids, which lie at triple junctions and simple boundaries, respectively (see Figure II-4).

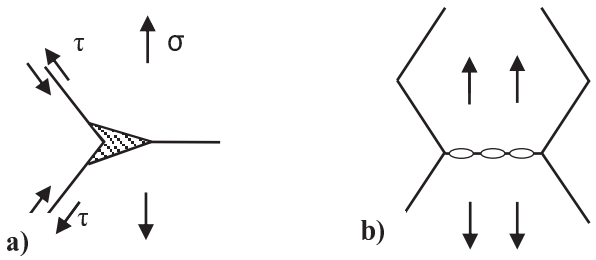

Figure II-4 Void initiation by (a) w-type cracks and (b) r-type voids

Zener [11] was the first to propose the w-type crack nucleation at triple junctions. He suggested that at high enough temperatures the grain boundaries have viscous behavior and that behind triple junctions, the displacement of the adjacent boundaries are limited. So, under the effect of a tensile stress there is a high stress concentration at triple lines, while the shearing stress of the neighbor non-perpendicular boundaries would be compensated by the applied stress. Tanaka and Lizuka [12] explained the initiation of the intergranular w-type crack in creep, using a continuum mechanics model which incorporated a recovery effect by atomic diffusion. They have

found a good agreement between the prediction of the model and experimental data for austenitic steel and concluded that there is a critical creep rate for wedge-type crack initiation.

Another mode of fracture has been associated with r-type pores at transverse grain boundaries. Greenwood and coworkers [13] suggested that nucleation of r-type voids does not depend on the stress concentration. However, according to Chen and Argon [14] there might be a correlation between propagation of w-type cracks and the presence of r-type voids at the grain boundaries.

GBS can lead to stress concentration and at triple lines. One difficulty with the sliding mechanism is that transverse boundaries appear to have a higher propensity to cavitation. One experimental study by Afshar and Biscondi proved that the damage due to cavitation is controlled by grain boundary sliding [9]. They have provided experimental data permitting the quantification of the influence of GBS on the nucleation process. This was done using bicrystals of copper with varying grain boundary angle with respect to the axis of applied stress. Then the evolution of cavitation was observed as a function of the amount of grain boundary sliding on a given grain boundary. Cavitation has been observed by Gandhi and Raj [15] in bicrystals where the boundary was perpendicular to the applied stress, such that there is no resolved shear and an absence of sliding.

More recently Ayensu and Langdon [16] found a correlation between GBS and cavitation. They have demonstrated that cavitation is inhomogeneous within any specimen, with an increase in the level of cavitation in regions of higher local strain. It was shown that the total cavitated area increases at high sliding rates, but the number density of cavities decrease at the highest sliding rates because of cavity interlinkage.

The nucleation models fall into several categories:

a) Grain boundary sliding as described earlier.
b) Cavity nucleation from **vacancy condensation** at a high stress region. The idea of agglomeration of vacancies to form stable voids (nuclei) was first developed by Raj and Ashby [17]. It should be emphasized that only certain of the voids with a critical radius of a^* and free energy of ΔG_T^* are stable to grow and their nucleation rate can be expressed as the following equation:

$$\dot{N} \cong n^* D_{gb} \qquad \text{Equation II-2}$$

where,

$$n^* = n_0 \exp(-\frac{\Delta G_T^*}{kT}) \qquad \text{Equation II-3}$$

D_{gb} is the grain boundary diffusion coefficient and n_0 is the density of potential nucleation sites. Riedel [7] has also included a 'Zeldovich' factor in this equation to account for dissolution of the supercritical nuclei with $a > a^*$.
As transverse boundaries may not readily slide, it has been suggested that vacancy accumulation occurs by stress concentration associated with **dislocation pile-ups** against, hard second-phase particles or grain boundaries [18]. Dyson [19] showed that the nucleation process can be continuous through creep and that growth and nucleation may occur together. He also proved the effect of pre-strain, which shows that the nucleation process may be controlled by plasticity.
c) Cavity formation at **particle-obstacles**. Kassner et al. [20] showed continuous nucleation of cavities in the neighborhood of high angle boundaries with obstacles (regions of highly twinned metal surrounded by low twin density regions). High angle boundaries without

obstacles did not appear to cavitate. The material studied in this thesis does not contain any second phase particles or impurities, so this particular mechanism is not discussed.

II.1.3 Mechanisms of creep void growth

The following section describes the current understanding of cavity growth during creep in polycrystalline metals and alloys. Growth is discussed based on the diffusion-controlled model proposed initially by Hull-Rimmer [21] and slightly corrected later by Speight and Beere [22], as well as according to the plasticity controlled model of Hancock [23] and Cocks and Ashby [24]. Finally, the coupled diffusion plasticity model of Needleman and Rice [5] and Chen and Argon [14] will be treated.

II.1.3.1 Diffusion-controlled growth

Cavity growth process at grain boundaries and elevated temperatures has long been suggested to involve atomic diffusion. Figure II-5 presents the basic geometry of the model.

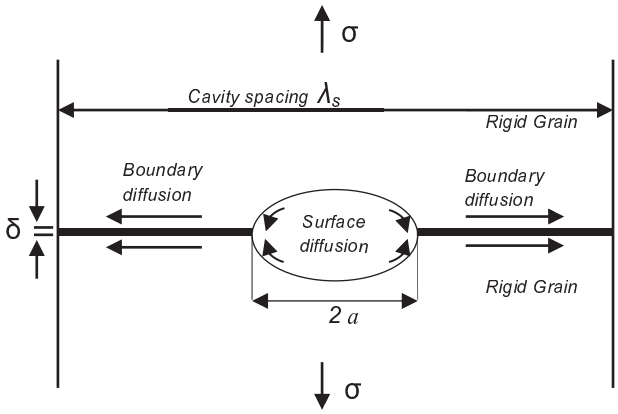

Figure II-5 Cavity growth by diffusion across the cavity surface and along GBs due to a stress gradient

In this schema a cavity with radius a is shown on a GB lying perpendicular to the direction of the applied stress. During the growth step the atoms are transported from the cavity surface along the GB. This diffusion takes place first along the cavity surface and then along the grain boundary where the atoms are deposited. Since the slowest process controls the growth rate, the two diffusion mechanisms need to be discussed separately.

II.1.3.1.1 Grain boundary diffusion-controlled growth

The growth process by grain boundary diffusion becomes the controlling mechanism if it is slower than the surface diffusion. In this case the cavities maintain an equilibrium shape. According to Hull and Rimmer [21], who treated this problem for the first time, (or others like Speight and Beere [22] or Riedel [7] who derived similar equations), the growth rate of a cavity with radius a is given by:

$$\frac{da}{dt} = \frac{D_{gb}\delta\,\sigma\Omega}{kTa^2} \qquad \text{Equation II-4}$$

where δ is the grain boundary width, Ω the atomic volume, k is the Boltzmann's constant, T is the temperature and D_{gb} the grain boundary diffusion coefficient (rate controlling parameter). By integration between the critical radius (below which sintering occurs) and $a = \lambda_s/2$ we get the rupture time expressed as a function of the inverse of stress (Equation II-5).

$$t_f \propto \frac{1}{\sigma}$$ Equation II-5

This is the first relationship between stress and rupture time for diffusive cavity growth. Later, others suggested improved relationships between cavity growth rate and stress similar to that of Hull and Rimmer. Riedel [7] suggested Equation II-6 for the growth rate of widely spaced voids.

$$\frac{da}{dt} = \frac{D_{gb}\delta\,(\sigma - \sigma_0)\Omega}{1.22kTln(\frac{\lambda_s}{4.24a})a^2}$$ Equation II-6

where σ_0 is the sintering stress. Again, integration to determine the time for rupture leads to Equation II-5. Despite these improvements, the basic description long suggested by Hull and Rimmer is largely representative of unconstrained cavity growth of widely spaced voids. More recently Cho et al. [25] have measured the rupture times and cavity growth rate and found consistency with the cavity diffusion growth model of Hull and Rimmer if allowance for continuous nucleation was made.

The vast majority of creep-rupture experiments yield stronger stress dependency often compatible with the Monkman-Grant equation, i.e. $t_f \propto 1/\dot{\varepsilon} \propto 1/\dot{\sigma}$. This led to continuing investigations regarding the possible reasons. In addition to the unexpectedly strong stress dependence the observed rupture time is generally much longer than predictions by simple diffusion-controlled cavity growth models.

II.1.3.1.2 Surface diffusion-controlled growth

The growth process by surface diffusion becomes the controlling mechanism if it is slower than the diffusion along grain boundaries. The cavity develops a crack-like shape as it grows because atoms at the cavity tip are removed at a faster rate than they are replaced by surface diffusion from other regions of the cavity surface. This is known as non-equilibrium cavity growth because the cavities have a non-equilibrium shape during growth.

It has been showed by Chuang and Rice [26], that for a given geometry of the void tip the surface flux is only related to the cavity radius a and da/dt. They also suggested (and later confirmed by Needleman and Rice [5]) that at low stresses the cavity growth law is as following:

$$\frac{da}{dt} = \frac{\delta D_s \Omega \sigma^3}{2kT\gamma_s^2}$$ Equation II-7

where, D_s the surface diffusion coefficient and $\gamma_s$is the surface energy. This suggests that the rate of cavity growth depends on the third power of stress. Also it was proposed that at higher stresses the growth rate varies as $\sigma^{3/2}$ [7], [8]. Although cavity growth seems to be controlled by surface diffusion it is difficult to understand why surface diffusion should be much slower than grain boundary diffusion. For most of the materials D_s is larger than D_{gb} [7], [8].

II.1.3.2 Plasticity-Controlled growth

At higher creep rates and stresses cavities can grow exclusively by plasticity. At high stresses the solid undergoes power-law creep described by the constitutive law:

$$\dot{\varepsilon}_{ss} = \dot{\varepsilon}_0(\sigma_e/\sigma_0)^n$$ Equation II-8

where, σ_0 and n are creep constants, $\sigma_e$is the Von Mises equivalent (tensile) stress, defined by:

$$\sigma_e = \left\{\frac{1}{2}[(\sigma_1 - \sigma_2)^2 + (\sigma_2 - \sigma_3)^2 + (\sigma_3 - \sigma_1)^2]\right\}^{1/2}$$ Equation II-9

And $\dot{\varepsilon}_{ss}$is the equivalent (tensile) strain-rate:

$$\dot{\varepsilon}_{ss} = \left\{\frac{2}{9}[(\dot{\varepsilon}_1 - \dot{\varepsilon}_2)^2 + (\dot{\varepsilon}_2 - \dot{\varepsilon}_3)^2 + (\dot{\varepsilon}_3 - \dot{\varepsilon}_1)^2]\right\}^{1/2} \quad \text{Equation II-10}$$

The quantity $\dot{\varepsilon}_0$depends exponentially on temperature:

$$\dot{\varepsilon}_0 \propto exp - \frac{Q_c}{RT} \quad \text{Equation II-11}$$

where, $Q_c$is the activation energy for creep and $\sigma_1\sigma_2\sigma_3$ and $\dot{\varepsilon}_1\dot{\varepsilon}_2\dot{\varepsilon}_3$ are the principal stresses and strain rates.

Hancock [23] initially proposed the plasticity-controlled cavity growth based on the idea that cavity growth during creep should be analogous to McClintock's model [27] for a cavity growing in a plastic field. Corresponding to this model, cavity growth occurs as a result of creep deformation of the material surrounding the grain boundary cavities in the absence of a vacancy flux. So the hole might grow because of the stress concentration associated with it, the creep strain possibly being produced by dislocation movement. It is useful to note that one characteristic of cavity growth by creep plasticity is that the cavity tends to elongate in the direction of maximum principal stress and grows as an ellipsoid (as illustrated in Figure II-6).

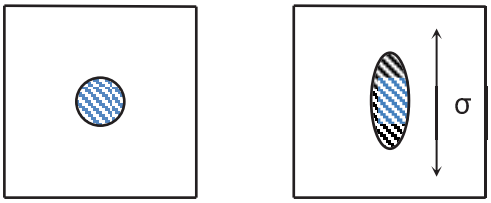

Figure II-6 (Left) Spherical void in polystyrene before creep. (Right) Void in polystyrene after creep in uniaxial tension. Arrow=direction of applied stress

The first models of cavity growth by power law creep considered an isolated cavity in a nonlinearly viscous infinite continuum, which obeys the Norton's law: $\dot{\varepsilon} = A\bar{\sigma}$. The basic model for cavity growth by power law creep was proposed by Budiansky [28]. According to this, the void volumetric growth rate in a uniformly deforming nonlinearly viscous solid is proportional to the void's actual volume (V) and the steady-state strain rate:

$$\dot{V} = \Lambda\dot{\varepsilon}\ V \quad \text{Equation II-12}$$

where, Λ is a dimensionless factor which depends on the current void shape and stress state. Riedel [7] described the growth rate of equilibrium cavity shapes in homogenous stress and strain fields as follows:

$$\dot{a} = a\Lambda\dot{\varepsilon}_e^{\infty}/3h(\psi) \quad \text{Equation II-13}$$

where a is the radius of the void, $\dot{\varepsilon}_e^{\infty}$is the equivalent tensile strain rate at large distances from the void and the function $h(\psi)$ accounts for cavity shape. Assuming that Λ is time independent and rupture condition is $2a = \lambda_s$, this equation can be integrated to get:

$$\varepsilon_f = \left[\frac{3h(\psi)}{\Lambda}\right]\ln\left(\frac{\lambda_s}{2a_0}\right) = \left[\frac{3h(\psi)}{2\Lambda}\right]\ln\left(\frac{1}{\omega_0}\right) + \varepsilon_0 \quad \text{Equation II-14}$$

where ε_0 is the strain at which the void is nucleated, a_0 is the void radius at nucleation, $\omega_0$is the voided area fraction at nucleation and ε_f is the fracture strain. If we can neglect the strain ε_0 at witch the void is nucleated, then the fracture strain ε_f becomes independent of stress. This leads to the prediction of the Monkman-Grant equation for ε_f, however the experimental values are much smaller than the predictions. Assuming $\lambda_s/2a = 10$, $h(\psi) = 0.61$ and using $\Lambda = 1.1$ for

uniaxial tension, the predicted fracture strain becomes enormous as 383% [7], while measured strains to rupture are typically of 20-30%. One possible explanation is the interaction between the cavities. Needleman and Rice [5] proved, however, that under typical creep rupture conditions, interaction effects are negligible. Recently, it has been shown by Dzieciol et al. [29] that the proportionality factor $\Lambda = 40$ indicating that the continuum model of Budiansky [28] might not be applicable in the vicinity of the void.

A different model was developed by Edward and Ashby [10] and later improved by Cocks and Ashby [24]. This is illustrated in Figure II-7 for the case of uniaxial tension. A cylindrical material volume with a diameter of $2l$ (which is equal to the separation of cavities in the boundary plane) and a height equal to the grain size d is centered on the cavity. It is further assumed that the stress on the surface of this cylinder is equal to that applied to the specimen.

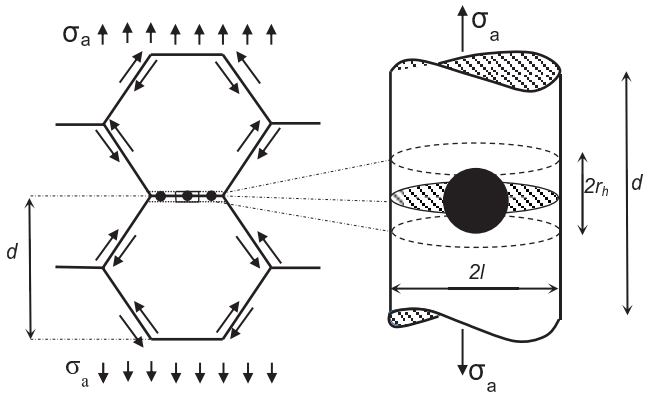

Figure II-7 Voids growing on a grain boundary in power-law creeping solid [24]

For the purpose of choosing a stress field the shape of the cavity is idealized as a cylinder of radius r_h and height $2r_h$ contained in a thick annular ring. The area fraction of the pore in the boundary plane is given by: $f_h = r_h^2/l^2$. This model is approximate, but it leads to analytical expressions for the void growth-rate. It can be also adapted for the case of multi-axial loading and it can be checked against results of the finite element calculations. In the case of simple tension the result is particularly simple. The average steady-state creep rate of the cylinder in regions, where no cavities are present is $\dot{\varepsilon}_{ss}$, but the shaded slab will creep faster by a factor of $(1/1 - f_h)^n$. So the result is that the shaded slab dilates causing the cavity to grow.

By applying the continuity equation for a multi-axial stress case the following expressions for the damage rate and steady state strain rate were obtained by Cocks and Ashby [6] (Equation II-15 and Equation II-16):

$$\frac{1}{\dot{\varepsilon}_0}\frac{df_h}{dt} = \beta\left[\frac{1}{(1-f_h)^n} - (1-f_h)\right]\left(\frac{\sigma_e}{\sigma_0}\right)^n \qquad \text{Equation II-15}$$

$$\frac{1}{\dot{\varepsilon}_0}\frac{d\varepsilon}{dt} = \left\{1 + \frac{2r_h}{d}\beta\left[\frac{1}{(1-f_h)^n} - 1\right]\right\}\left(\frac{\sigma_e}{\sigma_0}\right)^n \qquad \text{Equation II-16}$$

where β is a parameter which depends on stress triaxiality. For uniaxial tension β is equal to 0.6 but in a multiaxial stress case it can be explained by:

$$\beta = \sinh - \left[2\frac{(n-1/2)}{(n+1/2)}\frac{p}{\sigma_e}\right] \qquad \text{Equation II-17}$$

where, p is the hydrostatic pressure and σ_e the equivalent von Mises stress. The time to fracture at constant stress is obtained by integrating between the limits ($f_h = f_i$ at $t = t_n$ and $f_h = f_c$ at $t = t_f$) where f_i is the initial volume fraction of the pores, t_n the nucleation time and f_c is the value of f_h at which the pores coalescence (Equation II-18).

$$t_f = t_0 + \frac{1}{\beta(n+1)\dot{\varepsilon}_0} ln\left[\frac{1-(1-f_c)^{n+1}}{1-(1-f_i)^{n+1}}\right]\left(\frac{\sigma_e}{\sigma_0}\right)^n \quad \text{Equation II-18}$$

Finally the strain to fracture in simple tension is given by Equation II-19.

$$\varepsilon_f = t_f \dot{\varepsilon}_0 \left(\frac{\sigma_e}{\sigma_0}\right)^n + 0.2\frac{l}{d} \quad \text{Equation II-19}$$

Riedel [7] has also proposed a similar relationship, which accounts for void interaction effects. He argued that although the Monkman-Grant constant (C_{MG}) can be reduced considerably by the net-section-stress, the effect is insufficient to explain the experimentally observed low creep ductility. As an example for $n = 5$ the initially voided area fraction must be as large as $f_0 = 0.16$ if $C_{MG} = 0.25$. If more realistic values for f_0 are chosen (like $f_0 < 0.01$) then this constant's value increases to more than 1. This is a result appropriate for superplastic materials but not for creep rupture conditions.

II.1.3.3 Coupled growth

At intermediate strain rates the mechanisms described in previous sections can act simultaneously. This can lead to an enhanced growth rate of cavities. The combined effect of plasticity and boundary diffusion was studied by several authors - Edward and Ashby [10], Needleman and Rice [5], Chen and Argon [14] and Cocks and Ashby [6]. They suggested that the matter transported along the grain boundaries is accommodated by creep flow and this leads to faster growth of cavities. Needleman and Rice [5] developed a continuum model describing the combined mechanism. They have introduced a length parameter L, which is a function of stress, temperature and material. When $L \leq a$ (void radius), then interaction between creep plasticity and diffusion may lead to increased cavity growth. Accordingly to Budiansky [30], power law creep is important at large values of a/L, diffusion at small a/L and coupling within a range of $(0.2 < a/L < 20)$ [5].

$$L = L_0 e^{k^T m/T}[\mu/10^3\sigma]^{(n-1)/3} \quad \text{Equation II-20}$$

$$L_0 = 10^{n-1}[\delta_b D_{b0}\Omega/AbD_{v0}]^{1/3} \quad \text{Equation II-21}$$

$$k = (Q_v - Q_b)/3RT_m \quad \text{Equation II-22}$$

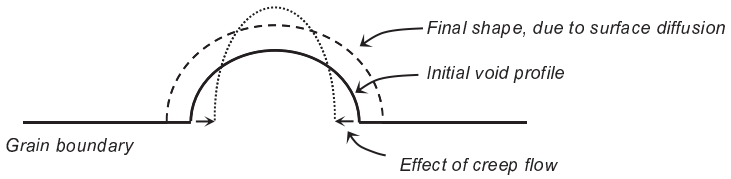

Figure II-8 Illustration of the effects of plastic creep flow – Cavity growth by the combination of plastic creep flow (which, if considered alone, generally tends to decrease the void radius)

II.2 Damage observations

Material's behavior is controlled by their microstructure. The details of each microstructure such as grain size, distribution and morphology of different phase affect the thermal and

mechanical behavior of the material. It is therefore important knowing the microstructure characteristics in order to predict material behavior. A simple example of such a model is the Hall-Petch relation that couples the grain size to the yield strength.

II.2.1 Transition from traditional 2D to modern 3D observations

Traditional methods of visualizing the microstructure involve simplifying the three-dimensional (3D) structure into a two-dimensional (2D) representation by optical or scanning electron microscopy. While 2D representation of microstructure is common and gives some idea about microstructure morphology, it is not fully representative of the 3D structure of the material. For example in the case of reinforced metal matrix composites [31] or alloys with particles such as precipitates or intermetallics [32], [33] the three-dimensional nature of microstructural features play an essential role in understanding microstructural evolutions as well as macroscopic properties. Even though traditional metallographic techniques can be used for rapid characterization many microstructural features, even simple three-dimensional shapes often cannot be deducted from examination of random planar cuts, much less the complex morphologies and distribution of grains and precipitates. In general, the conventional 2D metallographic methods are not sufficient to study interconnected structures and complex shapes.

Another example is the complex 3D shape of fatigue cracks, which are difficult to accurately characterize by surface (2D) observations, especially at the early stages of fatigue crack growth when the morphology is heavily influenced by the material microstructure [34]. Therefore, to visualize and fully understand the material's microstructure a technique that can capture the 3D nature of polycrystalline grains is required [35].

An accurate simulation of the material behavior can only be obtained by incorporating the actual 3D microstructure as the structural basis for the model. In recent years, there has been an intensive research in recovering the 3D structural information. The drivers for this interest are the wealth of information obtained by a 3D analysis, specifically spatial distribution of phases, real feature size, shape and connectivity. Two important parameters are usually necessary to choose before selecting an investigation technique. These are the resolution and the volume of material to be analyzed. As it is obvious in Figure II-9, performing a statistical analysis over a large surface of the sample limits the resolution. Inversely, higher resolution techniques are more local and less applicable for statistical analysis.

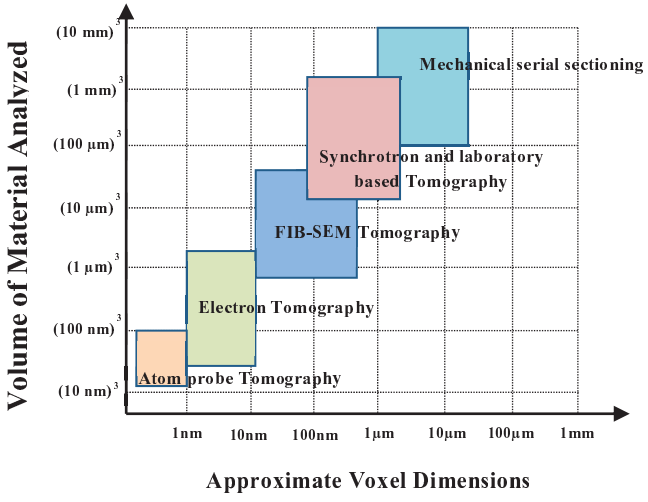

Figure II-9 Three-dimensional analysis techniques and their corresponding resolution and volume size.

The following sections discuss these methods separately based on their destructive or non-destructive nature.

II.2.2 Non-destructive methods

One of the recently developed nondestructive characterization at micrometer scale of 3D structures is computed tomography (CT). In this method a finely collimated X-ray beam passes through the structure and X-ray attenuation measurements are made at many rotation angles. These measurements - called projections - are then stored and used for the reconstruction of two-dimensional CT images. By stacking a series of such images the full 3D structure can be recovered. Hence this method is widely used for characterization of microstructures [31], observation of damage [36] or identification of damage mechanisms [37].

Regarding the fact that investigation of damage fluctuations during damage evolution would help to understand the mechanisms of damage [38], only chronological mapping of the proliferation of voids or cracks by micro-CT may not be adequate to establish an accurate damage model. It is therefore important the study of the relationship between the observed damage zones and local crystallography.

However, for some specific material systems it is possible to reveal the grain structure by decorating the grain boundary network with a thin film of a second phase having different X-ray attenuation and/or electron density. For example Ludwig et al. [39] and later Toda et al. [40] achieved grain boundary decoration by wetting them with liquid Gallium of a few hundred nanometers thick and visible as bright lines in tomographic slices. But even in such case tomography lacks information on the crystallographic orientation of the grains.

Recent developments such as Three Dimensional X-ray Diffraction (3DXRD) [41], High Energy X-ray Diffraction Microscopy (HEDM) [42][43] or Diffraction Contrast Tomography (DCT) [35], are non-destructive 3D orientation mapping based techniques, which enable obtaining grain specific crystallographic information. These methods are cost and time-consuming and it is not always possible to perform them with laboratory equipment. Another problem is that the above methods can be performed only in the absence of orientation and strain gradients, when the diffracted beam can be treated as parallel projections of the diffracting grain. The methods allow, however, a good reconstruction of the crystallographic orientation and 3D shape of grains in non-deformed samples [44].

II.2.3 Destructive methods

Among the observation methods having a destructive nature three dimensional metallographic investigations using the deep etching technique can be mentioned. It reveals the variety of true shapes and interconnections between fragmented morphologies, but it is clear that the application of this method is limited to certain cases. From the modern methods, serial sectioning is available by ultramicrotomy [45], a method for cutting the specimen into extremely thin slices or sections that can be viewed in a transmission electron microscope (TEM). In this method sections must be very thin because the 100 to 200 kV electrons of the standard electron microscope cannot pass through material thicker than 150-200 nm. For best resolution, sections should have a thickness of 30 to 60 nm.

Form the modern methods we can mention Atom-Probe Tomography (APT), which provides direct three-dimensional information concerning microstructure and chemical composition on a sub-nanometer scale [46]. From these atom scale observation methods we can also mention the

Knife-Edge Scanning Microscopy (KESM), which is a diamond ultramicrotome and line-scan based imaging system to serially section large volumes ($V > 1cm^3$) of material [47].

Serial sectioning is a technique which involves the preparation of a polished section suitable for microscopy and then the sequential recording (most usually either by optical or scanning electron microscopy (SEM)) to create a series of images. Each polishing step is carefully controlled to remove a known thickness of the specimen. Once the dataset is acquired the volume is reconstructed using image processing techniques. Serial sectioning permits generation of significantly large volumes (~few mm^3) of 3D microstructures at high resolution (up to sub-micrometric) and is used over a century in different fields of science as in mineralogy [48], biology [49] and materials science [50]–[52].

The basic steps of the conventional serial sectioning process are as follows:

1. Sample preparation
2. Fiducial marking by indentation
3. Material removal
4. Image acquisition
5. Repeating steps 3,4 and if needed step 2 up to desired thickness
6. Image processing (segmentation, image registering, etc.)
7. Serial section stacking, 3D reconstruction and visualization

Choosing the right technique needs some more information on material removal procedure. Material removal is conventionally performed by mechanical polishing, a procedure that can be manual or automatic. Recent developments led to automated serial sectioning methods using robots [53], [54]. These are fast and reproducible, but as the robot is coupled with an optical microscope the accuracy of the method remains the same (optical scale). Beside the conventional mechanical removal method ion beam sputtering was also used to generate 3D visualizations of materials.

The development of broad and focused ion beam etching techniques led to a full comprehension of the material removal by ion beam sputtering. The advantages of the process compared with other etching or machining methods are the universal applicability to all substances, the controllable high accuracy of attack vertically down to atomic monolayers, laterally with nanometer resolution and the fact that thermal effects can be kept small. Beyond this, undesired chemical effects can be avoided. However, limitations of the ion beam sputtering process have to be also considered, for example: control of dose and density distribution, mass and energy homogeneity, direction, divergence, positioning and stability. Some of these are indicated below.

Broad Ion Beam (BIB) sputtering develops single slopes at most grain boundaries and grooves occur preferentially at normal ion incidence. Following schema can help us understand the developments of single slopes.

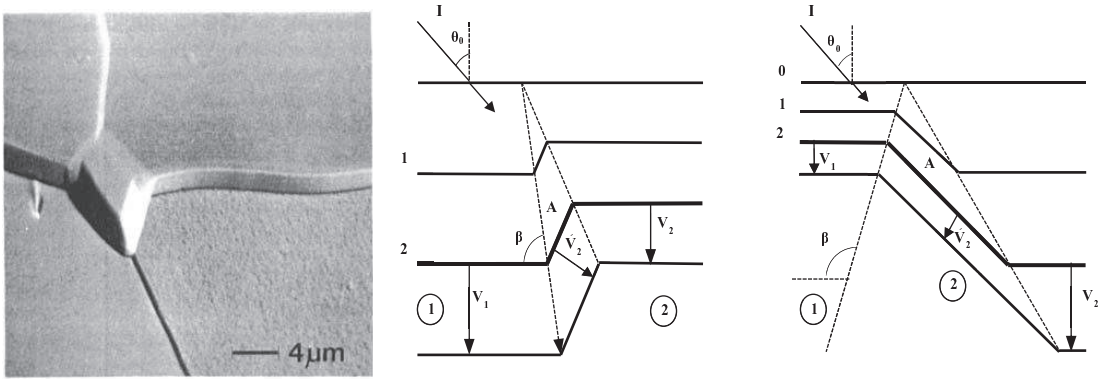

Figure II-10 Selective grain etching of polycrystalline Fe after bombardment with 10KeV Kr+ ions under 50° to the normal (Left). Model of slope development at a boundary between two grains with $v_1 > v_2$ (Middle) and $v_2 > v_1$ (Right). Here A is the slope, I the ion beam direction; θ_0 the angle of incidence, β the inclination of the grain boundary, v_1, v_2 and $\dot{v}_2$ are erosion velocities.[55]

It has been shown by Hauffe [55] that the grains are sputtered at different velocities, according to their crystallographic orientation to the ion beam direction. Neglecting the small relief structure on the grains, sputtering effects of reflected ions and re-deposition of sputtered material (which all occur, but do not prevent our basic discussion) the erosion velocity $v_i$of an area I of a surface relief is:

$$v_i = \frac{1}{N_s} J_0 \cos\theta_i \, Y_i(\theta_i) \qquad \text{Equation II-23}$$

where, $N_s$is the particle density of the solid, Y the sputtering yield, θ the incidence angle and J the ion beam density. The term $Y(\theta)$ represents of the sputtering yield on the incidence angle on the slope A. This model is applied and experimentally confirmed [55] for different three-dimensional arrangements of grain boundaries and ion beam directions from normal to grazing incidence. Unfortunately BIB sputtering method is not the appropriate method to produce parallel sections without creating artifacts at the micrometer scale.

Using the Focused Ion Beam (FIB) completely eliminates this artifact. So, FIB sputtering can actually generate parallel sections with a very high resolution. But the disadvantage of FIB-tomography resides in its local nature, leading to reconstructed volumes that are often smaller than the representative volume element required to understand the macroscopic properties of the material.

As an advantage of ex situ static microstructural investigations serial sectioning offers an inherent flexibility of coupling with other techniques and the relatively low cost of needed equipment's.

II.2.4 Coupling methods

At present, there is no single technique that can fully characterize the microstructure. Combinations of techniques specifically chosen to investigate a particular microstructural feature of interest are often used.

Clearly, the significant manual intervention required for traditional serial sectioning technique means that this is slow and tedious to perform. Moreover, it is limited in precision by the resolution of the imaging instruments. But once the section's surface is polished it becomes possible to interface a range of detectors to collect not only secondary electrons, but also

characteristic X-rays for Energy Dispersive X-ray (EDX) analysis [56] and back-scattered electrons for Electron BackScatter Diffraction (EBSD) analysis [57]–[59].

Serial sectioning and micro tomography have been earlier used in complementary manner to study the 3D morphological characteristics of Si and Ni-aluminide phases in Al-Ni piston alloys in the as-cast and solution treated conditions [56]. While synchrotron micro tomography was used to quantify the connectivity, shape and volume fraction of the two phases, their contiguity was assessed by serial sectioning. In the work of Gupta and al. [60] the two techniques are combined to study the cavitation behavior in a tempered martensitic steel crept at different stresses with the aim of clarifying the role of different internal interfaces.

Developments in experimental techniques are determined by the available equipment but, sometimes they are determined following the needs of the scientific/industrial community. One such example is the commercialization of automated EBSD, a scanning electron microscopy technique that automatically acquires and processes electron Kikuchi diffraction patterns for determination of local lattice orientations. The method can be used to extract parameters such as grain size, grain shape, volume fraction and morphology of inclusions or precipitates (if exist). In addition to orientation dependent features such as micro-texture and grain boundary character distribution. Thus EBSD appears ideally suited for coupling with serial sectioning in order to reconstruct many details of the three-dimensional grain structure.

Several coupling techniques were used to combine damage observations to the local crystallography. Birosca et al. [61] observed the three dimensional fatigue crack propagation using synchrotron radiations and coupled this information with several 2D EBSD scans on the areas of interest. They prepared the sections of these areas of interest by conventional grinding and polishing, although during serial polishing, the presence of a plastic zone around the crack increases the tendency of the crack to be closed by abraded material. To avoid this unwanted effect, Herbig et al. [35] used DCT for crystallographic characterization prior to deformation. DCT is capable to measure 3-D grain shape and orientation in many polycrystalline material systems, but it is only possible to be performed on the initial grain structure before the plastic deformation.

Investigation of the influence of crystallography on creep damage can be done at the moment only with destructive techniques. To be able to draw statistically founded conclusions it is necessary the development of an improved method capable to observe damage on large material sections and the combination of voids image with local crystallography (EBSD) is desired. Before introducing the method developed during this thesis the state-of-the-art of power law creep damage is revisited.

II.3 Experimental results on creep damage

II.3.1 Creep voids: From visualization to quantification

Tomographic studies of void growth have already been performed during tensile deformation at room temperature on a dual phase steel [62] and a model composite [63]. Both of them obtained lower growth rates for the average void than what predicted by the Rice and Tracy models [64]. They have shown, however, that a good agreement exists for the largest voids (namely for the “mean void” calculated as a partial average over the 50 largest voids).

Using synchrotron X-ray CT combined, coupled with in situ tensile deformation Weck et al. [65] and then Hosokawa et al. [66] investigated the effect of stress triaxiality on void growth and

coalescence in model materials. The specimens contained a pair of notches. They have measured the principal diameters of the voids and showed that the void growth along the notch direction was much faster. They have found that for some single-layer model materials, the void linkage process is accelerated along the notches.

Pyzalla et al. [67] and later Isaac et al. [68] investigated in situ cavity growth in creep-deformed brass at high temperatures. One important result of their work shows that the average cavity volume grows exponentially with creep time. It was revealed that cavity size distribution depends on the time. The characterization of cavity shape and spatial distribution showed that the cavities become more and more elongated perpendicularly to the loading direction. This feature was related to cavity coalescence, which became dominant at the latest stages of creep.

Using a void tracking method, growth and coalescence of single voids was observed (Figure II-11).

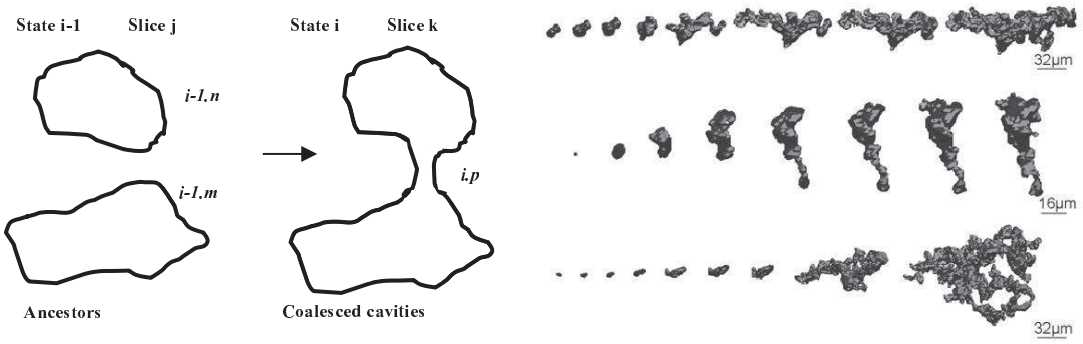

Figure II-11 (left) Schematic drawing for detection of coalescence (right) Shape evolution of three cavities exhibiting growth and finally coalescence of brass voids. [69]

It was shown that cavity coalescence takes place by plastic strain localization in the region between voids. They have shown the existence of a critical value of the inter-void ligament.

Sket et al. [70], [71] focused their work on the role of the local temperature in the development of spatially inhomogeneous strain, strain-rate and damage. In situ tomography, made it possible to correlate the local material characterization with a constant temperature gradient along the gauge length.

Using synchrotron X-ray nano-tomography with high resolution reconstruction (1 voxel = 50^3 nm^3), Dzieciol et al. [29] showed that cavities in recrystallized copper are nearly spherical, but that their shape changes during creep into a complex one with well-defined facets. This faceted shape can be understood in terms of dislocation glide on preferential slip planes.

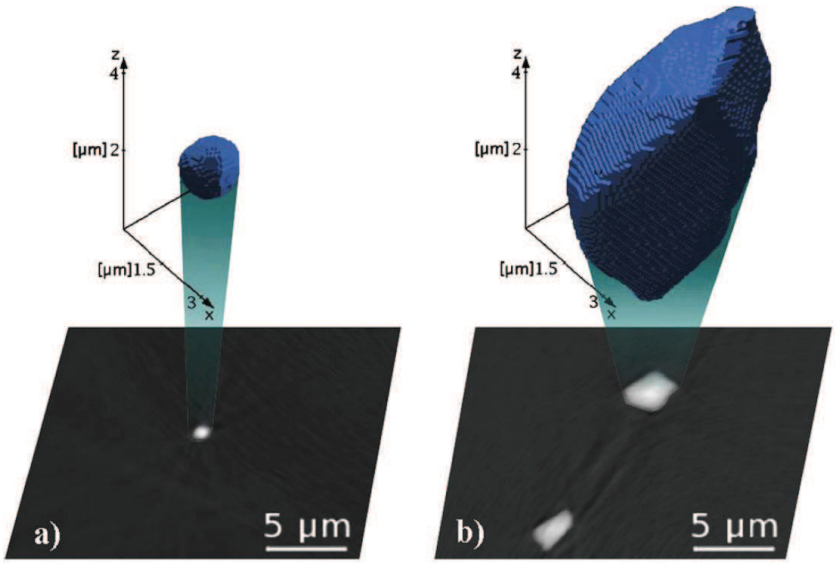

Figure II-12 Sub-micrometer resolution reconstructions of void shape. (a) A spherical shape is characteristic of the initial, recrystallized state. (b) Larger voids become faceted after 4% of creep deformation at 723 K. [29]

They have also shown that the real growth rates of voids during power-law creep of copper are much higher than the prediction of the nonlinear viscous material model of Budiansky et al. [28] by a factor of about 40. This faster growth is attributed to excessive dislocation glide (eventually coupled with surface diffusion) taking place at the void surface and leading to void faceting. It was suggested that, further studies linking growth rates to local crystallography would reveal more details of the true void growth mechanism.

II.3.2 Creep voids: Correlation to local crystallography

Hong et al. [72] studied the relationship between the grain boundary characteristics and the formation of grain boundary carbide precipitation. They observed that the increase in the misorientation between two adjacent grains correlates with carbide morphology. Then the cavitation behavior was investigated using a correlation technique. This was performed on the creep voids and it was observed that cavity formation is more pronounced at random boundaries that at coincidence site lattice (CSL) boundaries.

Combining EBSD and serial sectioning, Wahab et al. [73] reported to find more voids in steel at the interface between two grains than at the interface between a grain and a precipitate. In another work, Wahab and Kral [57] categorized the creep voids based on their location regarding to the grain boundaries and correlated the void location to void shape. The voids have then been divided to three categories as shown in Figure II-13.

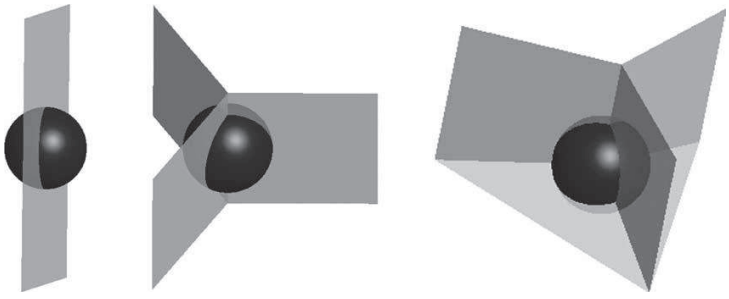

Figure II-13 Schematic representation of void location classification (left) simple boundary pore (middle) triple boundary pore and (right) void situated on quadruple boundary [57].

Despite the fact that the number of the pores on simple grain boundaries was higher, the total volume of the voids at this location was observed to be less than one tenth of those located at triple or quadruple boundaries. The explication was suggested to be that creep voids are most likely to nucleate first at the triple or quadruple boundaries, where there would be more vacancies. Moreover, they suggested that the occurrence of large voids at these locations are consistent with the current belief that void nucleation and growth takes place due to grain boundary sliding along geometrical irregularities at grain boundaries, where stress concentration is high. This would lead to more severe creep damage.

Wahab and Kral [57] have also studied the orientation relationship (OR) between the voids and the surrounding precipitates and the austenite matrix and found that most of the voids are adjacent to precipitates with a random OR with regard to the surrounding austenite matrix.

II.3.3 Creep voids: quantification of boundaries having a pore

Mahadevan and Casasent [74] presented a new technique based on image analysis for the detection of triple junction properties. In this technique grain boundaries are revealed using a chemical etching technique. Then they are imaged using a scanning electron microscope. Each image is segmented to separate the pixels of the matrix from those of the grain boundaries. Applying a series of filters on the segmented image, they could identify pixels in a junction of three grains as triple junctions. Further, they have: i) calculated the dihedral angle between each pair of grain boundaries and ii) detected the orientation of points near the triple junctions by analyzing the EBSD patterns there.

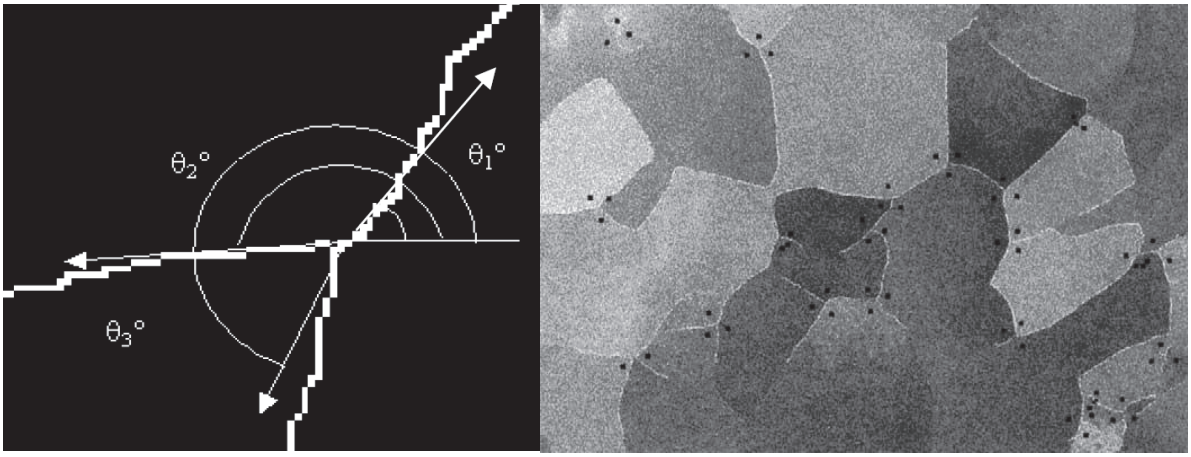

Figure II-14 Detection of the triple junctions and (left) calculating the dihedral angles (right) by acquiring EBSD patterns in their neighbourhood [74]

In the reality true grain boundaries could only be reliably revealed using EBSD scans and not by chemical etching. Using this technique, we can obtain information about the local orientation. So technically, we can characterize grain boundaries based on the disorientation between their neighbor grains (one angle for a simple boundary and three in case of a triple junction). Up to this date, this method was never applied to any creep deformed microstructure. Theoretically, applying it to all boundaries and comparing all boundaries to those containing a void should clear some facts about the dependency of void nucleation on local crystallography.

II.4 Objectives of this thesis

The principal objective of this research is to correlate the nucleation and growth of creep cavities to the type of GBs and to local crystallography.

In order to achieve this a statistical analysis on a large, representative material will be performed. This size limit along with the fact that we need the crystallographic information on deformed samples imposes using a destructive observation method, namely: serial sectioning combined with EBSD. In order to obtain an improved representation of the 3D microstructure the conventional serial sectioning technique will be combined with an accurate profilometer system in order to obtain a high spatial resolution in 3D and to avoid to reconstruction of artifacts related to non-parallel polishing of the microstructure. Some advantages of this new method are:

- Observation on a large field of view and in the mean time maintaining a high resolution
- Accurate measurement of the removed material thickness
- Updated procedure of data analysis, using an advanced image processing technique
- Damage observation by advanced methods of electron microscopy
- Combination of surface roughness information with microstructure

III.1 Thermomechanical treatments

III.1.1 Material

Damage during high temperature creep was investigated in oxygen free high conductivity (OFHC) copper (99.99% purity). The material was provided in the form of the bars with 2 cm of diameter. The bar diameter was reduced by 70% in 4 passes using a rotary hammer. Two types of samples were then machined with particularly reduced sections of the gauge length. Their diameter was 1.0 mm and 1.8 mm and they were used for in situ and ex situ tomography measurements, respectively. The dimensions of the samples are shown in Figure III-1.

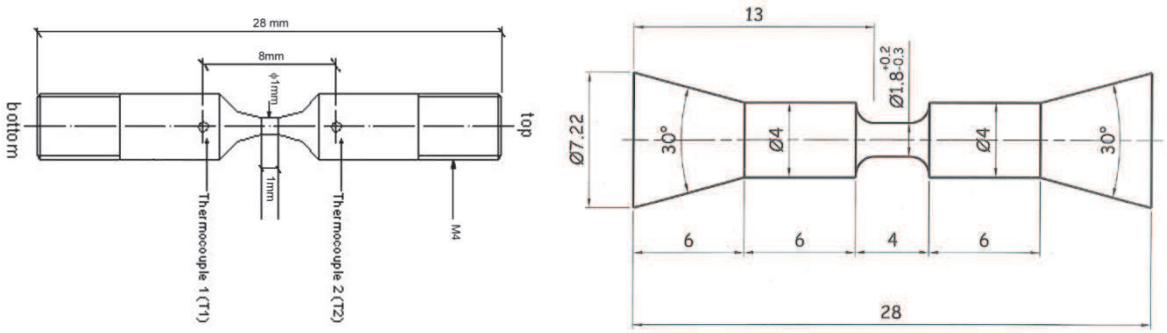

Figure III-1 Schematical drawing of sample dimensions used for in situ (left) and ex situ (right) tomography measurements

Once the samples machined, their surface carefully polished to remove any surface damage. This was obtained with P2500 and further by P4000 grit abrasive papers. In this state the reduced section gets a mirror-polished shining outlook as the high rugosity caused by machining was removed.

The samples were then put into sealed silica tubes under vacuum to prevent their oxidation and heat treated at 550°C for 24 hours and then furnace cooled. This treatment led to recrystallization of the samples which had an average size of about 40 µm. The grain size was determined from EBSD maps as the equivalent circle diameter.

III.1.2 In situ creep test

To perform tensile creep tests, two types of machines were at our disposition, the first one is a miniaturized device, shown in Figure III-2. In this device, the force is applied using two springs (made of steel 1.1200 Class C) and measured with a loading cell. When the springs are compressed the load is transferred to the sample through the load cell, which measures the actual load applied to the specimen. The whole loading system is mounted on a ceramic tube with good creep resistance at high temperatures and it is transparent to high energy beams. By a proper selection of the spring constant, nearly “constant-load” or “constant-stress” conditions can be applied [71]. Also the total displacement of the sample was measured by an inductive displacement transducer placed at the top of the device.

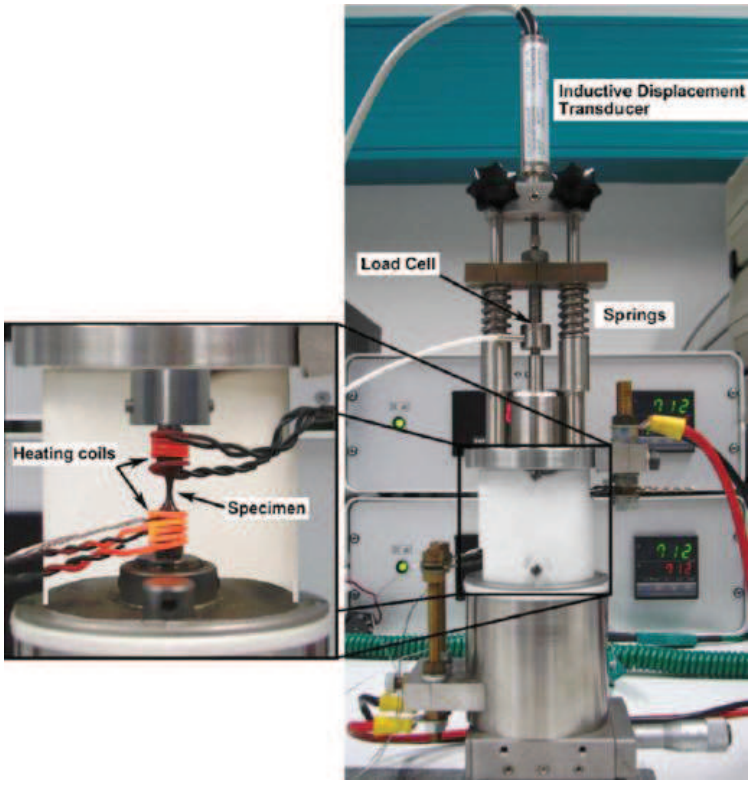

Figure III-2 Miniaturized creep machine

Cylindrical specimens of 1 mm in diameter and 1 mm in gauge length (as shown in Figure III-1 left) were creep deformed under uniaxial tension using this miniaturized creep machine mounted on the goniometer used for tomography scanning. Two coils placed at the top and bottom of the sample allow setting up a homogenous temperature in the gauge length. To keep the temperature measurement within the error of 1 K, a PID (proportional-integral-derivative) controller was used. However, the local strain and strain-rate of the samples was evaluated from 3D tomographic reconstructions through image correlation. Three samples were creep deformed at temperatures of 573 K, 723 K and 773 K, respectively. The samples were partially protected by a thin layer of Boron Nitride, which is a high temperature protection powder (at temperatures below 1000°C).

III.1.3 Creep test under high vacuum

The second machine at our disposal was a home-made one, built on a tensile testing machine frame. The sample is at the interior of a quartz tube and is protected against oxidization by creating a good vacuum. This machine is equipped with two vacuum pumps; the first one is a rotary pump, which allows reaching a medium level vacuum. Once this level achieved the second turbo molecular pump enables reaching a high vacuum (10^{-10}-10^{-11} MPa). Since the sample should be closed in the tube, but mobile a metallic welded bellows was used to close the tube from below. This insures the connection between mobile and static parts. A constant charge was then applied through the mobile part to the sample and the displacement of the sample was measured on an extension rod using two LVDT sensors (Figure III-3).

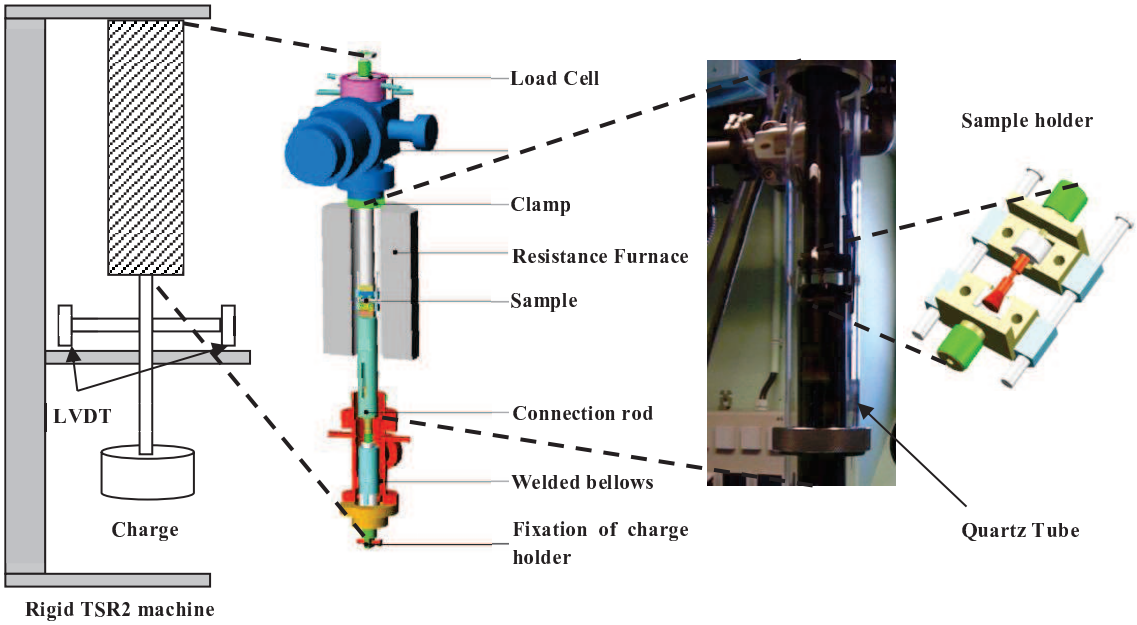

Figure III-3 High vacuum creep machine

The high temperature is applied to sample by a resistance furnace which covers the external side of the transparent quartz tube. The turbo-molecular pump and the whole upper and lower parts of the assembly were cooled by a closed recycled water circuit system. Therefore the thermal stability should be fully reached before starting the test.

Six specimens were creep deformed; three of them at 573 K under 80 MPa and three at 773 K under 10 MPa. The tests were interrupted in the end of the first, in the middle of the second, and at the beginning of the tertiary creep stage, respectively. The creep conditions (temperature and strain) were chosen in agreement with the aim of ex situ investigations related to the influence of the strain rate on the location of creep cavity nucleation sites, namely at simple boundaries and triple junctions. According to the creep deformation maps of Frost and Ashby [75] both experiments are in the power law creep region, but at 573 K cavities grow mainly by creep plasticity, while at 773 K by GB diffusion.

III.2 Characterization techniques

III.2.1 Computed tomography

The purpose of a computed tomography (CT) system is to build a 3D image of the inner structure of an object from a set of projections acquired in different directions. In case of absorption CT the parameter that is reconstructed in order to represent the structure is the linear attenuation coefficient (μ) of the object. The physics of X-ray radiography is based on Beer-Lambert law which relates the ratio of transmitted intensity (I) to incident intensity (I_0) to the integral of the linear absorption coefficient of the material μ along the path L (Equation III-1).

$$-ln\left(\frac{I}{I_0}\right) = \int_L \mu(x,y,E)dx \qquad \text{Equation III-1}$$

μ depends on the material and the X-ray energy, so for a polychromatic beam the Equation III-1 has to be integrated over the whole energy spectrum.

III.2.1.1 Principles of tomography

The basic tomographic setup consists of the following elements:

- The X-ray source: can provide parallel or conical beam
- A goniometer: is an instrument that rotates the sample to a precise angular position.
- A scintillator which transforms X-rays to a visible light photons necessary for a CCD camera
- A 2D CCD camera recording the projections
- A PC for controlling the stage and the camera

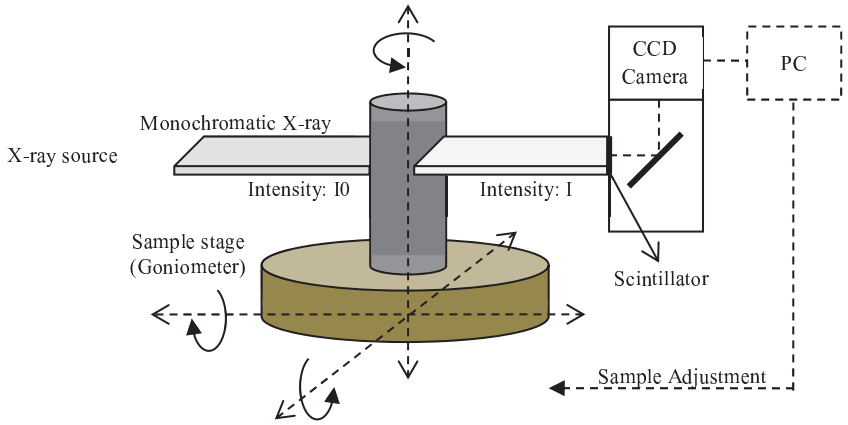

Figure III-4 Main elements of tomography setup

Usually micro-focus X-ray tubes are used as laboratory X-ray sources. They consist of anode and cathode. A heated tungsten filament supplies electrons which are accelerated by a high tension and are bombarding the anode. The X-ray spectrum depends on the anode material and the accelerating voltage.

In this work, however, synchrotron radiation was used for measurements. Synchrotron light is produced by charged particles (electrons) circulating in a ring at almost the speed of light. Electrons are deviated by the magnetic field of the bending magnets distributed all along the circumference. When the electrons are forced on a circular trajectory, emit the synchrotron light tangentially to their trajectory. The synchrotron light follows a straight direction towards the beamlines that are installed in the experimental hall. A beamline is composed of a series of hutches. The first one is usually the optics hutch and comprises such instruments as slits and filters, mirrors and monochromators. Close to it is the experimental cabin with the sample for study and the detector. At the end we find the control cabin. On computer screens one can monitor the experiment and the data acquisition. A schematic drawing of the synchrotron beamline components are presented in Figure III-5.

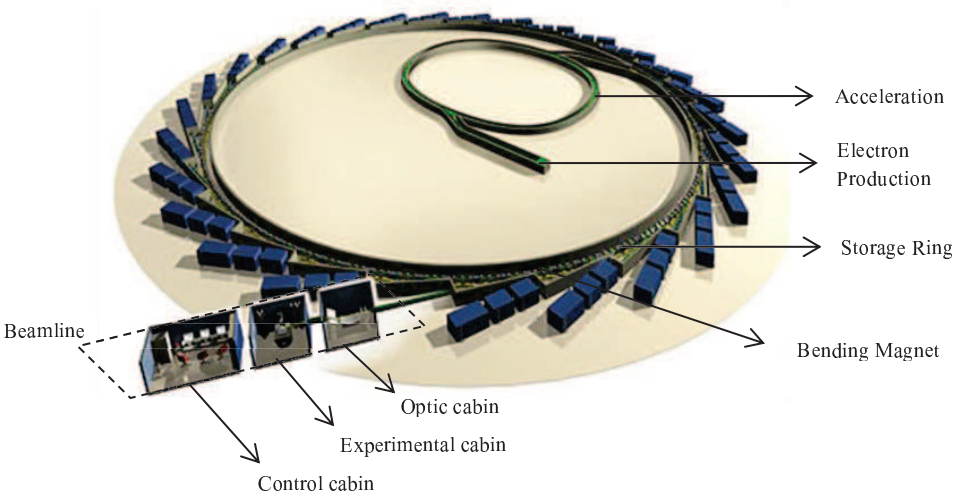

Figure III-5 Synchrotron components[76]

The use of synchrotron radiation in material science is due to its excellent properties:

- High brilliance, the intensity of radiation emerging from storage ring can be of the order of a billion times greater than radiation from a typical laboratory X-ray source.
- Wide tunability in energy/wavelength by monochromatization (sub eV up to a few hundred keV).
- Highly polarized radiation
- The coherency of the beam
- Time structure, radiation is pulsed typically 10 to 100 picoseconds in length separated by 10 to 100 nanoseconds.

For the objective of this thesis the tomography was performed at the ID15 beamline of the European Synchrotron Radiation Facility (ESRF). Thanks to the available high X-ray flux ID15 is the fast tomography beamline allowing to perform in situ measurements. To achieve this objective the investigated sample was mounted in the miniaturized creep device and positioned on the goniometer used for tomography. Then the creep test was started and tomographic scans were acquired several times during the creep, typically after every 30 minutes. From the three dimensional reconstructions the pores were extracted for analysis. The analysis is composed of several steps like labeling, quantification, shape definition and 3D visualization (will be described in the following chapter).

III.2.1.2 Reconstruction techniques

Because the projections contain superimposed information of a volume in a 2D plane the estimation of the absorption coefficient distribution of the object needs many projections. For every angular position θ, a 2D projection image is stored. The cross section of the object (slice) to be reconstructed is called $f(x,y)$ and a parallel projection of this object at the angle θ is denoted by $p(t,\theta)$, where t is the distance from the projected ray to the center of rotation (as shown in Figure III-6).

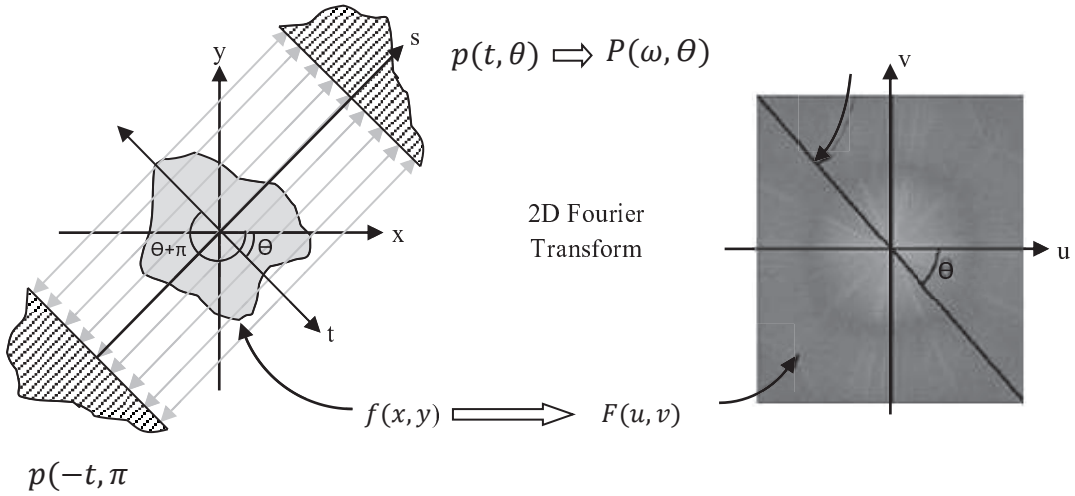

Figure III-6 Principle of tomography and illustration for the Fourier slice theorem. The object f(x,y) is represented in the rotated coordinate system by f'(s,t)

Once the projections are recorded, the next step is to perform the tomographic reconstruction. This is done using the inverse Radon transform. In case of parallel beam geometry, a condition that can be met at synchrotron sources, 180° rotation is sufficient to represent the Radon transform since:

$$p(t,\theta) = p(-t,\theta+\pi) \qquad \text{Équation III-2}$$

The mathematical theory governing the tomographic reconstruction is generally known as the Fourier slice theorem [77]. It states that the Fourier transform of a parallel projection $p(t,\theta)$ of an object $f(x,y)$ obtained at angle θ is identical to a section in the two-dimensional Fourier transform of $f(x,y)$ taken at the same angle:

$$P(\omega,\theta) = F(u,v)_\theta \qquad \text{Équation III-3}$$

where $P(\omega,\theta)$ denotes the Fourier transform of $p(t,\theta)$. This is illustrated in Figure III-6.

Although the Fourier slice theorem provides a straightforward solution to the reconstruction problem, it has some inconveniences in actual implementation such as interpolation in the frequency domain or implementation of the targeted reconstruction. Therefore, alternative approaches also exist, the most popular one being the Filtered Back Projection (FBP) algorithm.

The idea of the back projection relies in assigning to each point of the object the average value of all the projections that pass through that point. The back projected image is, however, a blurred version of the original object. An exact mathematical correction of the back projection smoothing effect can be performed by an appropriate pre-filtering of the projections leading to the FBP algorithm (illustrated in Figure III-7).

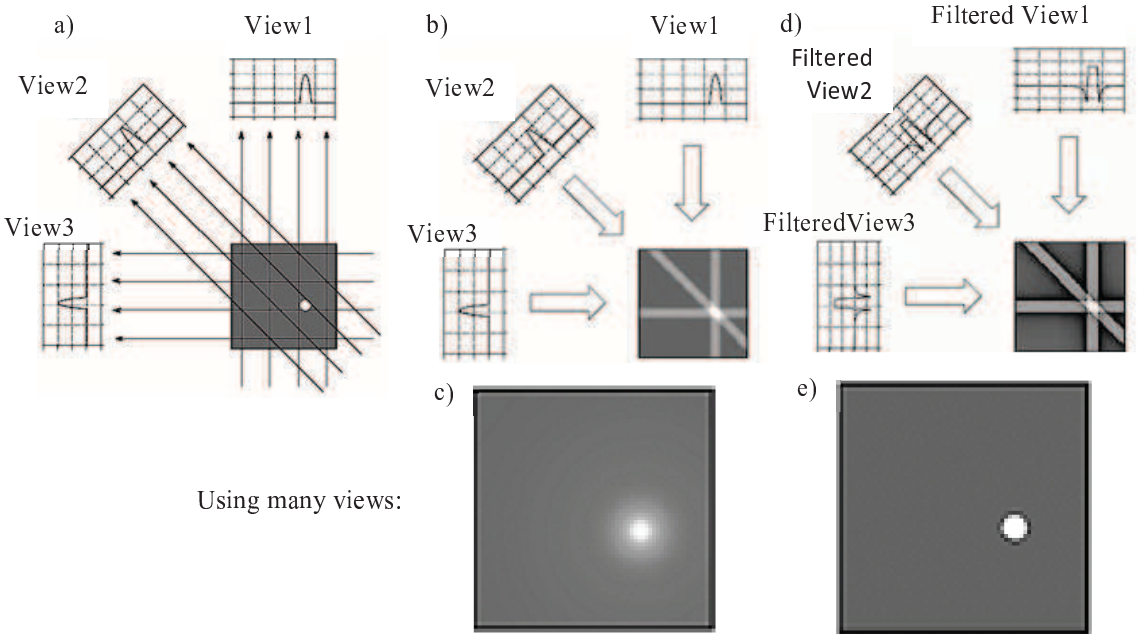

Figure III-7 (a) Projections acquired at three views (b) back projection using three views or (c) many views-giving blurred results (d) filtered back projection using three or (e) more views-more realistic result [78]

Based on the Fourier slice theorem and the symmetry property of the parallel sampling geometry the reconstruction formula can be rewritten as shown in Equation III-4.

$$f(x,y) = \int_0^{\pi} \int_{-\infty}^{\infty} P(\omega,\theta)|\omega| e^{j2\pi\omega(x\cos\theta + y\sin\theta)} d\omega d\theta \qquad \textbf{Equation III-4}$$

The inner integral is the inverse Fourier transform of the quantity $P(\omega,\theta)|\omega|$ which represents the Fourier transform of a projection filtered by a function whose frequency domain is $|\omega|$ (ramp filter). The ramp function $|\omega|$ emphasizes high-frequency contents and consequently the high-frequency noise. Different types of windows can be applied to shape the filter's frequency response and hence modify the noise characteristic to the reconstructed images. All tomographic volumes evaluated in this thesis were reconstructed using the FBP algorithm integrated in a home-developed software [79].

The quality of cavity detection depends to the quality of the reconstruction. Figure III-8 presents some results of the reconstructed sections for the same, creep deformed sample. Cavities are shown with a red contour.

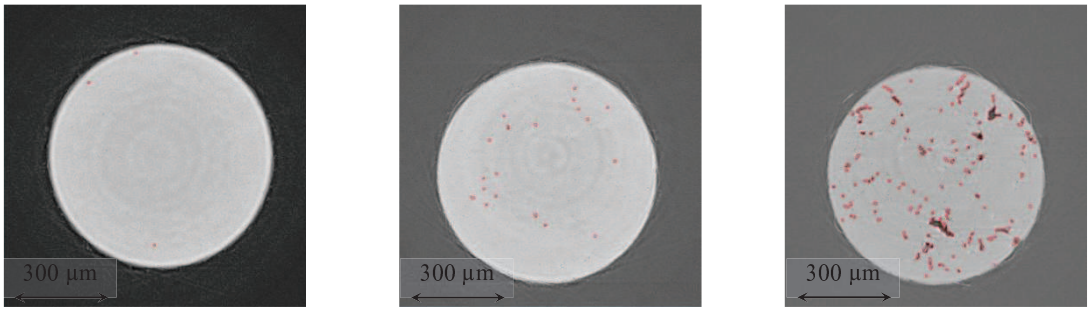

Figure III-8 Tomographic reconstructed slices of the same sample creep deformed at different strains - cavities are marked with a red contour

III.2.2 Scanning electron microscopy observations

The creep deformed samples under high vacuum were observed in a destructive way using scanning electron microscopy (SEM). The SEM is a microscope that uses electrons instead of light to form an image and it has many advantages over traditional optical microscopes: it has a large field of depth, which allows more parts of a specimen to be in focus at the same time. It has a much higher resolution and because the SEM uses electromagnets as lenses, there is much more control in the degree of magnification.

III.2.2.1 Principles of electron microscopy

In an electron microscope the image is formed step by step by the sequential scanning of the sample with the electron beam. The electron beam is created using an electron gun, then focalized using condenser lenses, scan coils and the objective (Figure III-9). So the beam converges on a spot form where the information will be extracted. The scanning coils are responsible to move the beam to a second spot and so on we can scan a line or the surface. Then the image is saved in a digital form (a matrix of the points) using gray levels. The image contains information about the surface of the sample, characteristic for a layer with the depth varying from about 1 nm to 1 µm. Finally the contrast of the image depends on the re-emission of the secondary or back scattered electrons.

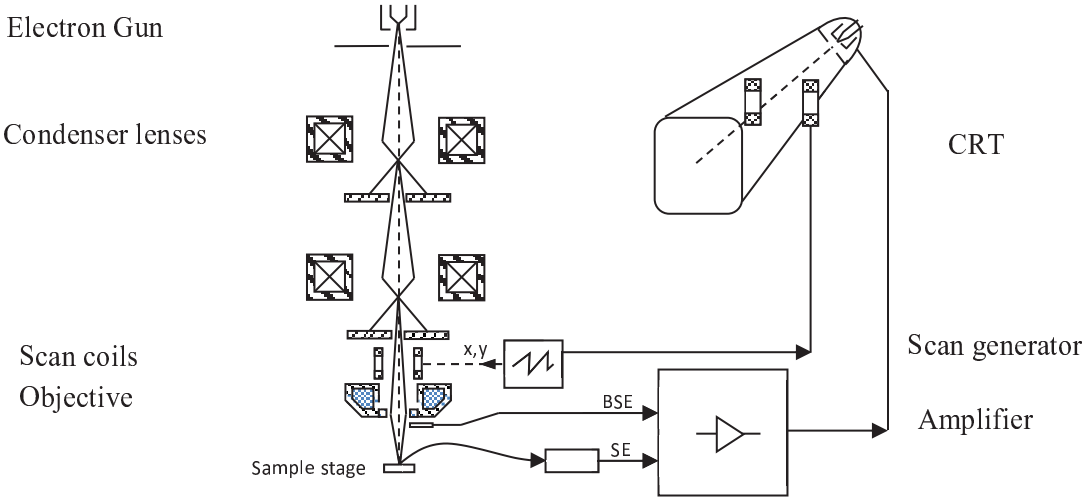

Figure III-9 Image formation in low-voltage scanning electron microscopy[80]

In order to understand the image formation and the image contrast it's necessary to take a deeper look at the electron-matter interaction and to the origin of secondary and back-scattered electrons. This helps us to decide the choice of detector and the acquisition resolution to obtain an image adapted to our needs.

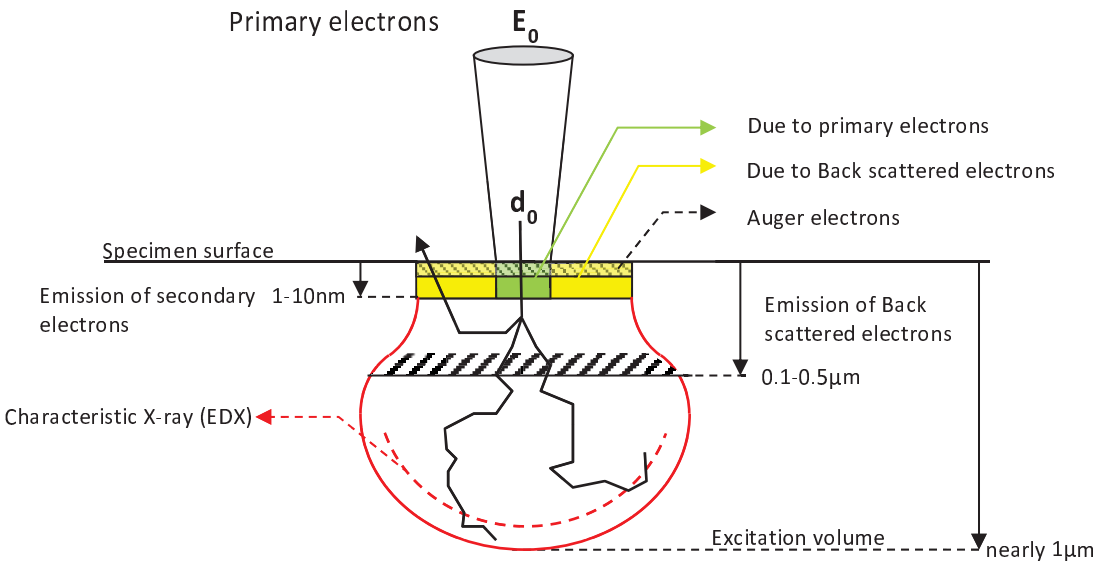

Figure III-10 Interaction of electron beam with the matter (thickness depends to beam parameters and material characteristic) [81]

Electrons accelerated onto a material result in a number of interactions with the atoms of the target sample. Accelerated electrons undergo elastic and inelastic scattering, which results in a number of signals that are used for imaging and obtaining quantitative or semi-quantitative information on the target. Typical signals used for imaging include secondary electrons (SE), BackScattered Electrons (BSE), Auger electrons and characteristic X-rays.

Where an electron beam impinges on a sample electron scattering and X-ray production develops in a volume (the electron interaction volume) that is dependent on several factors (Figure III-10), which include:

- The energy of the incident beam (accelerating potential) increases the interaction volume, but decreases the elastic scattering (e.g. backscattering)
- The interaction volume decreases as a function of the mean atomic weight
- Smaller and more asymmetric interaction volumes develop in samples tilted relative to the direction of the electron beam.

Each signal used for imaging or elemental analysis is generated in different electron interaction volumes and, in turn, each of the signals has different imaging or analytical resolution. Auger and secondary images have the best imaging resolution being generated in the smallest volume near the surface of the sample. Backscattered electrons are generated over a larger volume resulting in images of intermediate resolution.With an accelerating voltage of 10-30 kV, and incidence beam currents of 1-50 nA, electrons diffract from the zone of BSE electrons in the excited volume under the incident beam. The spatial resolution of the technique is governed by the SEM electron optics as in conventional BSE imaging. For high resolution imaging, high performance FEG-SEM or Field Emission Gun SEMs are required, along with small samples and short working distances. But before any observations the sample should be properly prepared.

III.2.2.2 Sample preparation

Sample preparation for SEM observation requires a delicate and careful handling. It starts by cutting the sample at reduced section. The cutting procedure is performed using a dicing saw. The

dicing saw employs a high speed spindle fitted with an extremely thin diamond wire (D~100 µm) to avoid any plastic deformation on the sample. The cut region is extremely small and difficult to manipulate. So, it should be embedded in a protecting resin.

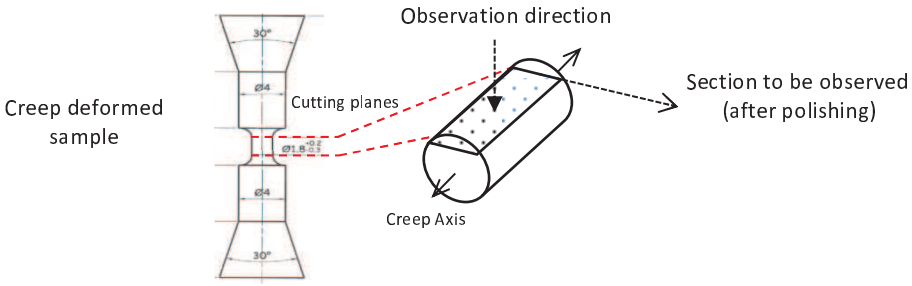

Figure III-11 Sample preparation for SEM observations

As the operation of SEM needs the local spot, affected by the electron beam to be discharged after analysis, the protection resin should be able to conduct the electric current. Also one should avoid exposing the sample to high pressure or high temperature (which is necessary for hot resin mounting). So the solution is to use a cold epoxy resin; with a mixture of Ni based acrylic powder additive (Buehler model 20-8500) that makes the resin conductive.

Initial mechanical polishing was applied on the samples using a LAM-PLAN automatic polisher using the following procedure:

1. Polishing with P400 grit SiC abrasive papers up to arrival to the desired section. (can take up to 40 minutes regarding to the hardness of the resin)
2. 15 minutes of polishing on a LAM-PLAN Cameo Silver plate using 9µm diamond solution.
3. 15 minutes of polishing on a LAM-PLAN Cameo Gold plate using 3µm diamond solution.
4. 5 minutes of polishing on a flocked tissue using 1µm diamond solution.
5. 15 minutes of polishing on a woven tissue using 1µm diamond solution.

The final polishing stage is not necessary for normal observations, but it eliminates the plastically deformed layer formed because of the first steps of polishing. There are three major solutions:

1. Electrochemically polishing the surface by A2-struers solution under 15V tension for about 30 seconds (tension and polishing time depends to sample size).
2. Mechanical-chemical polishing by colloidal silica particles for 15 minutes.
3. Ion etching for 7 minutes under 5.5 keV acceleration voltage which passes an ion current of about 250µA through the sample at an incidence beam of 20° with a sample rotation of 60 rpm.

III.2.2.3 Acquisition conditions

Once the samples prepared they are placed in a Zeiss Supra55VP FE-SEM chamber. Imaging is done at a relatively low working distance (10 mm) from the output of the electron gun. Two images were acquired with BSE and SE by focusing on the sample at the exact working distance which covers 1139 x 854 μm^2 at a magnification of X264. The acquisition grid was set to the highest spatial resolution which gives 3072x2304 pixels in each direction. This gives a spatial resolution of 0.371 µm in each direction. Scan speed was lowered to 2.54E-5 seconds per pixel

which gives the acquisition time of 3 min per image. These acquisition conditions allow covering the entire analysis surface without any mechanical movement of the stage.

As it can be observed in Figure III-12, the same area is imaged using SE and BSE detectors. In both images the copper matrix contains creep cavities which are seen as dark zones. For reasons of image analysis the image obtained by BSE detector is sharper and has a higher gradient of grey level gradient between the pixels describing the cavities and the matrix.

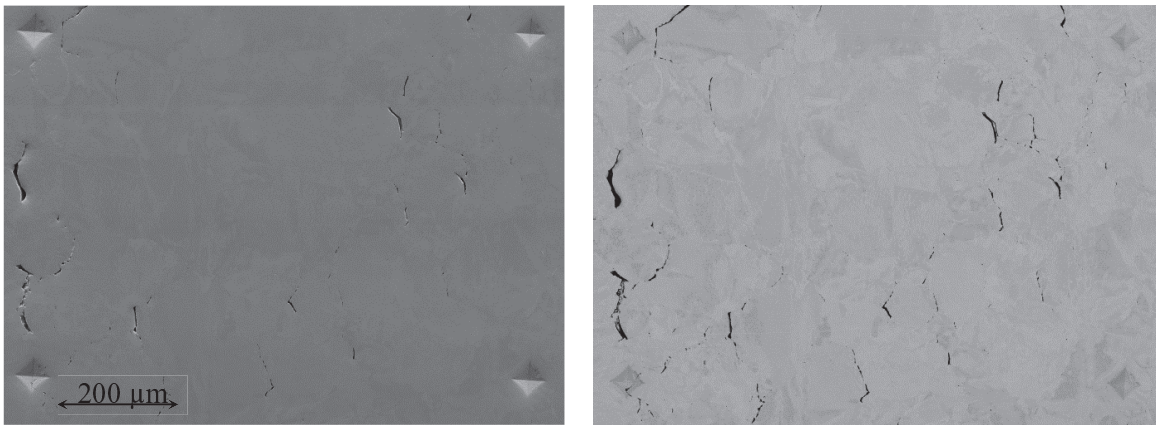

Figure III-12 SEM images obtained on a creep deformed sample with cavities inside the matrix - same zone imaged by (left) secondary electrons and (right) back scattered electrons

III.2.3 Surface topography – Optical Profilometer

As it will be discussed in chapter V, surface topography has a crucial importance in the accomplishment of the 3D reconstruction with the new serial sectioning technique. For the objectives of this thesis a 3D optical profilometer type Wyko NT 9100 was used. An optical profilometer is similar to a conventional microscope; its construction is presented below:

White light passes through a beam splitter, which directs it towards the sample surface and a reference mirror (Figure III-13). When the reflected light from these two surfaces is recombined, it forms a pattern of interference "fringes". Either the test surface or measurement head is scanned vertically such that each point on the surface passes through focus. A series of algorithms are applied to precisely map the height of each point on the surface.

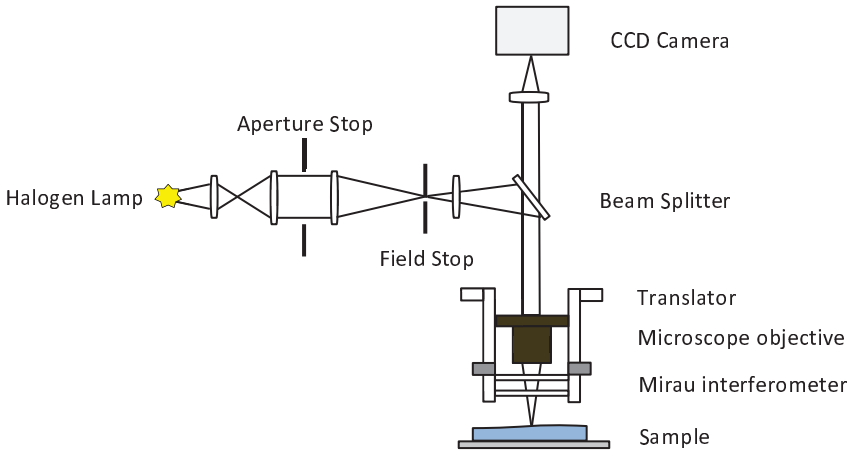

Figure III-13 Principles of optical profilometer

Two types of objectives were available on the profilometer used, which gave the following properties of the image:

Magnification	Working distance (mm)	Maximum slope (°)	Spatial resolution (µm)	Field of view (mm x mm)
X10	7.4	7.6	1.8	1.15 x 0.86
X50	3.4	26.7	0.37	0.23 x 0.17

Table III-1 Objectives at disposition on the Wyko NT 9100 optical profilometer

Two options are also available for reducing the noise level during the acquisition:

1. The modulation threshold: this parameter is a signal-to-noise discriminator that determines whether the data of a pixel is valid or not according to its fringe modulation level. When the maximum modulation level of a correlogramm is higher than this threshold, the data of that pixel is considered valid. Data points that are marked as invalid are not considered during the analysis. In summary higher values of modulation threshold lead to more reliable measurements but at the cost of the less number of points where the surface is calculated. The less the number of points are captured, the more interpolation is needed to cover the entire surface.
2. The averaging option combines several consecutive surface measurements at one location to obtain a single final result. Such averaging also helps lowering the noise in the measurement. If the noise is random (as is often the case in stable environments) the noise level decreases as the square root of the number of scans. Typically averaging 4-9 measurements produces noticeably better results on smooth surfaces.

The theoretical resolution of the height measurement according to the manufacture is about 0.2-1 nm. But this resolution can hardly be achieved at that scale because the level of the noise is much higher. In order to evaluate the maximum error of the surface reconstruction with each objective the surface is measured twice (each time averaged over 4 measurements) and the result of each point is then subtracted from the previous measurements and a “difference image” is obtained. As it is shown in Figure III-14, the maximum error for X10 objective is about 1.270 µm and for X50 0.521 µm. It can be also observed that the maximum error occurs where the local slope regarding to surface is higher.

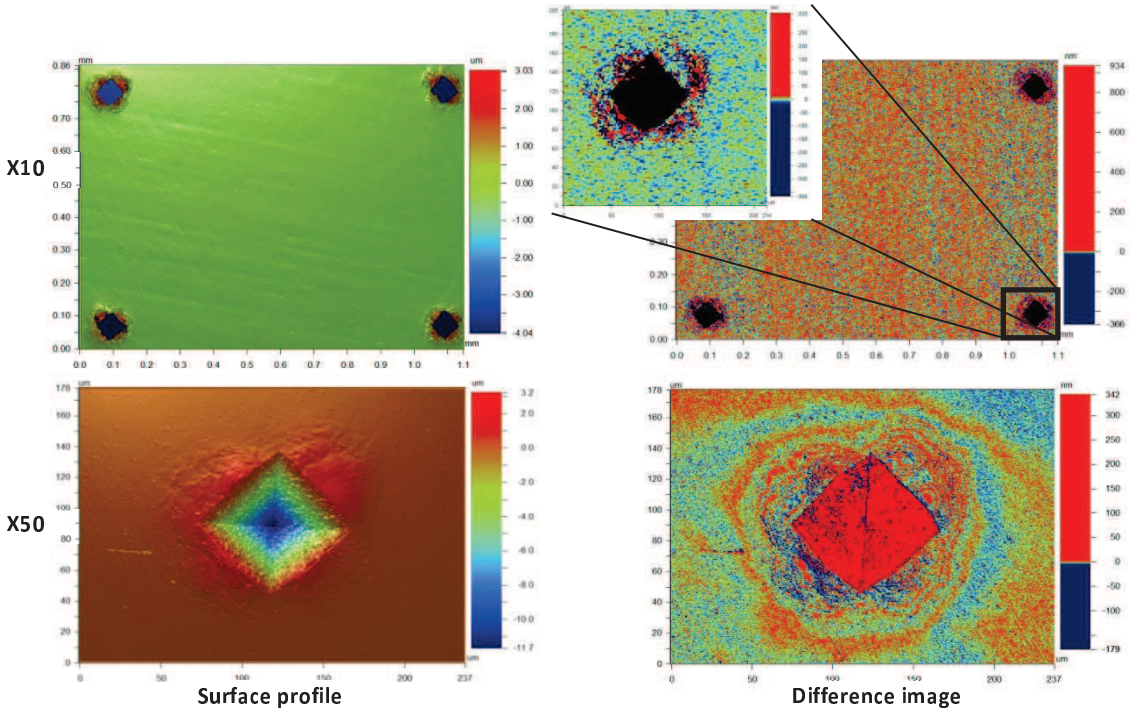

Figure III-14 Example of surface profile for each objective with their corresponding maximum error estimation

III.3 Crystallographic orientation

The majority of structural materials are made up of many crystals (grains), each of which has an ordered structure. These crystals all fit perfectly together to form a solid polycrystalline material. Although the structure within each of these crystals is ordered this is not aligned with the internal structure of the neighboring grains. This creates a grain boundary, which is an interface between two crystals whose atomic structures are not geometrically aligned. These crystals are said to have different crystallographic orientations relative to the sample reference frame.

Orientation of individual crystals (grains) within a polycrystalline sample can be described as the transformation (with the associated transformation matrix) of the sample coordinate system to the crystal coordinate system. Usually, the sample coordinate system is defined by elongation (ED), transverse (TD) and normal (ND) orthogonal directions, while the crystal's coordinate system is defined by the crystallographic cube directions [100], [010] and [001].

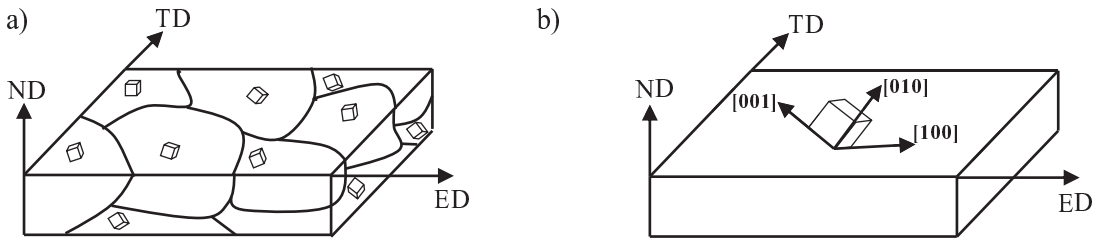

Figure III-15 Schematic representation of: a) polycrystalline microstructure depicting the different orientation of the crystals, b) sample reference frame and crystal frame inside the bulk material

The orientation matrix of a crystal relative to the sample frame can be represented in multiple ways. One of these is related to Euler angles $(\varphi_1, \phi, \varphi_2)$. There are also multiple conventions for representing these rotations, the most commonly used is the Bunge convention [82].

III.3.1 Electron backscatter diffraction (EBSD)

The analysis of diffraction patterns of back scattered electrons in a scanning electron microscopy (SEM) enables the determination of the local crystallographic arrangement of the microstructure. EBSD patterns are obtained by focusing the electron beam on a crystalline sample. The sample is tilted to approximately 70° with respect to the horizontal. This is usually done by tilting the SEM stage, which contains the sample holder. Tilting to 70° allows optimizing the number of electrons to be back scattered and oriented towards the detector. The diffracted electrons, which interfered constructively (corresponding to the Bragg's law) produce a diffraction band (Kikuchi bands).

$$2d_{hkl}.\sin\theta_{hkl} = n\lambda \qquad \text{Equation III-5}$$

Due to the short wavelength of the electrons the diffraction angles are small 1-2°, therefore the intersection of the diffraction cones (which are hyperbolas in reality) appear as straight lines on a phosphorous screen placed parallel to the incident beam. The phosphor of the screen interacts with diffracted electrons and emits light suitable to be captured by a Charge-Coupled Device (CCD) camera. The electron diffraction pattern (EBSP) produced on the phosphorous screen is projected on the CCD by an optical system similar to one used in X-ray imaging detectors. In the present case we call this detector an EBSD detector.

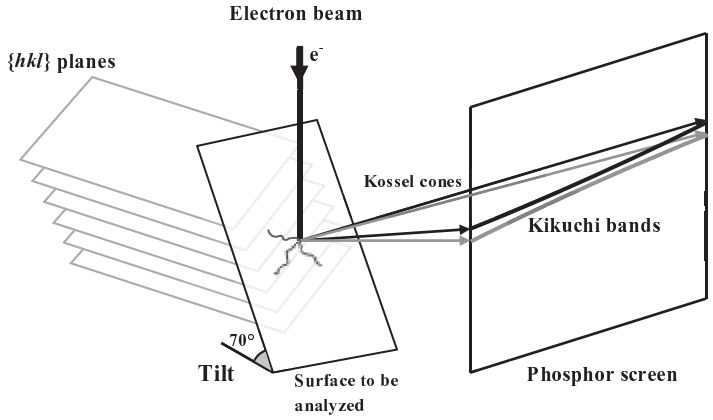

Figure III-16 Diffraction of the Back scattered electrons from the {hkl} planes and forming the so called Kikuchi bands

The bands in the pattern represent the reflecting planes of the diffracting crystal volume. Hence the geometrical arrangement of bands is a function of orientation of the crystal lattice such that:

a) The symmetry of the crystal lattice is reflected in the pattern
b) The width and the intensity of the bands are directly related to the spacing of the atoms in the crystallographic plane
c) The angles between the bands are directly related to the angles between the crystallographic planes.

III.3.2 Orientation determination

In order to determine the orientation, the diffracted patterns should be indexed. Indexation of the diffracted patterns takes place in a three-step process: a) Kikuchi band detection b) Kikuchi band identification or indexing of the pattern and c) determination of orientation.

Krieger Lassen et al. [83] were the first to suggest using the Hough transform to extract the bands. The Hough transform is applied to the Backscattered Kikuchi Pattern (BKP) image described previously. The equation governing the Hough transform is:

$$\rho = x\cos\theta + y\sin\theta \qquad \text{Equation III-6}$$

where (x,y) describes a set of pixel coordinates forming a line and the Hough parameters (ρ, θ) provide and alternative description as shown schematically in Figure III-17.

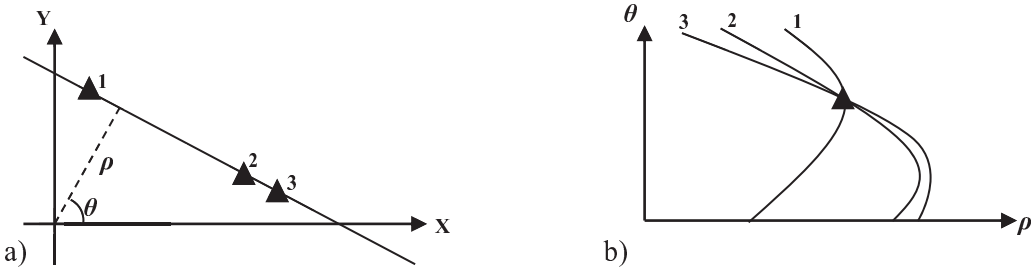

Figure III-17 Schematic of Hough transform parameters: (a) x-y space and (b) positive p portion of Hough space

By transforming an image into Hough space, lines in the image space become points in the Hough space. This is done by first dividing Hough space into discrete bins (for example 1° steps for θ and 100 steps in ρ from $-\rho_{max}$ to $+\rho_{max}$). The intensity at each x, y pixel in the image is then added into all corresponding bins on the curve defined by $\rho = x\cos\theta + y\sin\theta$ (where ρ is calculated for each discrete θ). The problem of finding a band in the diffraction pattern is then reduced to finding a peak of high intensity in the Hough transform. An EBSP image the corresponding Hough transform and the bands detected are shown below:

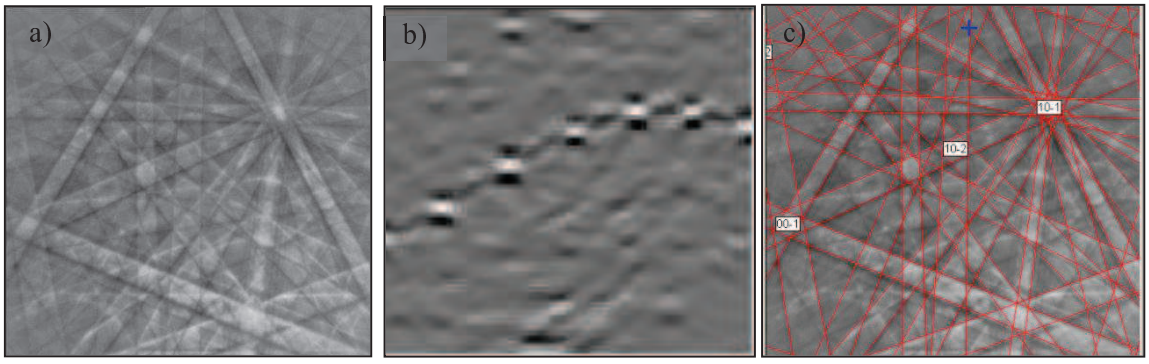

Figure III-18 (a) Collected EBSP (b) corresponding Hough space and (c) indexed EBSP

Once the bands have been detected, the reflecting planes associated with the detected bands must be identified. The width of the bands is a direct function of the d-spacing of the diffracting plane (Bragg's law) and is compared to a theoretical list of diffracting lattice planes. The angles between bands have to be determined and compared with theoretical values. The inter-planar angles between three intersecting bands are calculated and compared with the data from table in

order to decide their identity within the small tolerance, usually 1 to 2 degrees. Once the planes are correctly identified, zone axes are indexed from cross-product calculations of indexed planes.

Usually more than one possible solution can be found for every three bands and a parameter called Confidence Index (CI) is used, which is based on a voting scheme. In this procedure all possible sets of three bands are formed and the solution is based on the most probable indexing of the pattern, which is a function of setup tolerance between measured and theoretical inter-planar angles.

In the last step orientation determination is based on the calculation of the orientation of the corresponding crystal lattice with respect to reference frame. Often a sample reference frame is used and a sequence of rotations is applied to bring the sample frames into coincidence with the crystal lattice frame. Crystal orientation can be then defined by three Euler angels ($\varphi_1, \phi, \varphi_2$).

III.3.3 Orientation calculations

The orientation of the crystal is defined as the rotation of the crystal coordinate system with respect to the reference coordinate system. There are different, but equivalent orientation descriptors ranging from Euler angles to quaternions, etc. Each of these can be more appropriate from case to case. Functions make it possible to convert a descriptor into another, either directly (when possible) or through an intermediate descriptor. These conversions are very well described in different references and are implemented in some free access software such as Orilib [84].

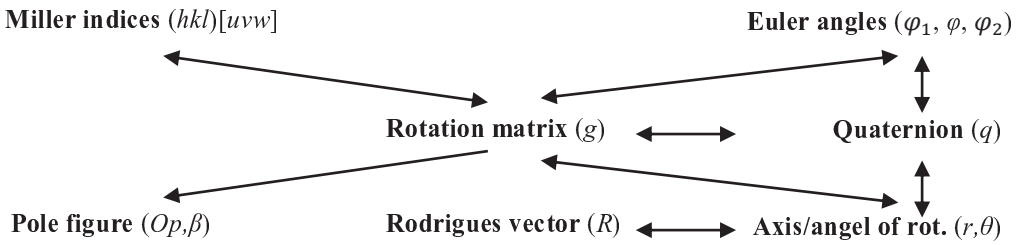

Figure III-19 Available orientation descriptors and direct conversions

This following section describes some mathematical functions performing calculations with orientations.

III.3.3.1 Misorientation – Disorientation

Let g_1/q_1 and g_2/q_2 be two orientations. The misorientation between the two orientations is defined as the rotation that brings one orientation to the other. The misorientation is commonly expressed in the reference coordinate system.

$$g_m = g_1^{-1} g_2 \; or \; q_m = q_2 q_1^{-1}$$

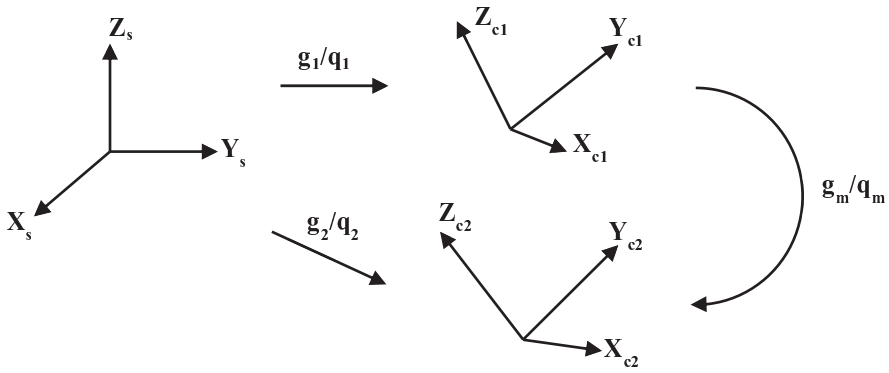

Figure III-20 Misorientation between two crystals

Actually, due to crystal symmetry, there are several misorientations g_{mi} with $i \in \{1, \ldots, n\}$, which are obtained by replacing orientation 2 by its n-th crystallography-related orientation. The disorientation g_d/q_d, is defined as the misorientation with the minimum angle of rotation.

III.3.3.2 Mean orientation

An expression for the mean orientation has been proposed by Humphereys et al [85]; and more generally by Glez and Driver [86] using quaternions. The main expression for the mean orientation for the set of orientations is as given by Equation III-7:

$$q_{mean} = \left(\sum_{i=1}^{n} q_i\right) / \left(\left|\sum_{i=1}^{n} q_i\right|\right) \qquad \text{Equation III-7}$$

In reality, calculation of the mean orientation should consider the symmetry of the f.c.c crystal which contains 24 symmetry operations for describing an orientation and there is equivalence between q and $-q$, too. For this reason, an iterative method was used to calculate the q_{mean}: a reference orientation, for example q_1 is compared to orientation q_2, chosen in a way that disorientation between q_1 and q_2 to be minimum. The mean orientation obtained, q_{mean}: is than compared to q_3 and …. In the same way this procedure is applied to all orientations to calculate the final mean orientation. This procedure is integrated in Orilib software, a C++ code developed by Quey [84].

Figure III-21 calculation of the mean orientation, for a series of orientations (Quey, 2008)

III.3.3.3 Schmid factor

It is observed experimentally that plastic slip occurs when the shear stress acting in the slip direction of the slip plane reaches a critical value (Schmid law). This critical shear stress is related to the stress required to move dislocations across the slip plane.

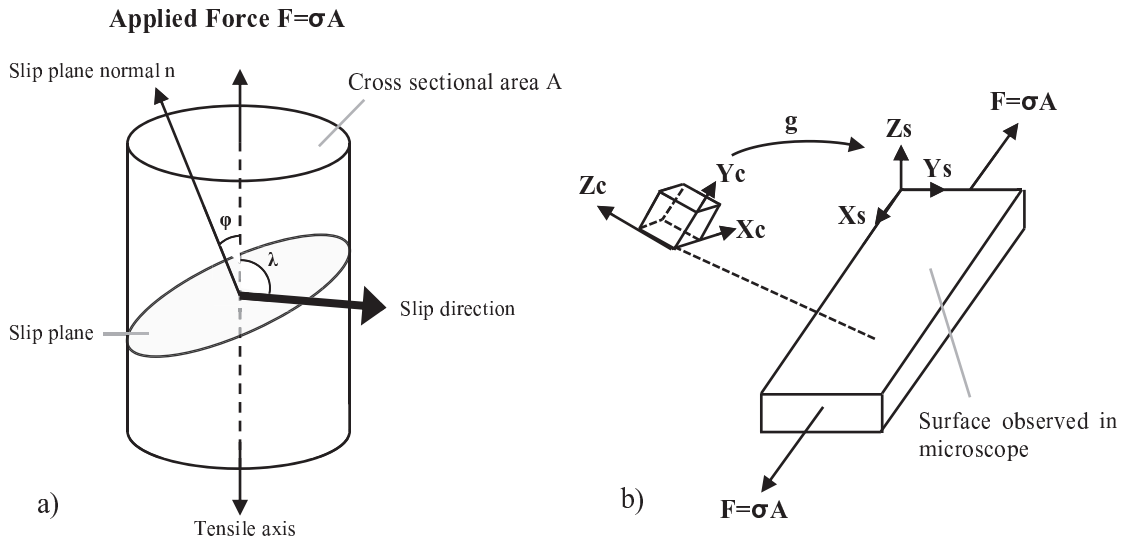

Figure III-22 relation between slip plane and slip direction with the applied tensile axis and (b) transformation from crystal coordinate to sample coordinate system

The resolved shear stress on the slip plane parallel to the slip direction is therefore given by:

$$\tau_R = \frac{resolved\ force\ acting\ on\ slip\ plane}{area\ of\ slip\ plane} = \frac{F\cos\lambda}{A/\cos\varphi} = \frac{F}{A}\cos\varphi\cos\lambda \qquad \text{Equation III-8}$$

where φ is the angle between the tensile axis and the slip plane and λ the angle between tensile axis and the slip direction. Before calculating these angles the crystal's slip direction and plane normal should be brought to the sample coordinate system. This can be done by using the orientation matrix calculated using the three Euler angles.

In f.c.c metals the observed surface traces result from dislocation movement in four {111} slip planes each with three possible <110> slip directions. Therefore, for copper 12 possible systems are considered.

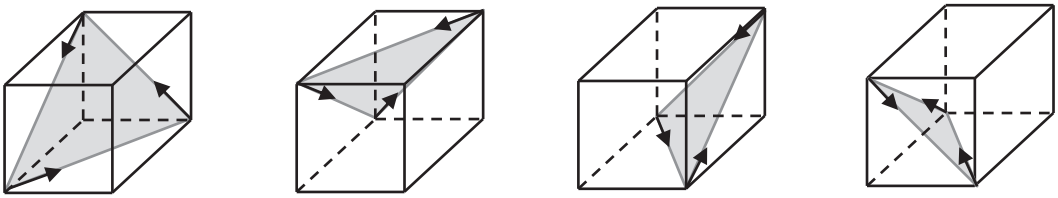

Figure III-23 The 12 slip systems in a f.c.c. crystal

In order to distinguish them better, they are named in the following order [87]:

A1	$(111)[\bar{1}10]$	A2	$(111)[0\bar{1}1]$	A3	$(111)[10\bar{1}]$
B1	$(11\bar{1})[\bar{1}0\bar{1}]$	B2	$(11\bar{1})[011]$	B3	$(11\bar{1})[1\bar{1}0]$
C1	$(1\bar{1}1)[110]$	C2	$(1\bar{1}1)[\bar{1}01]$	C3	$(1\bar{1}1)[0\bar{1}\bar{1}]$
D1	$(\bar{1}11)[101]$	D2	$(\bar{1}11)[01\bar{1}]$	D3	$(\bar{1}11)[\bar{1}\bar{1}0]$

Table III-2 The 12 slip systems in a f.c.c. crystal

The active slip system in the crystal is chosen to be the one with the maximum value of the Schmid factor.

III.3.4 Standard resolution EBSD measurements

For the objective of this thesis, a Zeiss Supra55Vp FE-SEM was used. In this SEM, the EBSP detector was attached to a port on the chamber, orthogonal to the stage tilt axis of the sample tilted toward the detector at ~70°. This port allowed the detector to observe samples placed at a working distance of about 15mm. As explained earlier the diffraction pattern is then captured by a CCD camera placed behind a phosphorous screen.

With a stationary beam at a point on the sample, an EBSP is analyzed using the HKL Channel5 software. The EBSP is uniquely defined by lattice parameters of the investigated crystal; by the crystal orientation in space; the wavelength of the incidence of electron beam (which is proportional to the acceleration voltage) and the proximity of the EBSP detector to the sample. With *a priori* information about candidate phases, the software determines and reports the identified phase and orientation. Then the software commands the SEM electron beam to move to the next point.

As the technique is developed for automated orientation detection and overall speed, the ability to scan the beam over multiple points on the sample has become practical. An EBSD map is then defined by its location, size and by the sampling step size between points. In this way, the resolution of the map may be adjusted to reveal the grain structure and grain boundary character, depending on the electron beam resolution under the sampling conditions, time available and size of the sample area required. In addition to beam control, for large sample area coverage, integrated stage motion is required.

The EBSD map of a sample after heat treatment is presented in Figure III-24 where the Euler angles $(\varphi_1, \phi, \varphi_2)$ correspond to the basic RGB colors. Knowing the orientation of each pixel and accounting for the crystal symmetry, the misorientation between each pixel and its neighbor is calculated (ex. By HKL Channel5 software) and the grain boundaries can be identified by imposing a limit value for the disorientation. In the example presented in Figure III-24 the grain boundaries with a misorientation of more than 10° are presented with black lines.

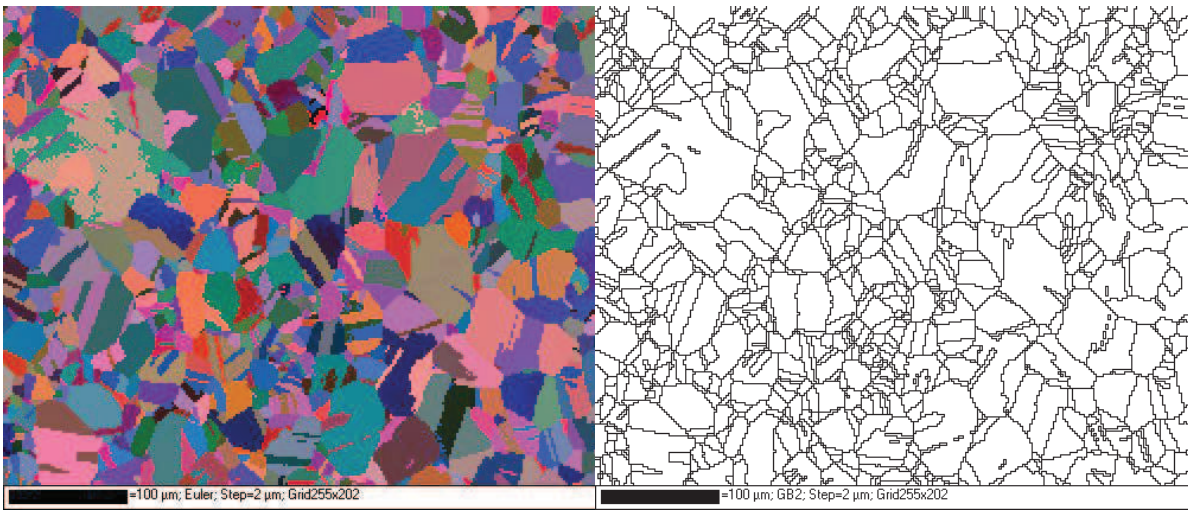

Figure III-24 EBSD map of the samples observed after heat treatment (left) Map of Euler angles presented in RGB mode (right) map of grain boundaries >10° calculated by HKL channel5 software

A number of parameters are used to describe the indexation quality and they are described as below:

Mean angular Deviation: A number that expresses how well the simulated EBSP overlays the actual EBSP. The mean angular deviation (MAD) is given in degrees specifying the averaged angular misfit between detected and simulated Kikuchi bands.

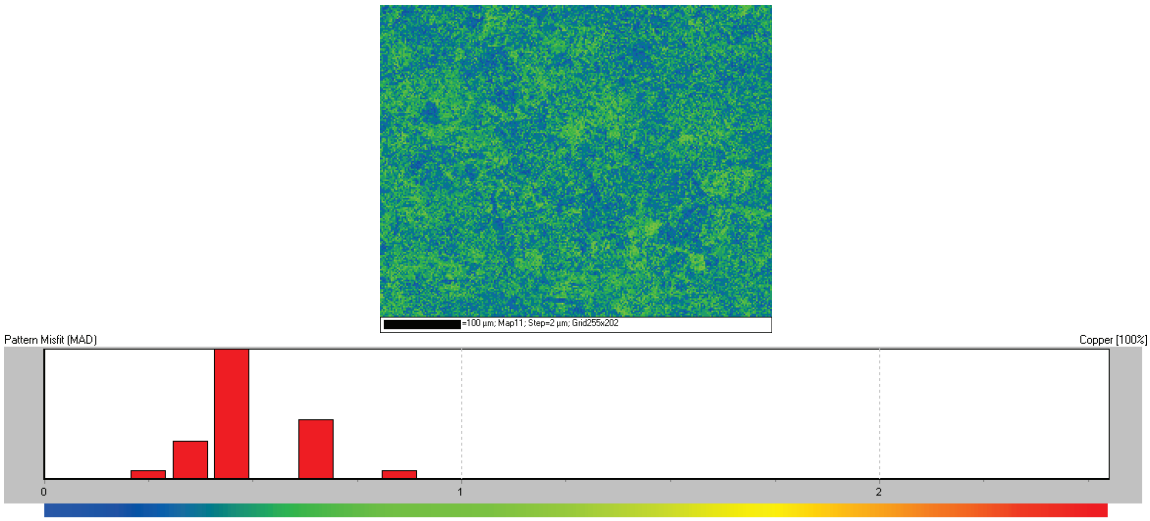

Figure III-25 Mean Angular Deviation (MAD) of the EBSD map presented in Figure III-24. As it can be observed in the legend's histogram; the misfit is below 1° for the entire map.

Band Contrast (BC): it is an EBSP quality factor derived from the Hough transform that describes the average intensity of the Kikuchi bands with respect to the overall intensity within the EBSP. The values are scaled to a byte range from 0 to 255. With this scale mapped to a grayscale from black to white, maps of BC can be created. These images indicate qualitatively different features of the microstructure, similarly to SEM or light microscopy images. Because EBSPs along grain boundaries have poor BC they appear dark in the map. Conversely, EBSPs of undeformed regions of a grain appear in light.

Band Slope (BS): it is an image quality factor derived from the Hough transform that describes the maximum intensity gradient at the margins of the Kikuchi bands in the EBSP. The values are scaled to a byte range from 0 to 255, i.e., the higher the value, the sharper the band.

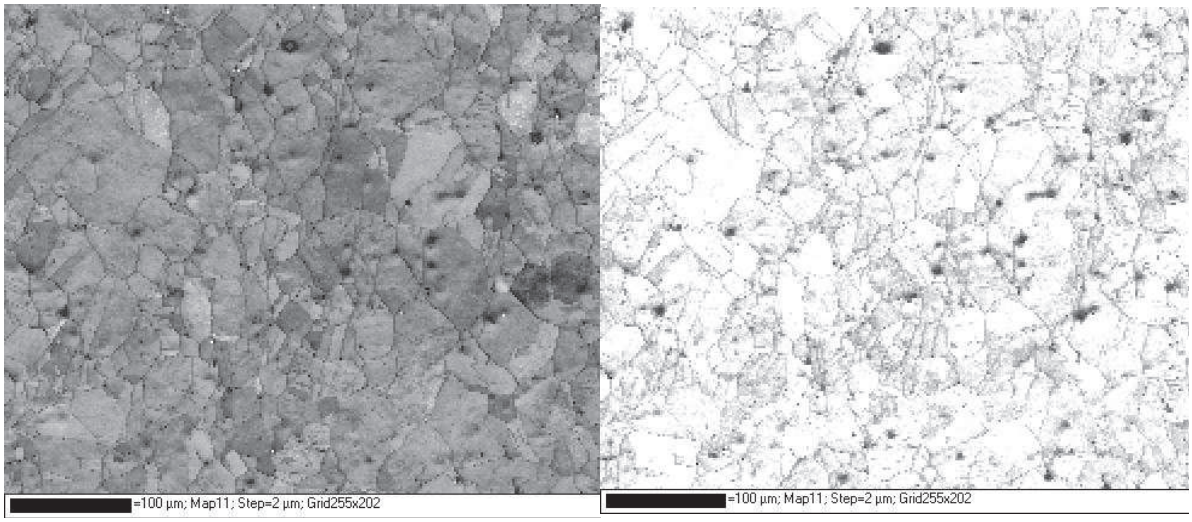

Figure III-26 Indexing quality presented by (left) Band contrast and (right) Band slope images

IV Non-destructive damage quantification

IV.1 Introduction

Fracture of metals and alloys during creep at elevated temperatures occurs generally by nucleation, growth and coalescence of grain boundary voids. Since the nucleation process is taking place at the nanometer scale or below, present characterization techniques allow a much better description of void growth and coalescence. Our present experimental knowledge on cavity growth is summarized in creep damage mechanism maps [6] similarly to the well-known deformation mechanism maps [75]. Some of these mechanisms were presented in section II.1.3. As a function of deformation conditions there are three basic mechanisms of cavity growth: at low strain rates and stresses the diffusive mechanism dominates, while at high rates and stresses growth becomes controlled by plastic creep flow. At intermediate values a coupling between diffusive growth and plastic creep is expected, but the mechanism has never been observed experimentally in spite of several attempts by Wang et al. [88]. This chapter focuses on the plastic creep mechanism characteristic for deformation conditions imposed in the experiment.

For the same samples discussed later in this section Dzieciol et al. [29] have shown that the growth mechanism of cavities during power law creep has a viscous flow nature and was identified with the glide and climb mechanisms of dislocations. Considering the viscous material flow for creep, Cocks and Ashby [24] have developed a general continuum model, which predicts the time evolution of the area fraction of the voids prevailing on sample cross sections lying perpendicular to the externally applied stress. The model emphasizes that damage evolution is deterministic, in the sense that material sections with initially higher amount of damage have higher damage rates. The aim of the present chapter is to study the local evolution of the area fraction of damage and to compare it with predictions of the existing model [24]. We also aim to expand the scale of damage evaluation at the sample level to and analyze damage localization and rupture.

IV.2 Experimental details

Experimental investigation of damage evolution is a challenging task since as mentioned above the damage rate depends on the amount of damage present in the material. This makes difficult a comparison between results obtained on different specimens by destructive techniques such as optical or electron microscopy. Moreover, damage assessment at the surface of the material can be quite different from damage in the bulk, for which reason application of non-destructive investigation methods capable of capturing these changes are desirable. Among several methods able to monitor damage we mention Acoustic Emission (AE), which is a standard qualitative technique [89] as well as synchrotron X-ray microtomography, which can be performed in situ during a creep test.

Three samples made of oxygen free high conductivity copper (OFHC) were creep deformed under the conditions described in Table IV-1. The corresponding creep curves are presented in Figure IV-1.

$T\ (K)$	$\sigma\ (MPa)$	$\dot{\varepsilon}\ \ (10^{6}s^{-1})$	Time to rupture (H)
573 ± 4	89 ± 1	6.0 ± 0.2	4.5
723 ± 4	37 ± 1	3.2 ± 0.2	6.8
773 ± 4	26 ± 1	2.6 ± 0.2	11

Table IV-1 Creep conditions of the three in situ deformed samples

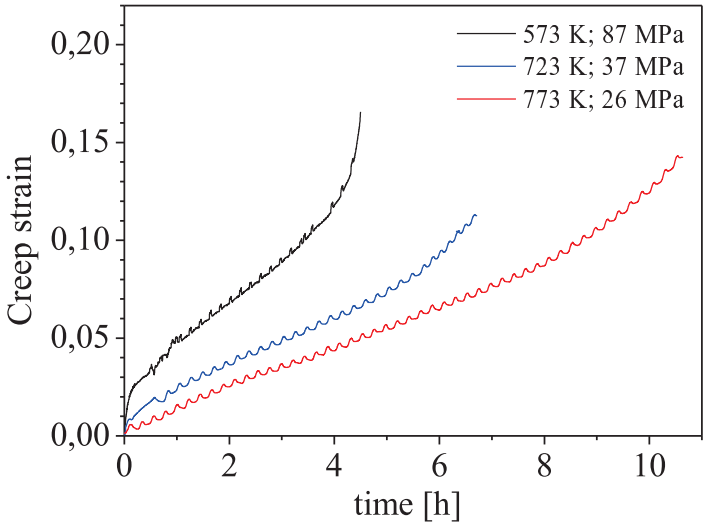

Figure IV-1 Creep curves of samples obtained on the miniaturized creep machine, the picks on each curve correspond to one tomographic acquisition

Microtomography during creep was in situ performed at ID 15A of the ESRF using an intense and parallel synchrotron beam generated by an undulator source. The mean energy of the beam was of about 80 keV and had a large band-width. The transmitted intensity was recorded using an X-ray detector with an effective pixel size of 1.4 × 1.4 μm^2. The CCD of the detector with a resolution of about 2.1 µm [90] was working in frame transfer mode. The readout speed of 60 frames per second of the CCD allowed operation without mechanical shutter. Motorized slits defined the horizontal and vertical beam sizes of 1.7 mm and 1.3 mm, respectively. 800 radiographs with an exposure time of 250 ms each were collected in about 3 min and scans were performed every 15 min. Volumes for investigations were chosen in such way that deformation is small enough to allow to correlate the slices between consecutive stages of creep.

IV.3 Data treatment

The procedure of data treatment consists of the following steps:

- Reconstruction of projections
- Image segmentation
- Correlating the reconstructed volumes

3D tomographic scans were reconstructed using in-house developed software based on the filtered back projection algorithm and accounting for the specific noise present in the measurement. Principles of this method are described in section III.2.1.2.

Since tomographic reconstructions usually have non-uniform brightness and the average gray-level of cavities depends on their size, a local method of segmentation was selected. It is also known that proper shape evaluation can be obtained only through gradient based and region-growing algorithms, which suggests a combination of local threshold followed by the watershed transformation.

Since reconstructed images contained also air beside the sample's microstructure, first the air had to be extracted. This was done by simple morphological operations, a coarse thresholding

followed by morphological dilation and erosion. Then small features were disconnected by morphological opening and finally closing with a given structuring element size was applied to provide a smooth outline. The images were segmented with the watershed algorithm using markers originating from a local threshold criterion [91]. The result of this is shown in Figure IV-2.

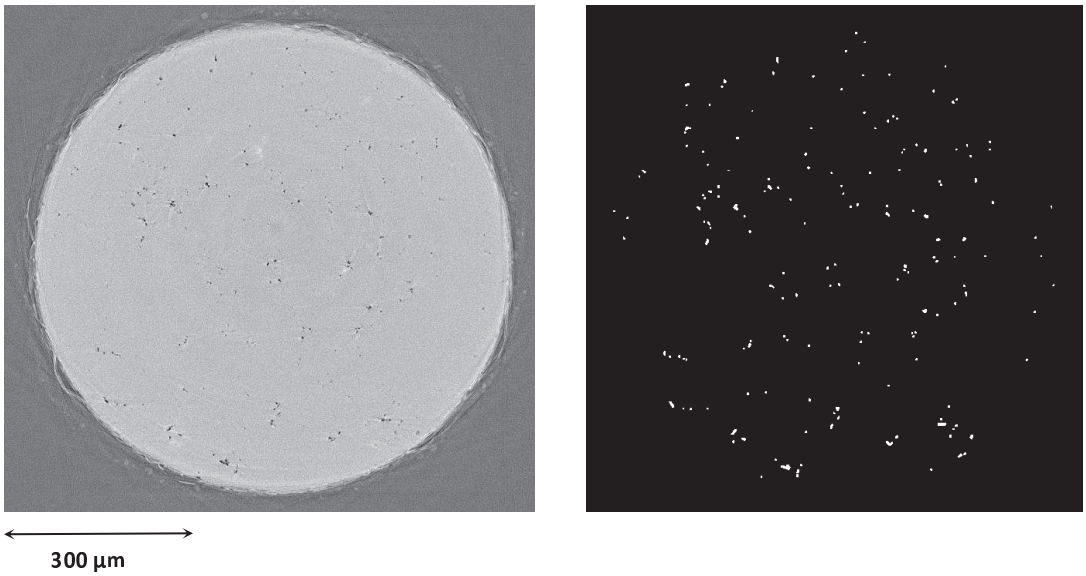

Figure IV-2 (left) The reconstructed section of a creep deformed sample which contains external air, the matrix and the creep voids. (right) The creep voids of the same image extracted using a local thresholidng and watershed technique

IV.3.1 Correlating the reconstructed volumes

Applying the segmentation procedure, the internal features (voids) were extracted from the matrix. The pores can then be reconstructed in three-dimensions for each volume. But these volumes still need to be correlated to register the objects in consecutive volumes.

IV.3.1.1 Phase correlation

The Phase-Correlation (PC) approach is based on the Fourier-shift theorem stating that the translation of a given function in the space domain corresponds to a phase shift in the frequency domain. Let $f_1(x,y)$ and $f_2(x,y)$ describe the grey levels of pixels in images 1 and 2, respectively. Further assume that image 2 is shifted with regard to image 1 by the vector (x_0, y_0).

$$f_2(x,y) = f_1(x - x_0, y - y_0) \qquad \text{Equation IV-1}$$

According to the translation property of the Fourier transform we can write:

$$\hat{f}_2(u,v) = \hat{f}_1(u,v)exp[-i(ux_0 + vy_0)] \qquad \text{Equation IV-2}$$

where $\hat{f}_m(u,v)$ denote the Fourier transform of $f_m(x,y)$, m=1,2. Hence the normalized cross power spectrum of the two images is given by:

$$\frac{\hat{f}_2(u,v)\hat{f}_1(u,v)^*}{\left|\hat{f}_2(u,v)\hat{f}_1(u,v)^*\right|} = exp[-i(ux_0 + vy_0)] \qquad \text{Equation IV-3}$$

where (*) indicates the complex conjugate. Taking the inverse Fourier transform (IFT) of the normalized cross power spectrum we obtain the Dirac delta function $\delta(x - x_0, y - y_0)$ centered at (x_0, y_0). Figure IV-3 illustrates the result of this operation on two cross-correlated images. A sharp maximum is obtained. It means that the inverse Fourier-Transform of the cross-power

spectrum yields a peak (Dirac delta function) at the position corresponding to shift between signals. The phase-correlation method can be extended to rotation and scaling detection too [92]. For this it is necessary to map the image in polar (for rotation detection) or log-polar coordinate systems (for both rotation and proportional scaling detection).

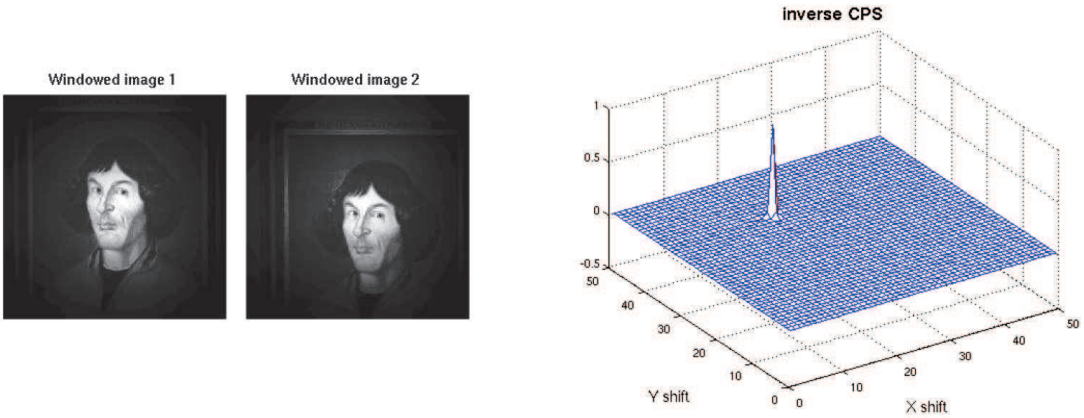

Figure IV-3 The shift between the two images is indicated by sharp peak in the inverse cross power spectrum (CPS) (Krzysztof Dzieciol, 2010)

IV.3.1.2 Global (slice) correlation

In order to extract the same objects from consecutive volumes, first, slices lying perpendicular to the external stress axis should be cross-correlated. The region of interest was shifted among the correlating slices and compared with the reference slice. Then the translation corresponding to the biggest correlation factor was taken as a result. This delivers the displacement of given cross sections at different stages of creep. The procedure is shown schematically in Figure IV-4.

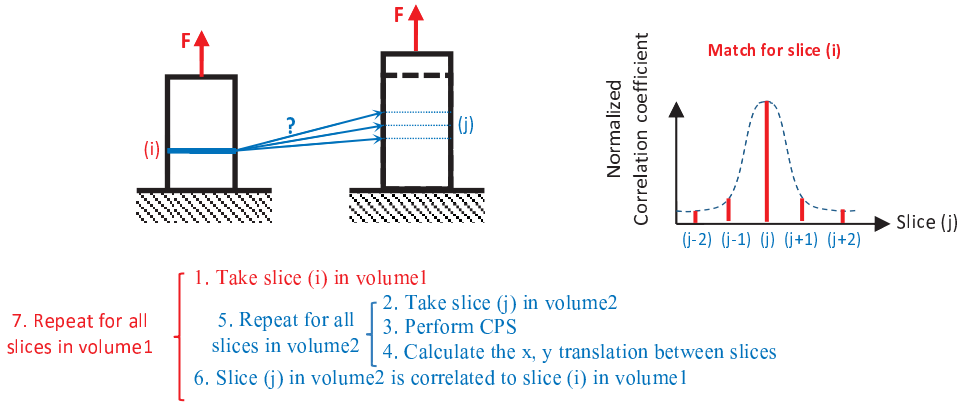

Figure IV-4 Procedure of slice correlation using phase correlation (PC) algorithm

Several correlation techniques were compared by Dzieciol [79] and it was found that the best performance is given by phase correlation. The higher coefficient and its low time consumption make it a good choice for processing big datasets. Advantages of PC are the possible detection of "sub-pixel" changes, short computational time and small sensitivity to gray level variations. This was important for volumes obtained from fast tomography, where contrast changes along the volume were visible due to the intensity inhomogeneity in the primary beam. Figure IV-5 shows, for example, voids evolution in a region of interest containing the most damaged slice (in the last reconstructed state) corresponding to the sample deformed at 773 K.

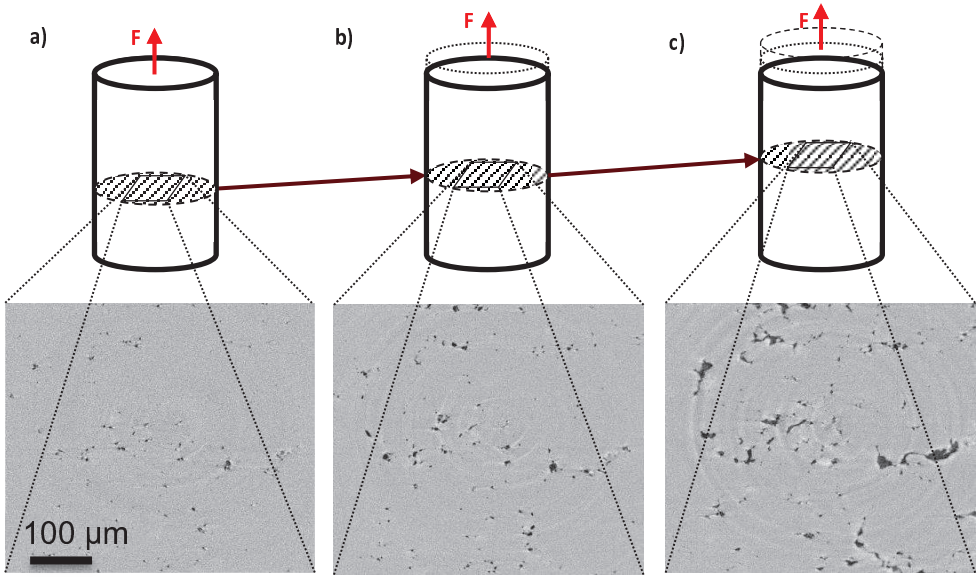

Figure IV-5 Damage evolution on slide no.56 (Figure IV-6) having the highest void area fraction in the last reconstructed state of the sample deformed at 773K. (a) t=0.36tf, (b) t=0.53tf, (c) t=0.79tf. The creep time is indicated as part of the failure time.

IV.4 Results

IV.4.1 Global (slice) registration

Damage was characterized by the area fraction of voids A_A, on slices lying perpendicular to the external stress. The evolution of A_A on each material slice has been followed through image registration by cross correlating slices of consecutively reconstructed volumes.

The area fraction of cavities for all registered material slices is shown in Figure IV-6 as a function of the slice number in the initial state and at different reduced creep times (creep time as multiple of creep lifetime). The figure indicates well damage localization by the gradually increasing local amplitudes. We should emphasize that remarkable fluctuations are present already at the beginning of secondary creep regime (0.36 t_f).

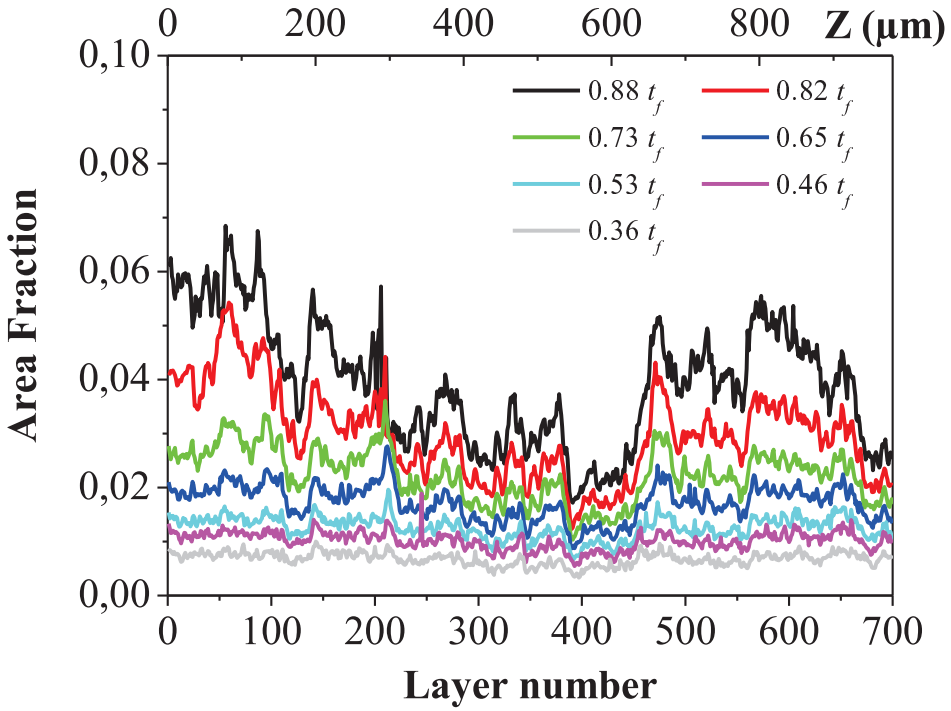

Figure IV-6 Evolution of the area fraction of cavities on material slices lying perpendicular to the external load at different creep times. The slice numbers corresponds to the initial state. The upper horizontal scale gives the position of the slices in µm (sample deformed at 773K)

IV.4.2 Local strain rate

The results of slice registration can be used for the evaluation of the local strain and strain rate in the sample, too. Selecting an initial reference distance along the Z axis of $l_0 = 50\ layers\ (70\mu m)$, the results of slice correlation will also provide the length l between selected reference slices. The local true strain is simply obtained as described in Equation IV-4.

$$\varepsilon_{loc} = \ln\frac{l}{l_0} \qquad \text{Equation IV-4}$$

The strain rate is obtained in a second step by dividing the strain with the time interval between cross-correlated reconstructions, typically of 30 min. Figure IV-7 shows the distribution of the local strain rate (left axis) along the gauge length of the sample deformed at 773 K at two characteristic points of the creep curve: a) at the middle of secondary state and b) at the beginning of tertiary state. The strain rate at $0.53t_f$ decreases slightly (by about 20%) from layer 100 to layer 700. This decrease is larger than the error of the strain rate estimated from cross-correlation analysis to be of about 5%. A possible reason for this can be the small temperature gradient pointing towards the bottom of the ample. At the beginning of the tertiary creep stage, however, the strain rate shows a quite different behavior with higher values near the extremities of the gauge length. This is in good agreement with the variation of the average area fraction of voids (Figure IV-7 right axis). The comparison emphasizes the influence of local damage and local strain rate.

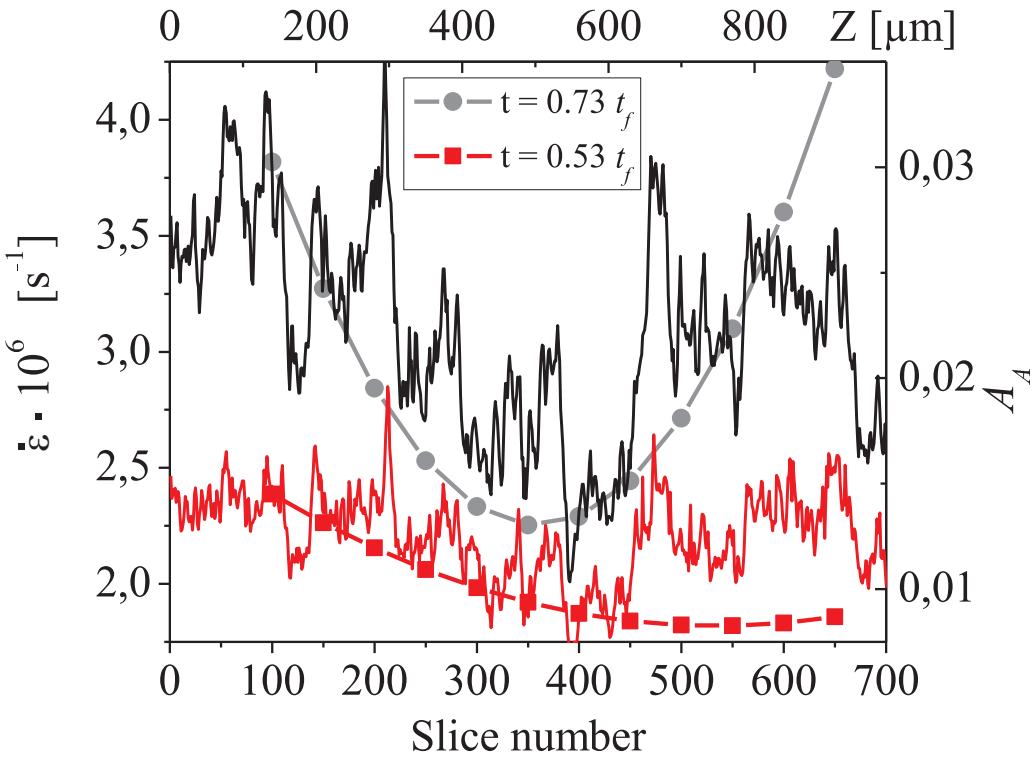

Figure IV-7 Local strain rate along the gauge length at two deformation states ($t=0.53t_f$ and $t=0.73t_f$) and the corresponding distribution of A_A (continuous line) for the sample deformed at 773 K

IV.4.3 Damage localization

To describe damage localization the evolution of porosity on the material slice having the largest area fraction A_{Amax}, (in the last reconstructed state) was selected. In order to compare the samples creep deformed under different conditions, the average value of $\bar{A}_A$ (global porosity) was chosen as an independent variable. Figure IV-8 shows that the evolution of A_{Amax} is very similar for the three samples not depending on temperature, strain rate or stress. This emphasizes that the damage mechanism (growth and coalescence of voids by viscous flow) is the same in each case. The largest area fraction of voids for the sample deformed at the lowest temperature 573 K and highest stress 87 MPa is relatively small (~0.0075) since the last analyzed state is still in the secondary creep regime. The reason for this is the relatively long acquisition time of a tomographic scan (~3 min) compared to the actual strain rate. During the acquisition time the movement of material layers due to sample elongation is larger than the pixel size, which leads to the blurring of the image. The last reconstructed state corresponds only to 75% of creep lifetime and it is still in the secondary stage (see Figure IV-11). For the case of samples deformed at 723 K and 773 K the last reconstructed state is in the tertiary stage at 88% and 90% of the lifetime, respectively.

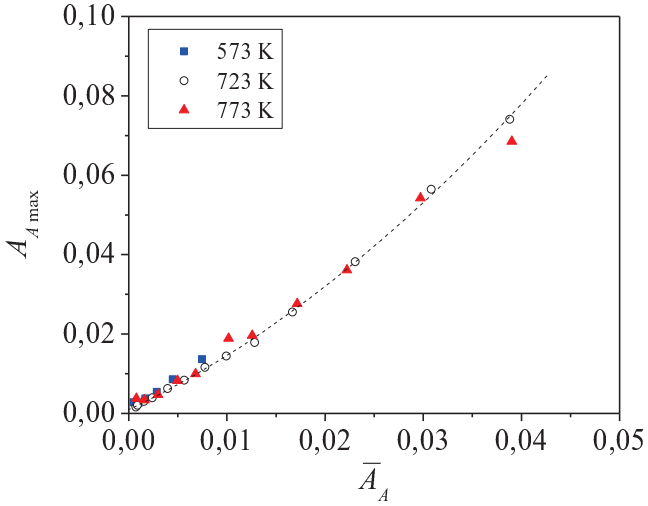

Figure IV-8 Evolution of the largest fluctuation A_{Amax} as a function of the mean are fraction ($\bar{A}_A$ or volume fraction) of voids

It was suggested recently [89] that creep rupture time of composites is proportional to the duration of the primary creep regime. Such a rule is very interesting and it can offer a good method for rupture prediction. Exploring the phenomena from a microstructural point of view, this means that essential features of damage should be present in the microstructure already at the beginning of secondary creep regime. It is evident that the copper polycrystal shows less heterogeneity than fiber reinforced composites [89], but as shown previously (Figure IV-6) one cannot exclude that an initially present small heterogeneity of damage determines the final fracture and its location.

IV.4.4 Similarity to final stage

Considering the distribution of A_A in the final reconstructed state as representative for damage distribution before fracture we have quantified the similarity between this distribution and that at an earlier deformation state. The corresponding cross correlation coefficients CC, are shown in Figure IV-9(left) as a function of the average area fraction of cavities $\bar{A}_A$.

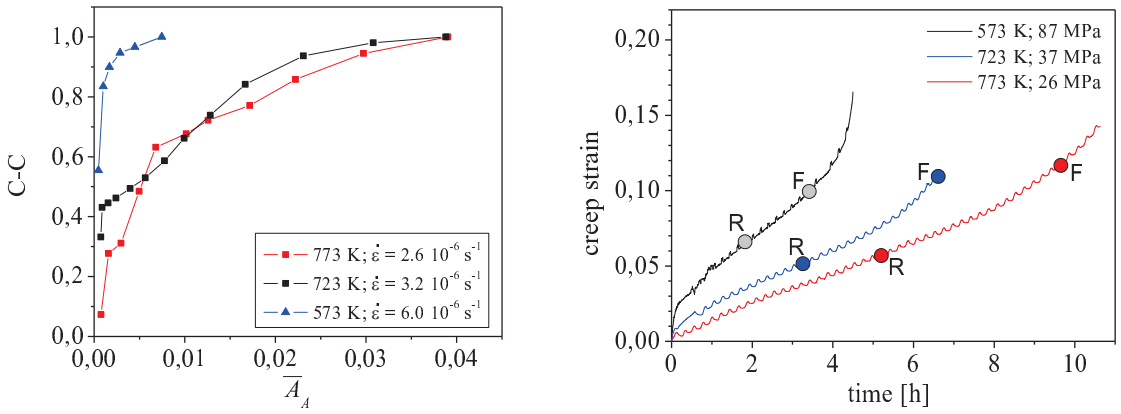

Figure IV-9 (left) Variation of the cross-correlation coefficient between the final and previous distributions of A_A as a function of the average area fraction of voids (right) corrected average creep curves showing final state (F) and the state (R), which has a strong correlation to the final state.

All samples show monotonically increasing cross-correlation coefficients indicating increasing similarity with the final state. It is remarkable the fast increase of the correlation coefficients corresponding to the sample deformed at the highest strain rate and lowest temperature (573 K). The two other samples (723 K and 773 K) having nearly identical strain rates show very similar variations, which means that the strain rate is an important parameter affecting localization.

Choosing a threshold value for the correlation coefficient it becomes possible identifying a previous deformation state, in which damage distribution already showed a strong similarity to that before rupture. For the usual "strong correlation" threshold of $CC_{th} = 0.7$, the corresponding "similar" states are indicated by circles in Figure IV-9(right) (the states before rupture are indicated by F). It is remarkable that for all samples the state with high similarity appears already in the secondary stage (half of the lifetime), when the corresponding creep strain is only about 5%. The creep curves in Figure IV-9(right) have been calculated from the measured displacement of samples top region using the inductive displacement transducer. Strain calculation has been done choosing the effective length $l_{eff} = 2.3\,mm$, which led to the same value of the average strain rate in the secondary stage as the one obtained from tomographic evaluations. The undulations on the curves originate from the inductive displacement transducer, the cables of which were moving during the tomographic scan.

IV.4.5 Simulation of damage distribution according to model of Cocks and Ashby

In [29] a comparison between the evolution of experimentally determined mean volume fraction of cavities and the prediction of the Cocks and Ashby model [24] was presented. Here we use the Cocks and Ashby model to predict the evolution of damage fluctuations (as recalled in Figure IV-10 and Equation IV-5 [24]).

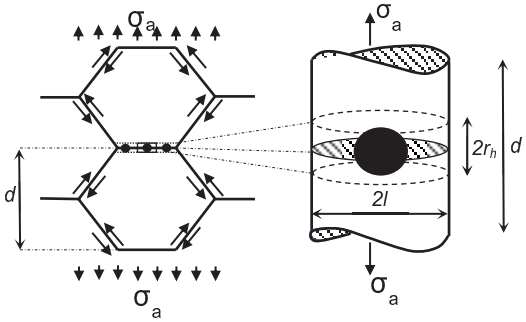

Equation IV-5

$$\frac{1}{(1-f_h)}\frac{df_h}{dt} = \frac{\dot{\varepsilon}_{ss}}{(1-n\dot{\varepsilon}_{ss}t)}\left\{\frac{1}{(1-f_h)^{n+1}} - 1\right\}$$

f_h:Area fraction of holes on grain boundary

$\dot{\varepsilon}_{ss}$: Steady state creep rate

Figure IV-10 A recall of the void growth model proposed by Cocks and Ashby [24]

Since the model has been developed for the case of non-interacting voids such a comparison would allow quantifying the importance of cavity interaction, which is expected to become more and more important at later stages of creep. Therefore the evolution of A_A on each material section was calculated according to the Cocks and Ashby model [24] starting from initial values corresponding to the "strongly similar" states identified by cross-correlation (section IV.4.4). The results show first of all that local damage evolution is faster in experiment than in simulation in agreement with previous findings for A_A [29].

To better emphasize the similarities between experimental and predicted distributions of A_A the calculations have been continued for a longer time until the model curve reached one point on the measured curves. As shown in Figure IV-11 the predicted damage distributions describe satisfactorily the measured experimental distribution. Exceptions are the regions with strong localization of A_A.

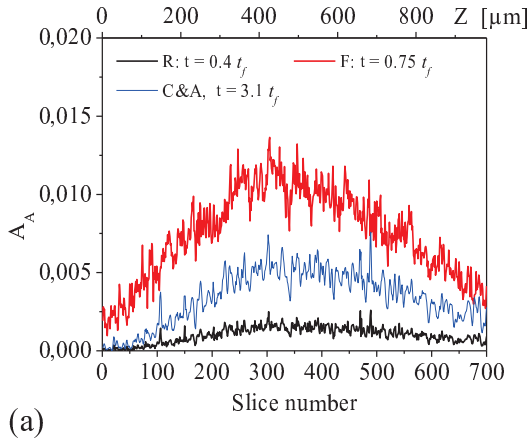

(a)

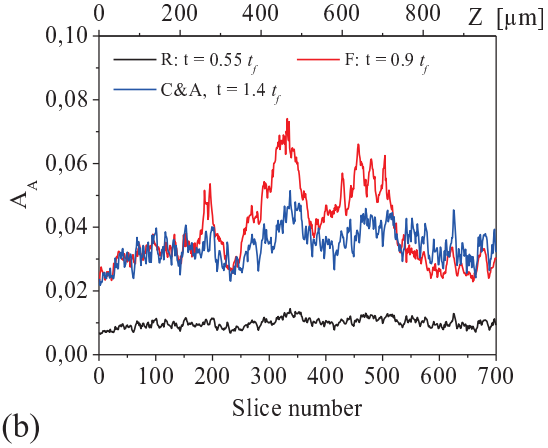

(b)

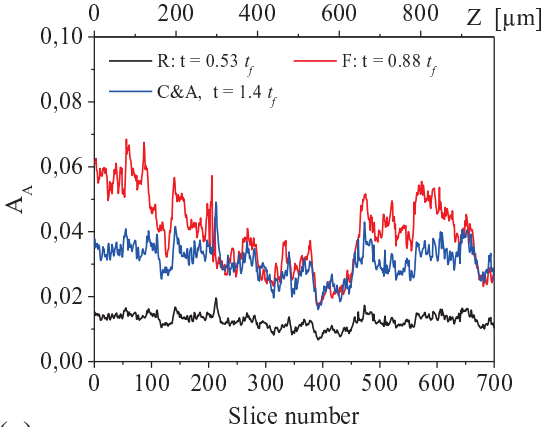

(c)

Figure IV-11 Comparison between experimentally determined and predicted distributions of void area fraction along the gauge length. The experimental distributions correspond to the final reconstructed state (F) and a previous reference state (R) with a cross-correlation coefficient larger than 0.7. The reference state has been used as an input for prediction of damage distribution according to the model of Cocks and Ashby [24] **(a) sample deformed at 573 K, (b) at 723 K and (c) at 773 K.**

IV.5 Discussion of in situ tomography results

There are a relatively small number of scientific publications dealing with the in situ analysis of damage localization during plastic deformation of engineering materials [29], [67], [89], [93], [94]. The existing tomographic data describe the different type of damage in complex composite structures during room temperature (RT) tensile deformation [95], [96] or creep at high temperature [94]. Tomographic reconstructions of these composites clearly evidence different damage mechanisms, such as particle delamination, particle fracture, void formation and growth at various stages of creep [94], [95]. These earlier works have mainly focused on describing damage evolution at the micro-scale in terms of the average void [62], [67], [68] or in terms of single cavities [29], [93]. Another parameter investigated was the mean volume fraction of voids or *global porosity*, which for RT deformation was found to increase much slower with deformation [96] than the prediction of the classical Rice and Tracey approach [64]. Good agreement has been found, however, between the predicted and experimentally determined *local porosity* for some sub-volumes of the structure [96]. This clearly indicates the importance of damage inhomogeneity and localization and at the same time the inadequacy of a "mean cavity" approach. Dzieciol et al. [29] have described this inhomogeneous distribution of damage in terms of the area fraction of voids on planes perpendicular to the applied stress, which is a reasonable choice if the cylindrical symmetry of the deformed sample is taken into account.

This section further expands the latter study by analyzing the evolution of damage fluctuations and trying to answer questions related to damage localization and final fracture.

Present results indicated that a strong coupling exists between the amount of local porosity and the local creep rate. It is interesting to note that variations of about 1% in the area fraction between different parts of the gauge length (Figure IV-7) lead to relatively large variation of the local strain rate, a self-amplifying process that is clearly evident in the tertiary creep stage. The origin of damage localization roots, however, is much deeper in the void growth mechanism. For viscous flow the volumetric void growth rate is proportional to void volume [28], which means that larger voids grow faster than smaller ones. Thanks to the sensitivity of the tomographic evaluation the growth of small fluctuations is already observable in the secondary stage of creep.

From the point of view of creep lifetime prediction the most interesting parameter seems to be the fluctuation having the maximum amplitude $A_{A\,max}$. How this amplitude is related to other structural parameters is a very intriguing question. Obtaining such a relationship could serve as a good predictor of creep lifetime once an analysis of the microstructure has been performed. We have found empirically a parabolic law describing the evolution of $A_{A\,max}$ as a function of the mean volume fraction $\bar{A}_A$. This law is described in Equation IV-6.

$$A_{A\,max} = a_0 + a_1(\bar{A}_A) + a_2(\bar{A}_A)^2 \qquad \text{Equation IV-6}$$

where $a_0 = 10^{-3} \pm 3.10^{-4}$, $a_1 = 1.18 \pm 0.06$ and $a_2 = 18.6 \pm 1.5$. As fluctuations depend on the size of the system Equation IV-6 should be considered valid only for copper specimens with dimensions similar to the ones investigated in present work. We are also aware that the global porosity is not the best independent parameter, but the independence of $A_{A\,max}$ from temperature and strain rate indicates that this approach might be adapted to practical cases with well-defined geometry and where creep lifetime prediction is an important issue. It is important to note the relatively small value of $A_{A\,max} \cong 8\%$ in the last reconstructed state ($t \cong 0.9t_f$). This is much smaller than the value of 25% usually considered as a failure criterion [24].

Cross-correlation results between the distribution of damage in the last reconstructed state and earlier states revealed a relatively new aspect of damage localization. The strong correlation ($CC > 0.7$) between the distributions at about 90% and 50% of creep lifetime is remarkable, which clearly indicates the deterministic nature of damage evolution. Compared to results originating from the macroscopic behavior of the creep curves and relating fracture time to the length of the primary creep regime [89], the present data show that damage distribution before rupture is strongly correlated to a state near the middle of the secondary stage. As indicated by the rate of AE energy release substantial damage in composites has already been formed at the end of primary creep, which might explain the discovered correlation with the creep lifetime [89]. Contrary to this, in the copper polycrystal damage evolves more progressively, dominant fluctuations developing only in the secondary stage.

The corresponding creep time is about half of the creep lifetime, but is also surprisingly small.

In line with previous findings simulations of damage distribution according to the model of Cocks and Ashby [24] have been performed. The calculations show that theoretical predictions and experimental data are in satisfactory agreement (Figure IV-11) suggesting that damage distribution at the half of the creep lifetime is already characteristic for that in the final state. The model does not adequately describe damage growth in regions of high localization. This faster growth in experiments might be attributed to void interaction effects not taken into account by the model. Evidently, the results for the sample deformed at lowest temperature having the last reconstructed state at 75% of the lifetime are less characteristic than those of the other two with final reconstructions at $0.88\ t_f$ and $0.90\ t_f$, respectively. Ideally, damage distribution in a state as near as possible to the moment of the final fracture is needed. This requires faster tomographic scans, which will probably be available with a new generation of CMOS based X-ray detectors.

IV.6 Conclusions

Creep damage evolution in terms of the area fraction of voids on slices perpendicular to the external stress has been investigated using in situ tomography. It was found that:

- Damage localization begins relatively early; distribution of A_A along the gauge length of the sample at the half of the creep lifetime shows already strong correlation with the distributions at $t = 0.90\ t_f$.
- The amplitude of the maximum fluctuations increases parabolically as a function of the average area fraction of voids. For power-law creep of copper this relationship is independent of temperature, stress or strain rate.

The next question to be answered here is that: Is there any influence of local crystallography on the damage mechanism? If yes, how can we evaluate that? The conventional tomography is not capable of providing any information about the crystallography. As also explained in section II.2.2 the methods like 3DXRD, DCT or HEDM are applicable on the samples at the initial state. So they are not ideal for creep deformed samples containing pores. Destructive methods like FIB-EBSD, TEM, KESM or ultramicrotomy are able to provide the desired information, but they are all local observation methods and it is hard to obtain statistically representative results from them. Hence it is important the application of an investigation method adapted to present needs. Wide-field EBSD combined with serial sectioning was therefore developed within the frame of this thesis at Ecole des Mines de Saint Etienne. The method and the results obtained are presented in the following chapters.

V Destructive damage quantification

V.1 Introduction

The main aim of this chapter is to extract the crystallographic information of the grains located in the neighborhood of creep pores. Analyzing the crystallographic data, we can define the grains and extract the grain boundary positions. To achieve this objective a new technique is developed based on serial sectioning combined with EBSD. In chapter IV, it was concluded that a statistically based relationship between damage and local crystallography is needed. This is possible only by choosing a big enough analyzed volume, which is representative for the sample. Based on the bibliographic review presented in chapter II the experimental method permitting to do this is on plastically deformed specimens is the serial sectioning. As will be explained further in this chapter some modifications to the conventional serial sectioning technique will be necessary, which will insure that by using the EBSD in wide-field mode, enough data is extracted to reveal a statistical relationship between damage and crystallography.

V.1.1 Conventional serial sectioning

The basic steps of the conventional serial sectioning process are as follows (Figure V-1): Polishing, estimating the removed layer's thickness and surface characterization.

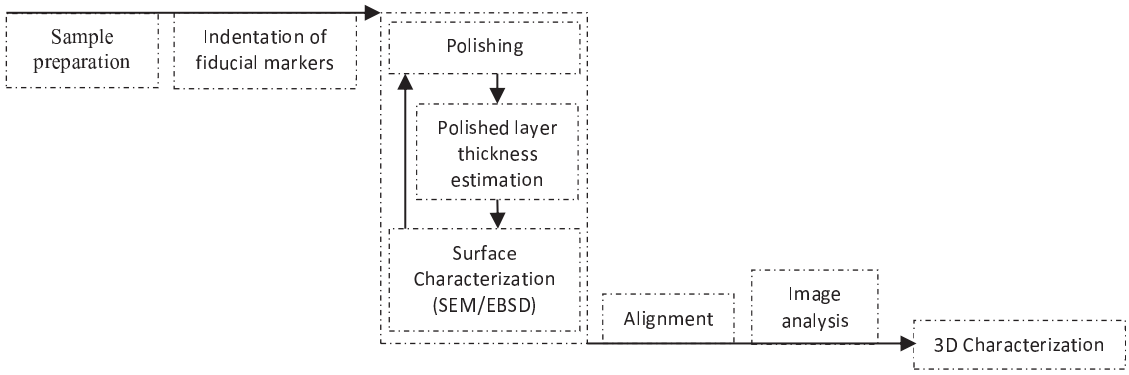

Figure V-1 Conventional serial sectioning - The basic steps

The primary polishing step is usually performed using abrasive papers, diamond solution [97] or SiC/AL_2O_3 particles [52]. The material removal is supposed to be homogenous over the required section (as much removal from a soft matrix as of the hard particles in a given microstructure). The obtained surface is also hypothetically considered to be parallel to the initial surface.

The second step consists of the estimation of the removed layer's thickness. At some scales of removed thickness, the sample's thickness can be measured directly [97] or by metrological instruments [98]. But for higher resolutions the initial surface is subjected to one or several micro hardness indentations. The height of the indent depends on its geometry (Figure V-2 - when not damaged or worn out). In case of using the Vickers indentation, the indenter is a diamond in the form of a square-based pyramid and its height can be obtained according to Equation V-1. Then the layer's thickness is calculated as the difference in the height of the indents calculated before and after polishing.

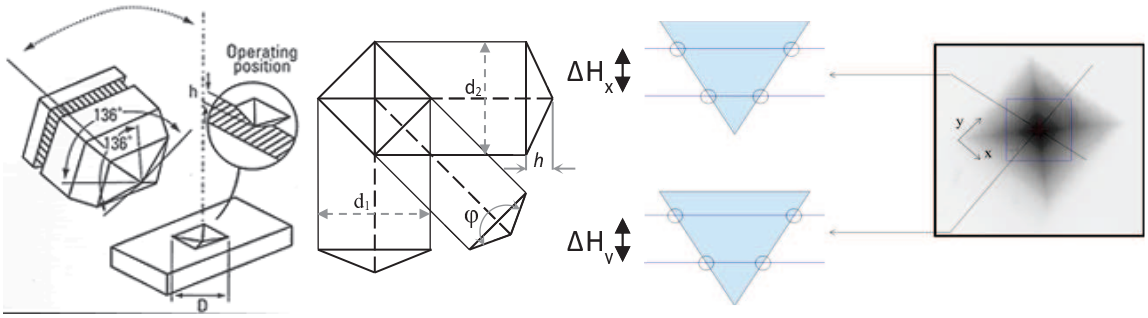

Figure V-2 Micro hardness indentation geometry

$$h = \frac{(d_1 + d_2)/2}{2\sqrt{2}\tan\left(\frac{\varphi}{2}\right)} \qquad \text{Equation V-1}$$

Finally, the polished surface can be imaged by optical/electron microscopy. Repeating this procedure a stack of images is obtained. Even if during the imaging procedure, the sample is placed in the same way in the microscope stage, the different images of the stack have translation and/or rotation with regard to each other. Superposition of the images in the stack is usually done manually or by image correlation techniques.

V.1.2 The problems of conventional sectioning methods

The accuracy of the conventional sectioning techniques is a subject which sometimes gets lost in various hypotheses that cannot be easily checked. Even if the effort is made to apply a homogenous charge on the sample while polishing, the resulting sections are not always parallel to the initial section as shown schematically in Figure V-3. This is especially true in case when large areas are polished and requires the real measurement of the locally removed layer thickness.

Figure V-3 Parallel sections hypothesis (a), becomes wrong when the load distribution is not homogenous over the polished section and lead to non-parallel sections (b)

The measurement of the thickness of the removed material is influenced by several factors:

- If the indentation diamond is damaged, or simply gets worn out while penetrating the surface, the intersection angle φ changes. So, the result of Equation V-1 with $\varphi = 136°$ becomes false. The calibration procedure can improve the accuracy but cannot guarantee the quality of indentation.
- In order to perform a perfect indentation, the sample's surface should be perfectly perpendicular to the indent diamond. Also reading the diagonals $d1$ and $d2$ require them to lay in the observation plane of the microscope.
- The penetration depth of the indents depends on the local crystallography of the grain, situated below the indent. This is due to the plastic anisotropy of the mechanical properties linked to the grain's orientation. For the same reason, mechanical polishing rate of the grains depends on their orientation. So, averaging the indentation height on several (usually 4) indents cannot accurately describe the global material removal.

The problem of the measurement of the indent diagonals was treated differently by several authors. Sidhu and Chawla [33] were the first to treat this problem. If the indentations were difficult to measure due to the ambiguity of exactly where an indentation diagonal began and ended, they have suggested that a reasoned guess can be made based on the previous measurements and what parts of the indentation can be identified as the vertices. Zhao et al. [99] proposed a process on how to define the shape of the indents correctly by using an image processing technique. Their technique used Level-Set and Geodesic Active Contours to obtain the contour and the diagonals of the indents and then the depth of the material layer removed is obtained using the diagonals depth on two consecutive sections. Any measurement error for each layer leads to an accumulation of the errors in serial sectioning. Therefore, our objective is to improve the conventional technique by suggesting a new high resolution and wide-field reconstruction method, which incorporates an optical profiling system. In addition to the proposed measuring procedure, the entire sectioning procedure is reviewed.

V.2 Experimental procedure

In this section, the experimental procedure of serial sectioning is explained step by step. Creep samples, deformed in the creep machine presented in section III.1.3 are chosen to be analyzed.

V.2.1 Sample preparation for serial sectioning

The procedure of serial sectioning is long. So, it is better to apply it simultaneously on several samples in an automatic or semi-automatic mode. Since samples with equivalent initial geometry are deformed to different strains, their actual size is different from each other and applying the same polishing load leads to different polishing rates. Therefore, the samples should be embedded in a polymer resin before. This helps the polishing procedure, which is now applied on the same surface area of all the samples. Embedding in a resin helps additionally the manipulation of fragile samples. Polishing the samples homogeneously several times and in the same way, excludes any type of sample holders which require the sample to be glued or screwed to the sample holder. The samples should be free to float in the vertical direction, but they should be blocked to translate horizontally. The idea is to use a polymer mask with several emplacements machined in it. Then the samples, which are protected by the epoxy resin can be machined with high precision with the same dimensions of the mask with a gap of about 10 µm (Figure V-4).

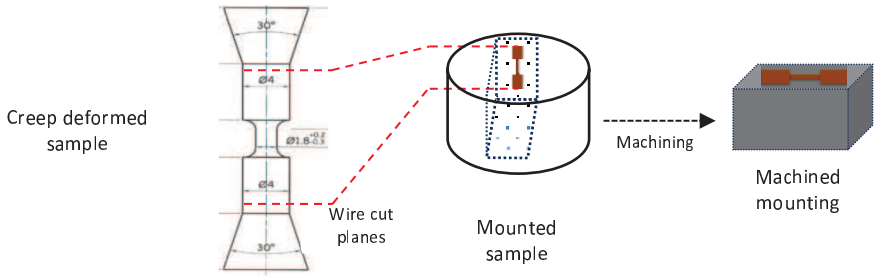

Figure V-4 Sample preparation for serial sectioning

The mask is then placed directly on the polishing cloth of the machine; the samples are numbered and one of their sides is labeled with “N” which will be always inserted in the same way in the mask. A thin rubber layer is then added on the mask, which will be the connection between the applied load and the mask. All the assembly is then protected by an outline piece called the contour made of a polymer, as shown schematically in Figure V-5.

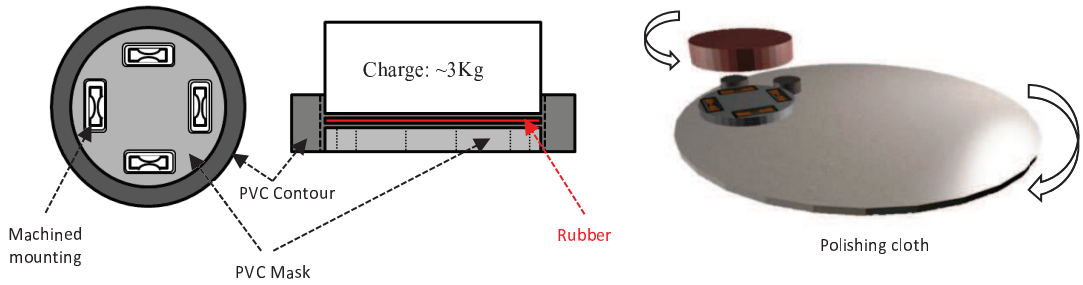

Figure V-5 Schematic drawing of the assembly used for serial polishing

V.2.1.1 The observation zone

Our aim was the development of a sectioning method that permits the analysis of a relatively large surface. The gauge length of the samples to analyze is about 2 mm long with a diameter of 1.8 mm. Taking into account the cylindrical geometry of the sample, the length of the analysis surface is chosen to be 1.2 mm along the cylinder axis and 0.8 mm perpendicular to it. This gives a final surface of 1.2 x 0.8 mm^2. This observation zone was marked by microhardness indents.

As it will be further explained the average size of the grains is estimated to be 40 µm (using EBSD analysis). Obviously it is not possible using a 40 µm deep indent because this will be quite large at the detriment of the analyzed surface. Table V-1 presents the indent size on our copper samples as a function of the applied load. The bigger the indent depth the less indents are needed for the reconstruction. We have selected the indent with a penetration depth of 13 µm and a diagonal size of 90 µm that corresponds to a charge of 500 g.

Indentation charge (g)	Diagonal size (µm)	Depth (µm)
200	56	7
300	70	10
500	90	13
1000	130	18

Table V-1 Indent size, obtained on OFHC cupper, profiles analyzed by optical interferometer

V.2.2 Material removal

The material removal procedure has to meet several conditions:

- First of all, the polished surface should be prepared for SEL and EBSD observations and should be free of any deformation induced by polishing procedure (so that the EBSD patterns can be obtained on it).
- It is also important that the pores should remain free of artifacts, and
- For the objectives of comparing the results of serial sectioning with those of tomography a vertical resolution of 1 µm is desired. Therefore, the thickness of the removed material should be around this value.

All the three major methods of polishing proposed in section III.2.2.2 will be reexamined and discussed in the following sub-sections.

V.2.2.1 Electorchemical etching

Electrochemically polishing is a very fast method that provides good finished surfaces, but can introduce artifacts at grain boundaries and especially at voids, where chemical etching becomes accelerated. So, this method cannot be accepted as material removal procedure.

V.2.2.2 Broad ion beam etching

Material removal by ion beam etching was examined using a GATAN model 682 PECS ion beam etching and coating system. The following results were obtained:

- The cone shaped ion beam causes some artifacts. Ions at the center of the beam have more energy than near the side and lead to in-homogenous polishing. This effect accentuates with increasing the number of polished layers.
- Selective etching: Grains are sputtered at different velocities, according to their geometric orientation to the ion beam direction [55].
- If the initial surface contains some defects, a cone or pyramid in the structure can be caused (Figure V-6-left).
- Re-deposition of sputtered material causes also some artifacts (Figure V-6-right).

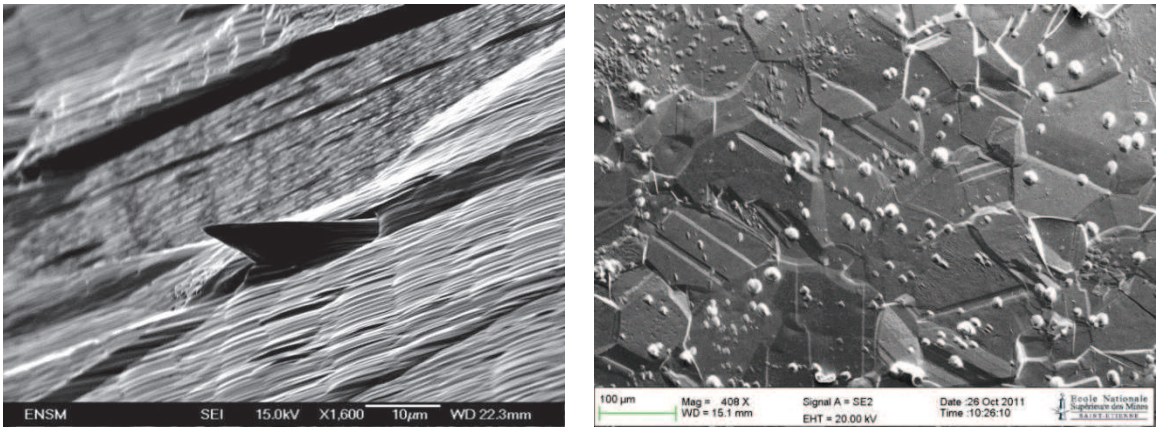

Figure V-6 Artifacts caused by Ion beam etching (left) cone formed as a result of initial surface defect (right) re-deposition of sputtered material

V.2.2.3 Chemical Mechanical Planarization (CMP)

CMP is a process that is now routinely used to planarize metals. This procedure is specially applied in the fabrication of integrated circuits [100]. This process uses slurries of fine abrasive particles such as colloidal silica. The stability and performance of slurries are influenced by the size and properties of these particles, which in turn are influenced by their synthesis route. Stability is important to improve slurry lifetime and minimize defects such as micro scratching caused by particle agglomerates or large particles during polishing. The rheological behavior of the slurry affects the friction at the polishing cloth-particle-sample interface and can alter the material removal rate. It is, thus necessary to carefully engineer the slurry characteristics to achieve good removal rate and planarity without causing defects. The slurry used for this research is the STRUERS OP-S suspension which has a PH of 9.8 and a grain size of about 0.04 µm. OP-S can also be used with the addition of reagents. This increases the chemical activity, thus shortening the actual polishing time. Slurries for copper CMP should contain smaller amount of abrasives (~3% by weight) and are maintained at slightly acidic PH (4-6) values. This can be obtained by adding an acidic agent like acetic acid or oxalic acid. This slurry can contain an oxidant such as hydrogen peroxide and a copper complexant to enhance the chemical component of CMP. The removal rates of copper with these slurries can change from 50 to 600 nm/min by controlling oxidizer, complexant and inhibitor concentrations [100]. For this project we did not use additive chemical components, so the samples were polished by OP-S at the initial PH of 9.8. Therefore the polishing rates were relatively small. The CMP was performed on a LAMPLAN Mastertex polishing cloth, perfectly adapted for being used when using colloidal silica particles.

As it was explained, the mechanical aspect should be coupled with the chemical aspect to get a controlled material removing rate. So, the charge on the sample and the rotation speed of the polishing pad should be well adjusted to make a good interface between the pad-particles-sample. With optimized conditions the rotation speed was about 400 rot/min for a charge of 3 kg on the samples.

V.2.3 Analyzing the sections

Once the surface prepared, two types of analysis were done:

- Extraction of cavities was done using SEM imaging. After comparing images obtained by secondary (SE) and back scattered electron (BSE) detectors, the BSE images were found to have a better contrast between the matrix and cavities, which made segmentation of cavities easier. The BSE-SEM imaging was performed after each polishing step.
- Crystallographic orientation of the grains was determined by EBSD. This analysis should cover the entire surface. As the analysis area is very large, the EBSD acquisition was performed in the cartography mode of the system. A smaller area at a higher magnification was scanned first and then the sample stage was mechanically moved to the neighbor zone. Then the maps were stitched together using HKL Channel 5 software. Therefore this acquisition corresponds to a wide field of view.

The wide-field EBSD measurement of a 0.8 mm x 1.2 mm surface (step size 1 µm) takes about 8 hours, which renders impossible performing it on all the layers. It was decided to do EBSD scans only after the removal of 4-5 µm (every 5th layer on the average). This is justified by the relatively large average grain size of about 30-40 µm of the studied samples (Figure V-7).

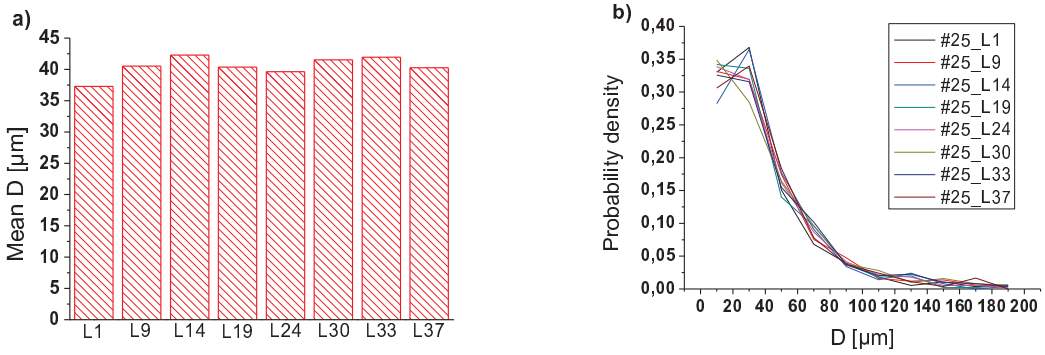

Figure V-7 EBSD results of the sections (a) the mean grain size and (b) the distribution of the grain sizes on all layers - sample deformed at 773 K and 10 MPa

V.2.4 Measuring the thickness of the removed material

In section V.1.2, the conventional method was criticized as being not sufficiently precise. The goal of the present method is to measure the locally removed material on the entire sample surface and not just at the indents. For this purpose the optical interferometer described in section III.2.3 was used. Similar to the EBSD case a stitching scanning method was selected (X50 objective) that enabled imaging small charts of 0.23 x 0.17 mm^2 (averaged on 4 measurements each), which were then stitched together. The acquisition time of one large surface was about 15 minutes. Figure V-8 shows a characteristic image obtained by this method.

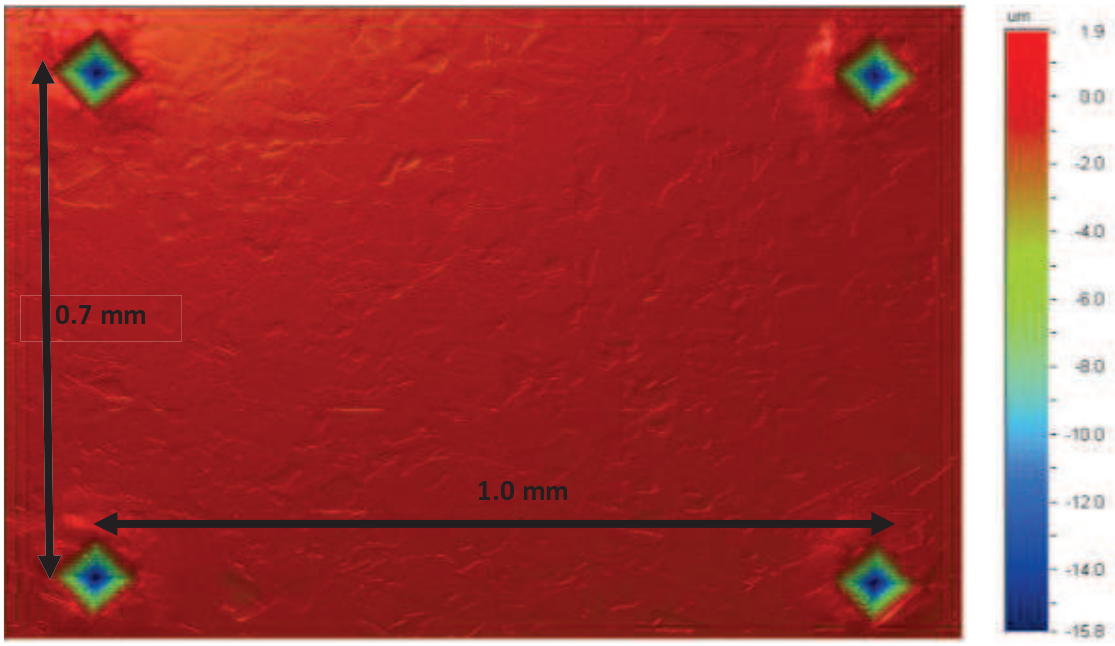

Figure V-8 Example of surface topography obtained with the Wyko NT 9100 optical interferometer

Such maps were obtained before and after polishing. To calculate the thickness of the removed material one needs, however, neutral reference zones where the surface topology does not change while polishing. These reference zones were chosen to be bottom of the indents at the vertices point of the indentation pyramid. As it is presented in Figure V-9 it is hard to precisely determine the coordinates of these reference points.

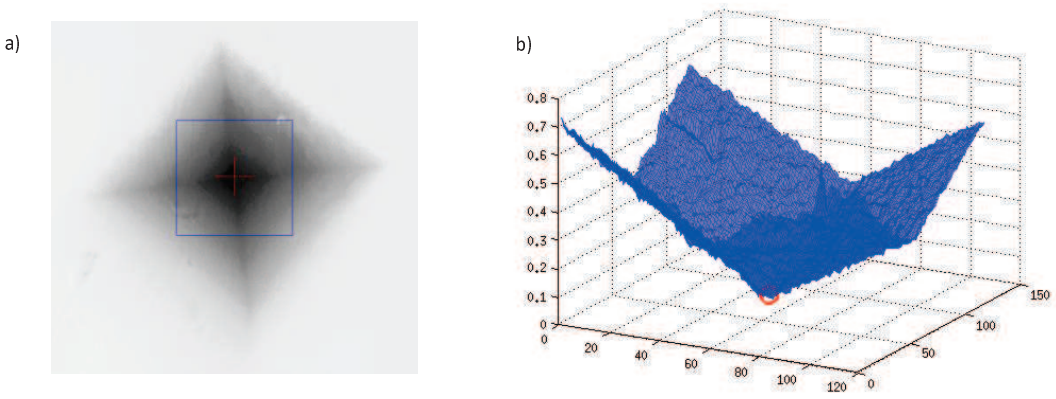

Figure V-9 Two-dimensional (a) and three dimensional (b) presentation of one indent. Topography obtained using an optical interferomter (normalized coordinates)

On a three dimensional profile, however, the reference bottom point can be extracted using the planar shape of the pyramid faces. It means that we can fit planes on the data at each of the 4 faces and the reference point will be given by their intersection (three planes to determine the point is sufficient, the 4th plane is used to improve the estimation accuracy. Examples of the slope of the indent faces are shown in Figure V-10.

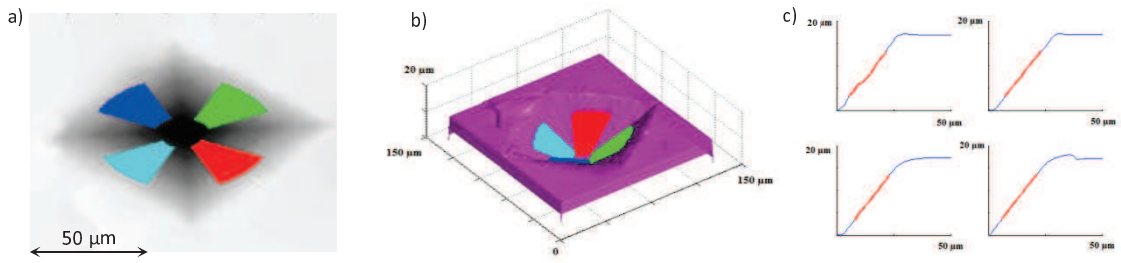

Figure V-10 Fitted planes on the indent walls showed (a) in 2D and (b) in 3D. The red portion of the curves in (c) show the part of the indent face where the planes are fitted

Once the four reference points (the bottom of the indents) were obtained, a reference plane can be defined as the plane that is passing through all of them (again, three points are enough to define the plane, the forth is used for accuracy purposes). This reference plane is considered as the basis for the reconstruction together with the hypothesis that it is identical before and after polishing. So, superposing two consecutive planes should entirely superpose the topography data of the two polishing layers. This is achieved first, by calculating the plane normal (n_1 and n_2) for each layer, and aligning each of them parallel to n_0 as shown schematically in Figure V-11. This is the vertical alignment procedure.

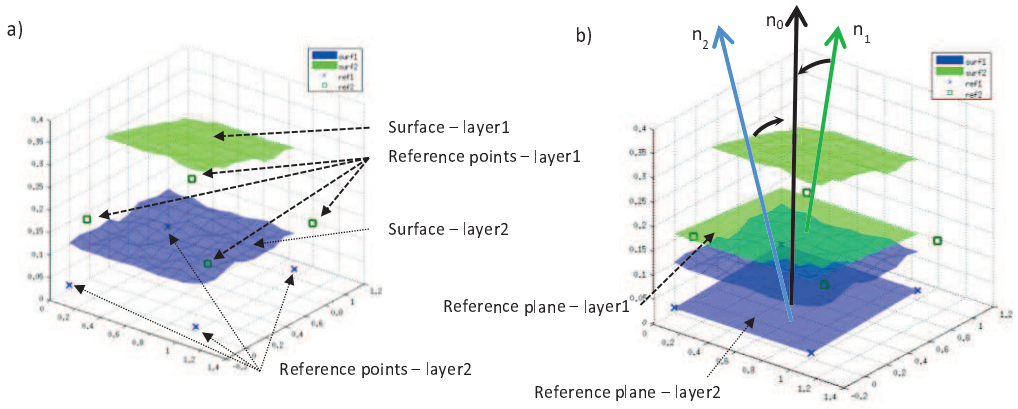

Figure V-11 Simulated data of topography (a) showing the reference points for each layer and (b) the reference planes of each layer, their normal, and the upright position (simulated coordinates are not representing the real sample geometry)

Using this method, the normal of the calculated reference planes are brought into superposition, but in reality the reference points will not be 100% superposed due to experimental error. Figure V-12 shows the reference points of two consecutive layers superposed on each other. One of them is also shown in higher magnification to view the displacement between the reference points. A schematic drawing shows in two dimensions the position of the real reference plane regarding to the calculated one. Angle β is showing the estimated error between the real and calculated planes. This angle is calculated experimentally and has a value below 1°.

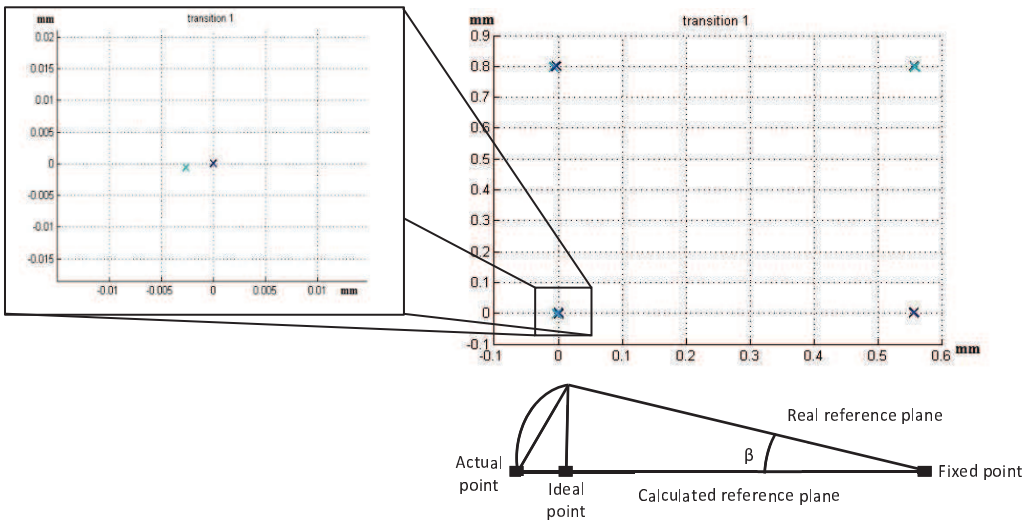

Figure V-12 Error estimation of the reference plane calculation

Once the planes were aligned parallel to each-other a coordinate system is defined at one of the reference points (Figure V-13-a). The mean thickness of the removed material between two consecutive sections can be then readily calculated by subtracting the coordinates of the corresponding two planes fitted to the surface topography (as indicated by the black ROI in Figure V-13-b).

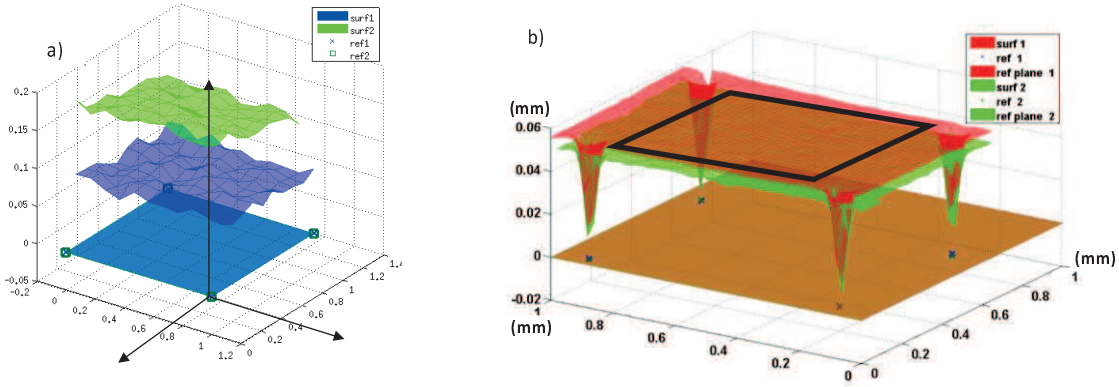

Figure V-13 Superimposed layers of (a) simulated data showing also the new coordinate system (coordinates are not representing the real sample geometry) and (b) of real data obtained by optical interferometry (showing the zone where the mean removal depth can be calculated)

Using the new coordinate system if we subtract the height of each pixel at level 1 from that of the same pixel at level 2, we obtain the removed material thickness of the pixel. This information can be stored in a gray level image. The resulting image is then named "the difference image" (shown in Figure V-14 beside the SEM image for comparing them). Based on the desired precision, 8, 16 or 32 bit image can contain the necessary information, which can be converted at any moment to µm scale by knowing the scale factor.

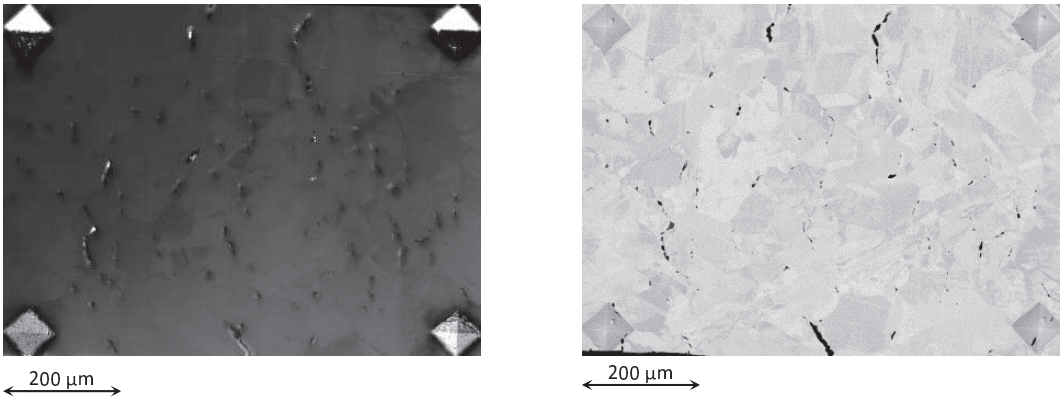

Figure V-14 The calculated "difference image" (left) and the SEM-BSE image (right) of the same zone after polishing

The data required to reconstruct the pores are their position (x, y) that we obtain from SEM imaging and their relative height with regard to the reference zero plane obtained with the profilometer. The local height of the pores is estimated from their neighbor voxels by using a large mean filter (100x100). Topography information was considered only to describe the surface and not for the reconstruction of the shape of the voids.

V.2.4.1 Transition layers

It was explained in the previous sections that the depth of the indents are not enough to cover the entire depth of the analyzed volume. For these reasons, the indents should be renewed from time to time, which requires special "transition layers" where a total of 8 indents will be present. The new indents are placed close to the old ones and serve for transmitting the reference plane information. Figure V-15 explains schematically this transition procedure.

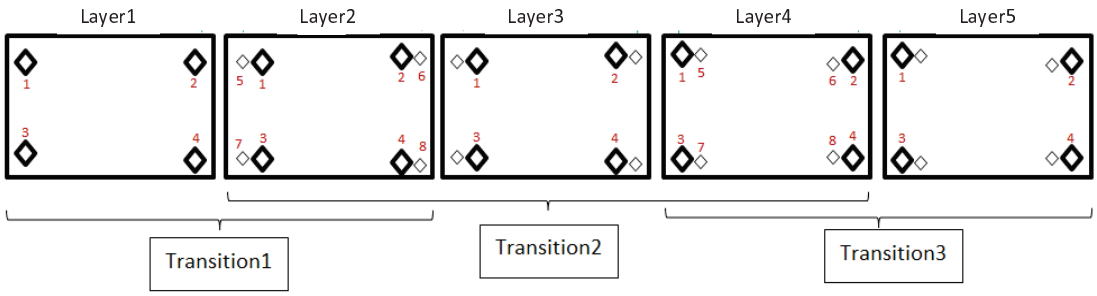

Figure V-15 Schematic descriptions of transition from one set of indents to the next ("transition layers")

The numbers marked in red beside the indents show the priority of the indents to be shown to the "P-meter" software handling the transition layers (the software is explained in the following section). The automated alignment of topography scans for the sample deformed at 773 K and 10 MPa is shown for two transitions in Figure V-16.

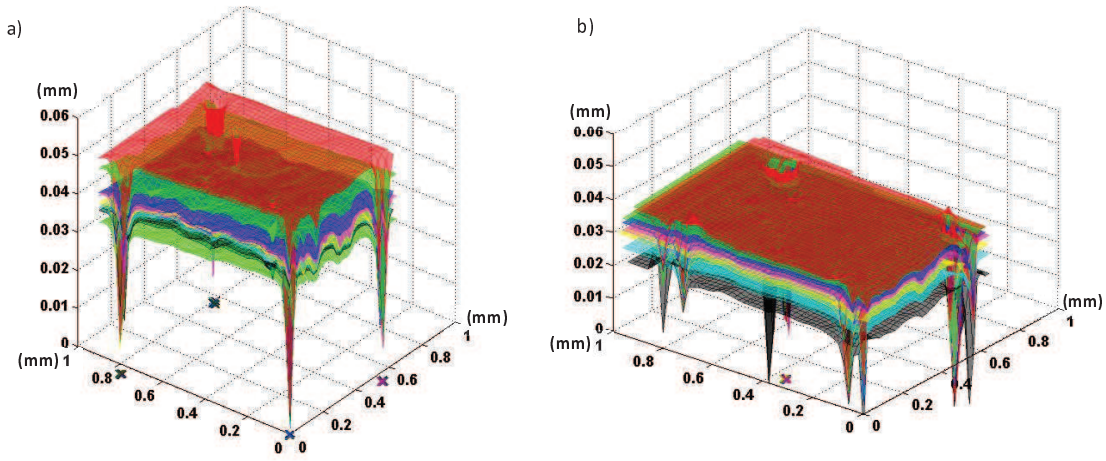

Figure V-16 Superimposed topography maps of (a) transition1 and (b) transition2 of the sample deformed at 773 K, 10 MPa

V.2.4.2 Automated calculations

Since manual alignment of the surface profiles can be quite tedious the algorithm was implemented in a home-developed Matlab software named "*P-meter*" [101] that has the following capabilities:

- Loads the raw data from profilometer
- Calculates the reference points of each indent
- Calculates the reference plane of each layer
- Changes the reference plane for the transition layers (explained in section V.2.4.1)
- Superimposes the layers, calculates and stores the "difference images" between each two layers
- Reconstructs the cavities

V.2.4.3 Polishing rates

Two sample series were serially polished. One deformed at 573 K and 80 MPa, the second at 773 K and 10 MPa. Due to imperfections in the acquired data the automated software presented above cannot be blindly applied and contrary to our aim manual intervention was needed from time to time. This makes the reconstruction procedure semi-automatic, requiring a long time for a complete 3D reconstruction. Therefore, in this manuscript only the samples corresponding to the beginning of the tertiary creep were analyzed.

On the sample deformed at 773 K and 10 MPa a total thickness of 40.91 µm was removed in 37 polishing steps. The mean removal rate was 1.10 µm per layer with a mean standard deviation of 0.56 µm. The reconstruction contains 5 transitions of the reference indents. The mean removal depths on each layer together with the cumulative removal are presented on Figure V-17. A total of 8 wide-field EBSD scans were performed, which are indicated by red points in Figure V-17-a.

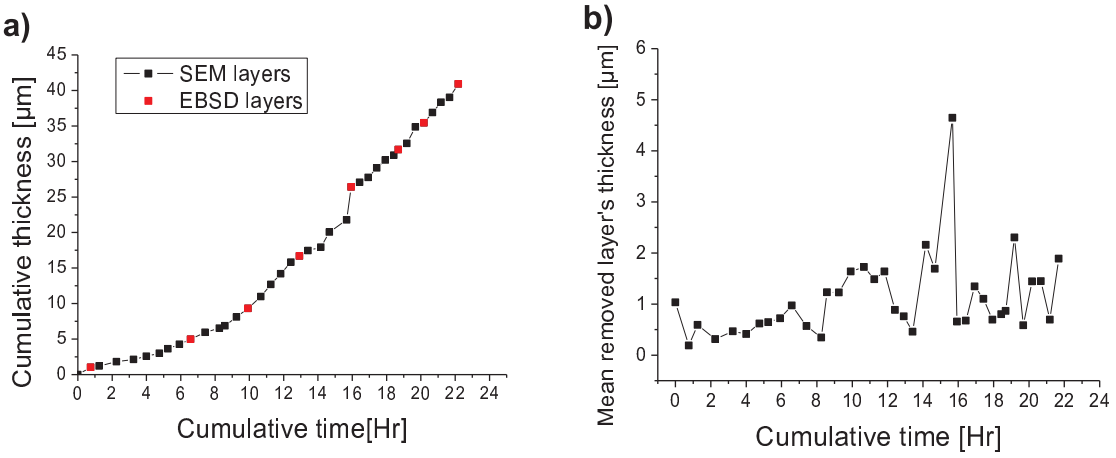

Figure V-17 Cumulative (a) and mean (b) material removal of sample deformed at 773 K and 10 MPa stopped at the beginning of the creep zone III.

The curve of the individual removal rate on each layer shows that the removal depths vary from 0.2 µm to 5 µm. It shows that the procedure of CMP is not 100% under control. But, it should be emphasized that nearly 22 hours of cumulative polishing procedure on this sample was performed successfully as the mean removal rate of 1.10 µm is close to the objective of 1.0 µm initially fixed. Also, the quality of EBSD indexation ratio (about 99.3%) on all the 8 layers shows the good quality of finished surface. The change in the removal rate after 10 hours of polishing is simply due to a switch to a new polishing cloth indicating that the quality of this plays an important role in the efficiency of polishing.

The second sample chosen for reconstruction (573 K, 80 MPa) was also stopped at the beginning of the tertiary creep stage. After 39 polishing steps a total material thickness of 39.9 µm was removed with a mean removal rate of 1.10 µm/step and a mean standard deviation of 0.56 µm (Figure V-18). 4 reference indent transitions were used and 9 large-field EBSD layers were scanned. Again, the visibly increasing removal rate after 22 hours of polishing was due to a change of the polishing cloth.

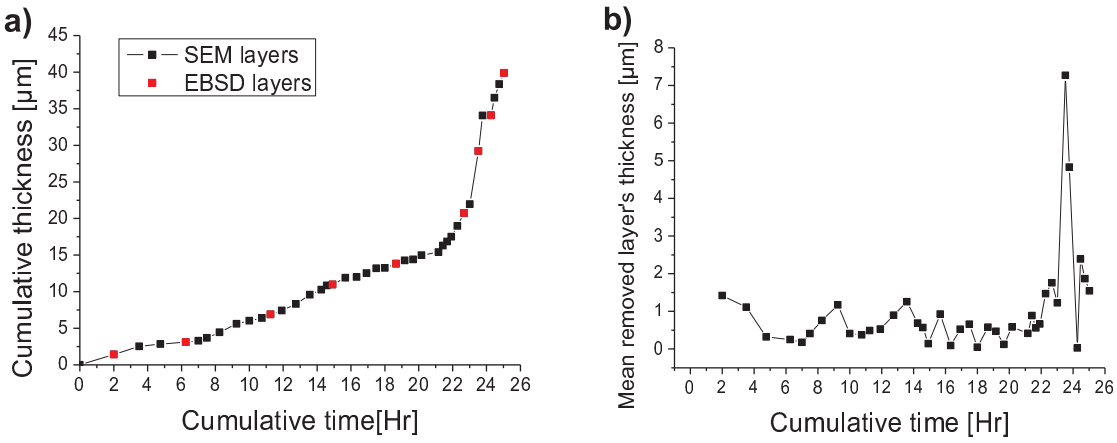

Figure V-18 Cumulative (a) and mean (b) material removal of sample deformed at 573 K and 80 MPa (deformed until the beginning of tertiary creep stage).

V.2.5 Serial sectioning cycle

In summary, the sectioning cycle is reviewed and presented schematically in Figure V-19.

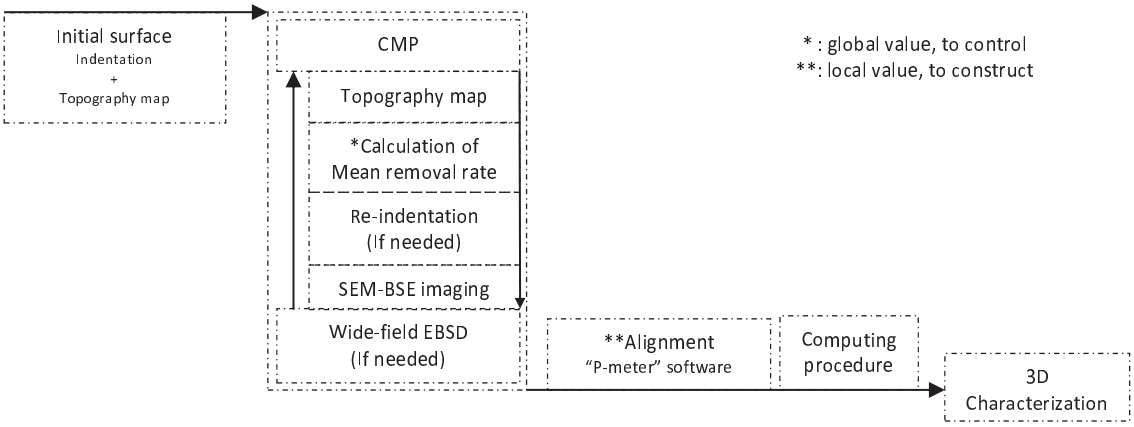

Figure V-19 Reviewed serial sectioning cycle

V.3 Computing procedure

V.3.1 Data alignment

V.3.1.1 Aligning strategy

In order to perform the 3D reconstruction the different images obtained with the different techniques (profilometry, SEM & EBSD) should be aligned. For the purposes of simplicity each stack of images obtained with SEM-BSE or profilometer are treated separately. First, they were superimposed inside their own respective stack of images. Then using a correlation technique the first layer of profilometer stack is correlated to its corresponding layer of the BSE stack. Knowing the transformation matrix between the first layers, this was applied to the entire profilometer stack. This brings the topography data in coincidence with the information coming from the microstructure (Figure V-20). To add the crystallographic information it is preferred that each layer is registered with the corresponding layer of the BSE stack.

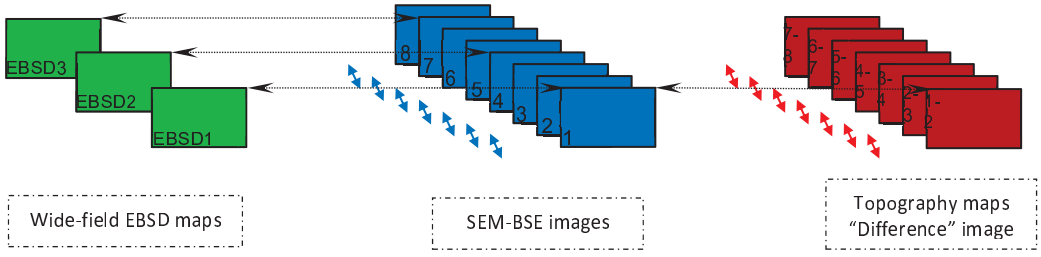

Figure V-20 Alignment procedure of images obtained by SEM, EBSD and optical profiling

V.3.1.2 SEM image alignment

Regarding the fact that the samples are placed sequentially in the SEM the image of a layer may be translated and rotated with regard to a previous one. The conventional method used to superpose 2D projections such as the images obtained by SEM is a rigid body projective transformation called the 'affine' transformation, a 3D transformation in the 2D space, which preserves the straight lines and ratios of distances between points lying on a straight line. This

transformation is described by Equation V-2 which has 6 unknown coefficients. They can be obtained by solving a set of linear equations.

$$\begin{bmatrix} \acute{x} \\ \acute{y} \\ 1 \end{bmatrix} = \begin{bmatrix} r_1 & r_2 & t_1 \\ r_3 & r_4 & t_2 \\ 0 & 0 & 1 \end{bmatrix} \begin{bmatrix} x \\ y \\ 1 \end{bmatrix} \quad \text{Equation V-2}$$

where, $r_1 : r_4$ are the coefficients of a rotation matrix, $t_1 : t_2$ the coefficients of a translation vector. At least 3 control points are needed to solve for the 6 unknown coefficients. In conventional case, only identifying the base of the indents would be sufficient to calculate the transformation matrix.

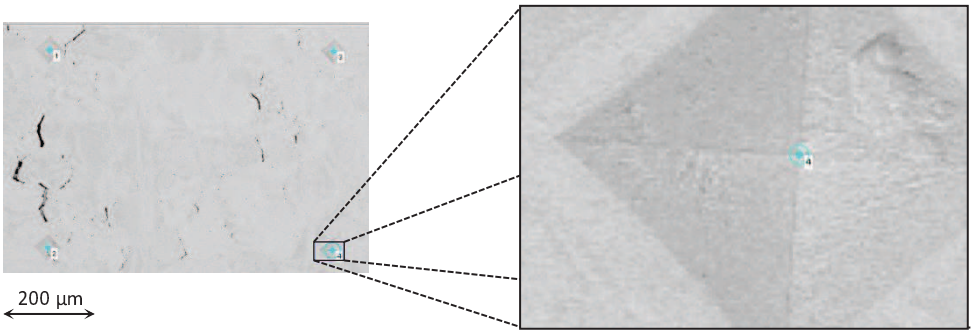

Figure V-21 Control points for projective transformation are the base of the indents

It should be mentioned that by increasing the number of control points the transformation matrix becomes more accurate. These can be found by cross correlating small ROI's of 100 pixels x 100 pixels between two consecutive images. Local cross correlation is repeated until 100 points giving high correlation coefficient are found. Equation V-2 is then solved in a least-square sense.

Figure V-22 shows the SEM image of two consecutive layers together. The arrows indicate the local displacement of the control points. It is visible that more arrows are present in areas with some features. It should be mentioned that a histogram equalization procedure before this step increases the correlation coefficients between images.

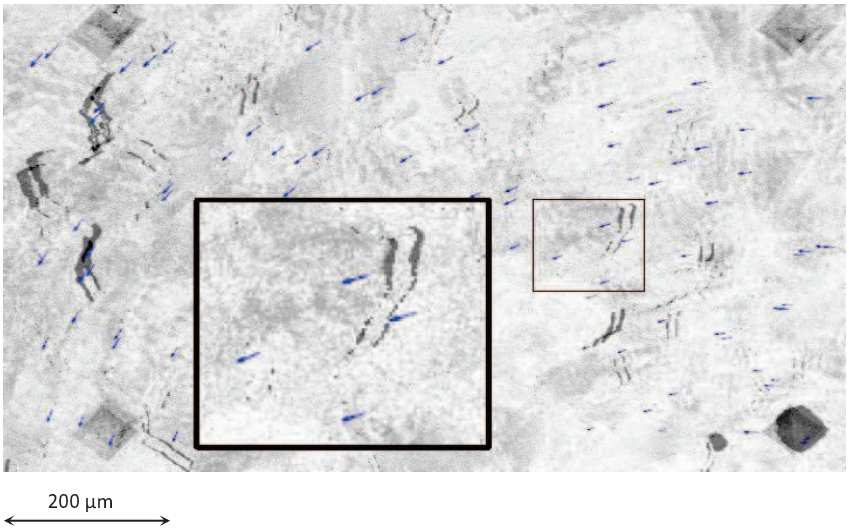

Figure V-22 Two overlaid consecutive SEM images with arrows showing local displacements of the selected ROI

V.3.1.3 EBSD alignment

It is more difficult to correlate SEM images with EBSD maps. When sample is tilted at 70° (for EBSD scan) an additional tilt correction becomes necessary. In this work we have selected to correlate SEM images with band contrast maps of EBSD. Luckily they present a very good similarity. So, the cross correlation method was again applied between the SEM image and the band contrast image. The transformation matrix brings the features of the EBSD band contrast image in superposition with the SEM-BSE image. This matrix is then applied to the Euler and the grain boundary maps (presented schematically in Figure V-23).

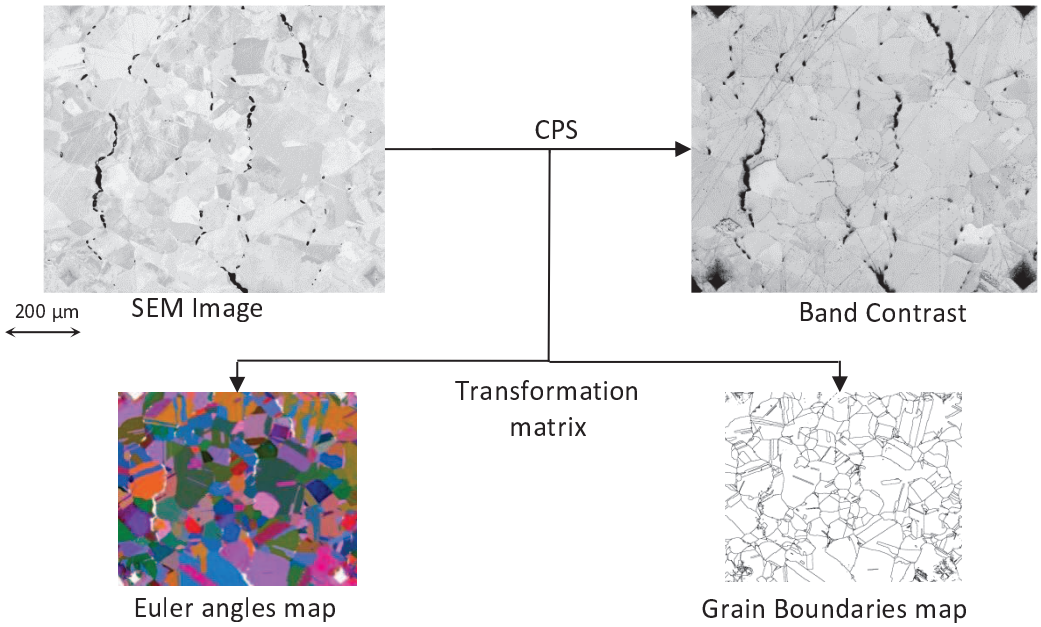

Figure V-23 Alignment procedure of EBSD maps to equivalent SEM images using the local cross correlation algorithm based on the EBSD band contrast image and applying the transformation matrix to Euler angles grain boundary maps.

It should be emphasized that applying this kind of transformation matrix to an image always requires interpolation of data as a result of the mismatch between the Cartesian coordinate systems. A nearest neighbor interpolation type was chosen to prevent distorting the physical information contained in the images. Using nearest neighbor interpolation, data missing is copied directly from a neighbor pixel.

V.3.1.4 Topography map alignment

The alignment of the topography data is already done by the "P-meter" software (section V.2.4.2). Once the aligned "difference" images generated, it was observed that they also have mutual features with the SEM-BSE images (Figure VI-14). So, again using cross correlation the SEM image of the first layer could be aligned with that of the corresponding difference image. The obtained transformation matrix was then applied to the entire topography stack.

V.3.2 Three dimensional creep voids

The 3D reconstruction of the pore network is composed from three main steps which are the segmentation, the labelling and finally the reconstruction. These steps are detailed in the following sub-sections.

V.3.2.1 Segmentation

There are several categories of segmentation algorithms for images:

- Region-based segmentation, which attempt to partition or group regions according to common image properties such as: intensity values, textures or patterns etc.
- Region growing methods such as the watershed algorithm
- Curve evolution methods such as the level set algorithm
- Clustering methods
- Edge-based segmentation related to the calculation of gradient image
- Thresholding, or segmentation based on the intensity of pixels
- Methods based on a combination of the above

The difficulty encountered in the segmentation of SEM images is related to the influence of the indents and sometimes to impurity particles on the surface, which have nearly the same grey levels as the voids. Segmentation was done using the Avizo software [102]. A mask image was selected manually, which hides the unwanted zones. A watershed algorithm was then applied on the rest of the image that uses the gradient image marking the edges of the pores. The mask image and the segmentation result are shown in Figure V-24.

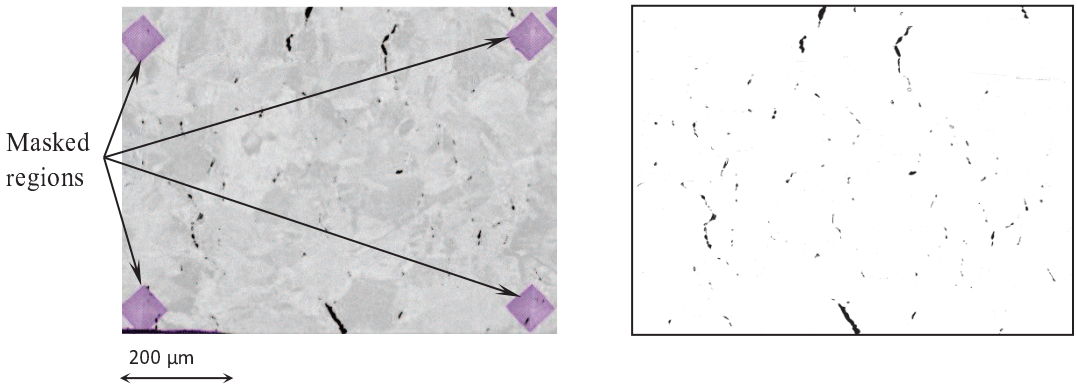

Figure V-24 Segmentation procedure (left) the mask image superimposed to initial image and (b) segmented image

V.3.2.2 Labeling the pores

Binarized images of voids from different layers should be now linked together. When a stack of superimposed images is formed the pixels find new neighbors in the third direction so, they become voxels. The connectivity of a voxel is described by its relationship to its neighbors. Compared to a pixel's connectivity, which can be up to 8 (usually 4 or 8) the connectivity of a voxel is much higher and usually defined by 10 (8+2) or 26 (8+9+9). This connectivity is schematically shown in Figure V-25.

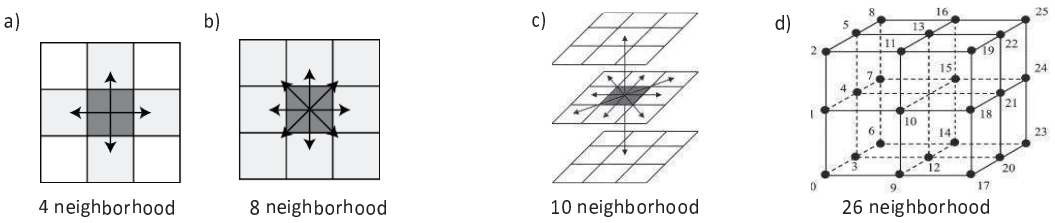

Figure V-25 Connectivity of pixels (a, b) and voxels (c, d)

The labelling process is performed on the binary image. It associates an ID number to the pixels/voxels coupled to each other in a given connectivity. In our case a 26 neighbor connectivity

filter was used to identify the 3D voids. The ID of each pore is stored on all the voxels forming that pore and as there as there are more than 256 pores in the matrix the numbers are stored in separate 16 bit images called “label image” (Figure V-26).

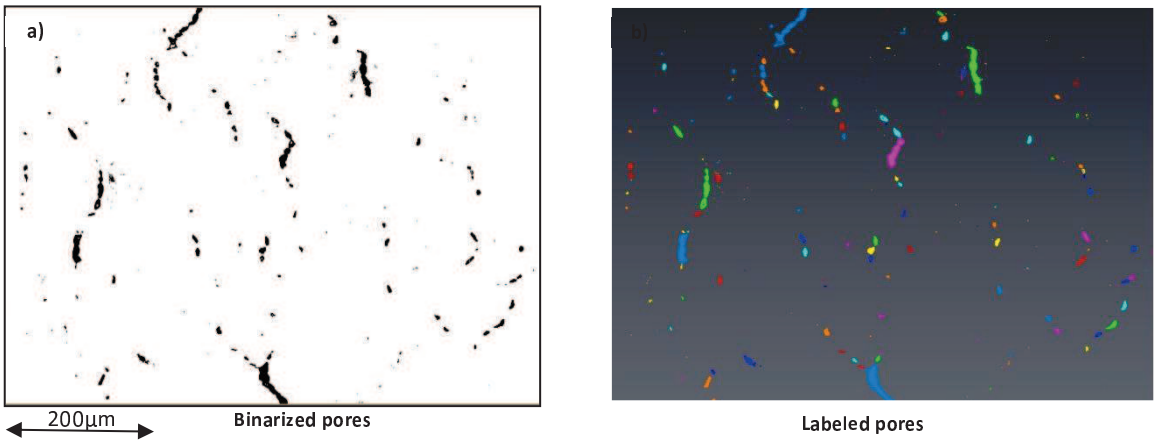

Figure V-26 (a) Binarized pores voxels are relinked in three-dimensions and get a label (b).

V.3.2.3 Pore reconstruction

V.3.2.3.1 Average height method

The label images are still not suitable for 3D reconstruction because of the non-equal distance between layers. In conventional serial sectioning, the solution to this problem is to define a regular grid and interpolate between the measured layers (schematically explained in Figure V-27).

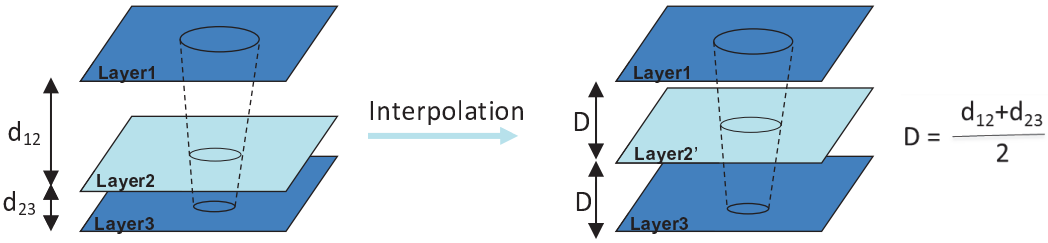

Figure V-27 Unequal distance between the layers can be fixed by making a regular grid (requires interpolation)

V.3.2.3.2 Local height method

Every pixel of the structural image has a (x, y, z) coordinate based on the real topography. Using this local height information the coordinates of each voxel making up the pore are extracted separately. The reconstruction of the void is done using all surface voxels and the Delaunay triangulation algorithm. Once the cavities reconstructed, the Avizo software allows cutting the volume into parallel sections and storing the real-shape cavities in the form of images.

An exaggerated schema (Figure V-28) shows the difference between local and average height methods for 3D reconstruction of the pores. Two grains are shown on the two sides of a pore, which is situated on a slope. The material removal rate of the grain2 is considered to be higher (green curve) or lower (red curve) than that of grain1.

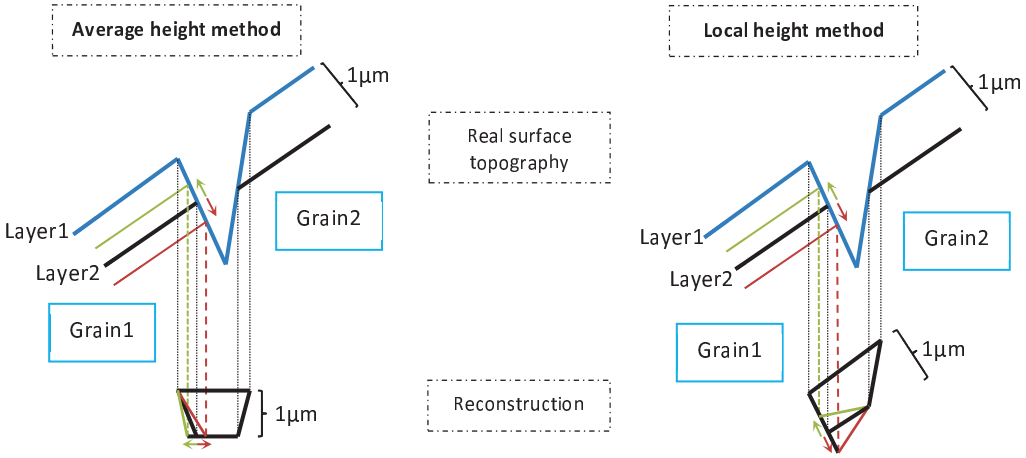

Figure V-28 The difference between the average and local height methods – a pore is shown on a slope in the boundary grains 1 and 2. The local topography effect is shown by changing the first grain's local height to a level higher (green curve) or lower (red curve) than the surface plane. The influence of this local height is then shown at the reconstructed volumes. The reconstructed volume is shown to be more realistic using local height data.

The same volume is reconstructed twice; once using average heights and in a second time using the local heights. The biggest pore in the sample is chosen to compare the methods. As it can be observed in Figure V-29, in the local method, the shape of the pore is more precisely defined; the volume obtained with the two approaches are nearly the same, but the local height method gives a more accurate connectivity.

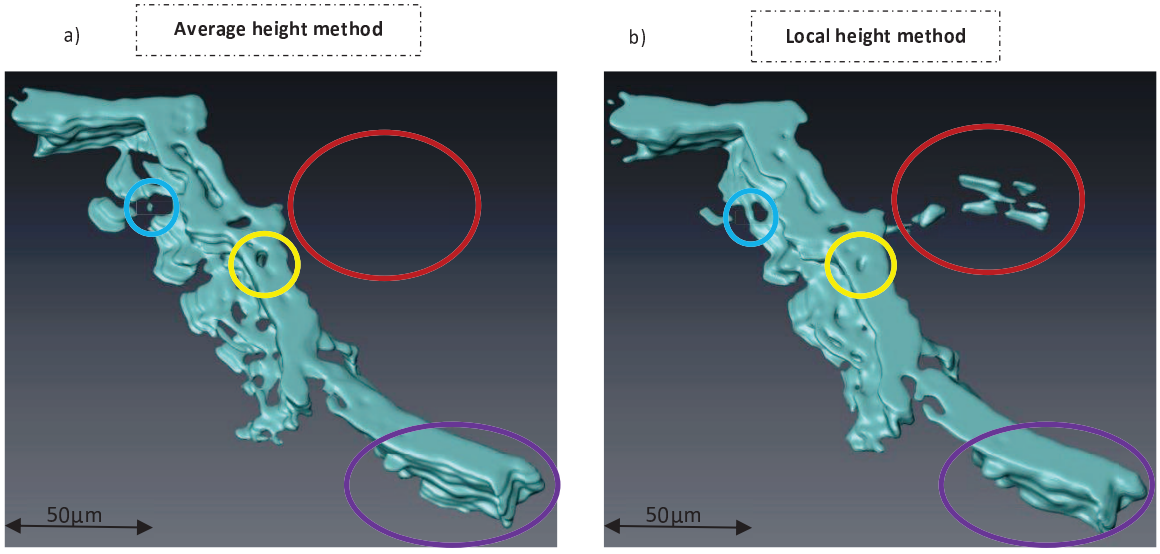

Figure V-29 Biggest pore in the volume, reconstructed by (a) average height method and (b) local height method

The reconstructed voids are visualized using Avizo (Figure V-30). It can be seen that most of the creep voids are lying in a direction perpendicular to the applied load axis.

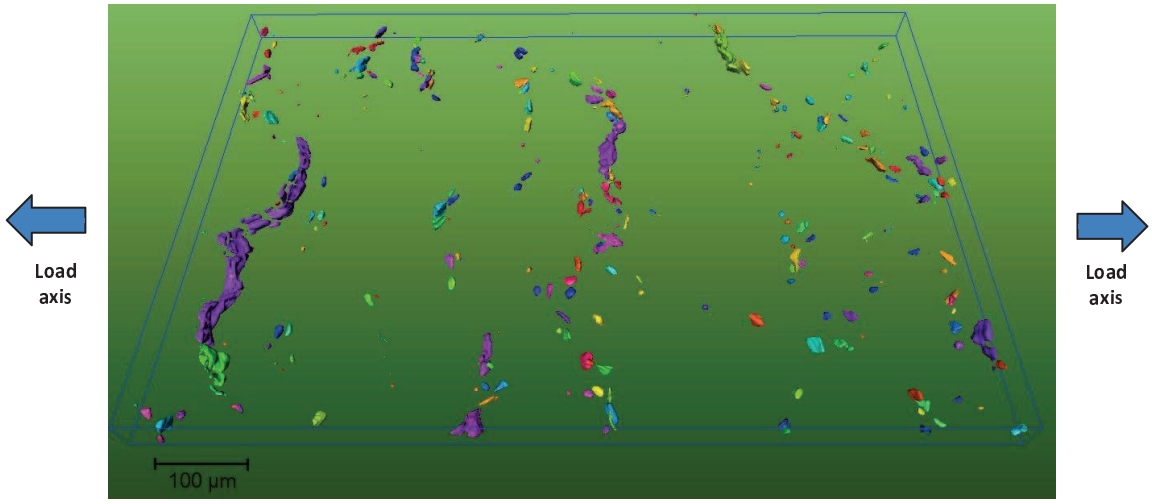

Figure V-30 Three-dimensional reconstruction of creep voids - sample deformed at 773K and 10MPa

V.3.3 The three-dimensional grain structure

If the serial sectioning methodology described above is extended to encompass many contiguous sections through the microstructure and interfered with EBSD, a three dimensional orientation map can be built up. Such a reconstruction tool gives access to connectivity parameters of the microstructure – the grain boundary network, triple junctions, creep pores, crystallographic orientation, etc. The main technical challenge involved is the precise vertical registration between sections and reproducibility in the specimen position with respect to the reference parameters of the SEM. An essential task of the reconstruction by serial sectioning is establishing the correct spatial and orientation registration for the sequential sections of EBSD data. Fortunately, these two processes are performed sequentially.

V.3.3.1 Orientation corrections

The EBSD data sets were analyzed using HKL Channel5 software. In an EBSD dataset not all points of the map are indexed with the same level of confidence in orientation. This may be for example, due to a diffraction pattern including information from two orientations in the probed volume. Therefore, it is reasonable to consider a strategy to replace low confidence points based (in proportion of 0-2%) on a detailed comparison with the neighboring data points. Within the HKL Channel5 software, confidence in indexing is reported as the Mean Angular Deviation (MAD) number. It is suggested that the confidence in indexing EBSD patterns is nearly constant for MAD numbers greater than 0.2, whereas the accuracy decreases sharply for lower confidence indices. An algorithm was integrated that associates the orientation of a low confidence index point with that of its neighbors with common contiguous orientation. Using this algorithm, the spurious data points have been smoothed. This is observable for single points at the center of a large grain whose orientation differs from its neighbors. In particular, the correction procedure makes high angle boundaries contiguous in character, as expected, and renders surface flaws such as scratches that had been mistakenly indexed as boundaries.

V.3.3.2 Data alignment in orientation

Spatial alignment procedures tacitly assume that the measured orientation of any given region shared between serial sections is identical, therefore section to section rotational alignment of each EBSD data set is a pre requisite. Any rigid rotation of the specimen between scans will introduce a rotational “offset” between sections. To correct this, a reference crystal of known orientation must be present in each serial section EBSD scan. Assuming that the orientation of the

single crystal is constant from section to section any rigid body rotational misalignment may be corrected by determining the transformation required to rotate the measured reference crystal orientation back to its original value. This transformation can then be applied to all orientations of the associated scan. However, in the absence of such a system this orientation misalignment is estimated to be about one degree. In order to avoid its influence on later data analysis several orientation parameters, such as the "mean orientation spread", were calculated on the 2D datasets for which the relative orientation error is smaller (~0.3°,[103]).

V.3.3.3 Grain boundary corrections

One of the particularities of an EBSD map containing voids is that the voided zones are not indexed. These zones are not involved in the grain boundary detection algorithm integrated in HKL Channel5 software. To solve this problem a grain boundary map was prepared using a special noise reduction filter. This filter fixes the orientation of a non-indexed pixel regarding to the orientation of its neighbor. In this procedure the criterion of the number of indexed neighbors is reduced to 5 (in 2D), and it works iteratively till the indexation of all the pixels having five indexed neighbors. This criterion is enough for the pixels forming a cavity to be 'artificially' indexed. This creates some non-correct indexations at the extremity of the map (which will also be cropped later), but helps obtaining the grain boundary at the location of the creep voids (Figure V-31).

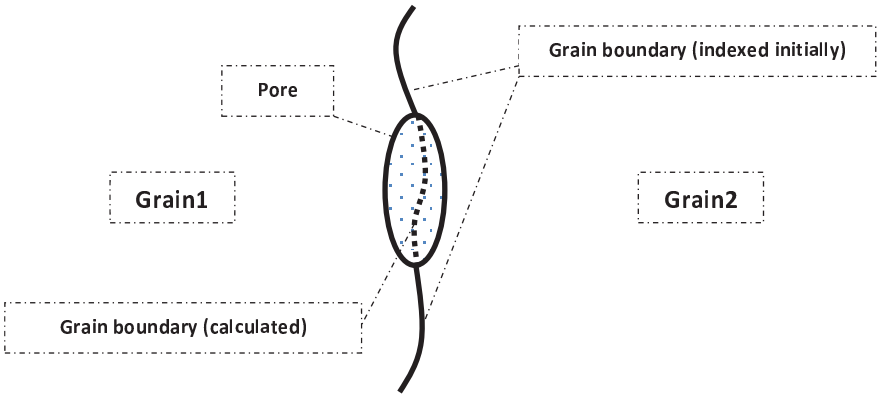

Figure V-31 Grain boundary calculation by noise reduction filter

This helps further to create a relationship between BSE-SEM image and the EBSD map. The generated orientations near the voids, however, are not used for the calculation of grain properties. Once the grain boundary network was corrected the alignment with the SEM image can be performed (Section V.3.1.3). So, it is no longer necessary to perform a section to section alignment. Since the grain boundary image is binarized, it can be inversed and the grain network can be visualized. Labeling this image we obtain an image containing all the grains in the layer and each will identified with a different number. The IDs will be stored as a 16 bit image (Figure V-32).

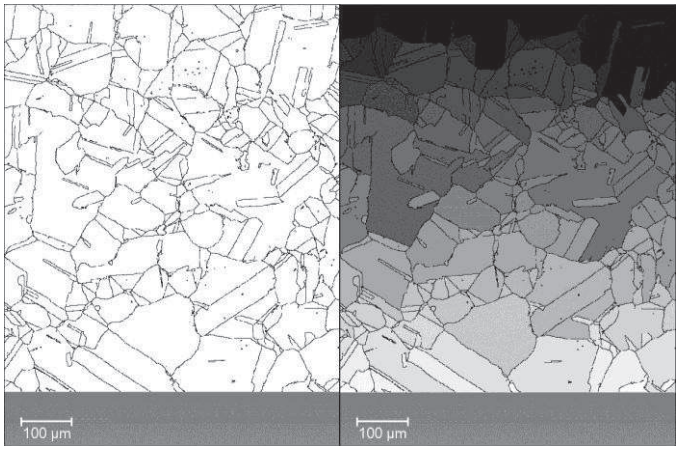

Figure V-32 (left) Corrected grain boundary network and (right) the labelled grain image.

V.3.3.4 Grain registration

The grains identified in each layer should be registered among consecutive layers to reconstruct the 3D grain network. In any normal microstructure the connectivity criteria to register a grain in several layers requires their geometrical superposition. It means that for grains with a mean size of 40 µm, cutting them into sections of 5 µm should produce sections that have a gravity center not far from each other. As it can be observed on Figure V-33, the microstructure of the studied copper samples is more complicated because of the presence of the twins.

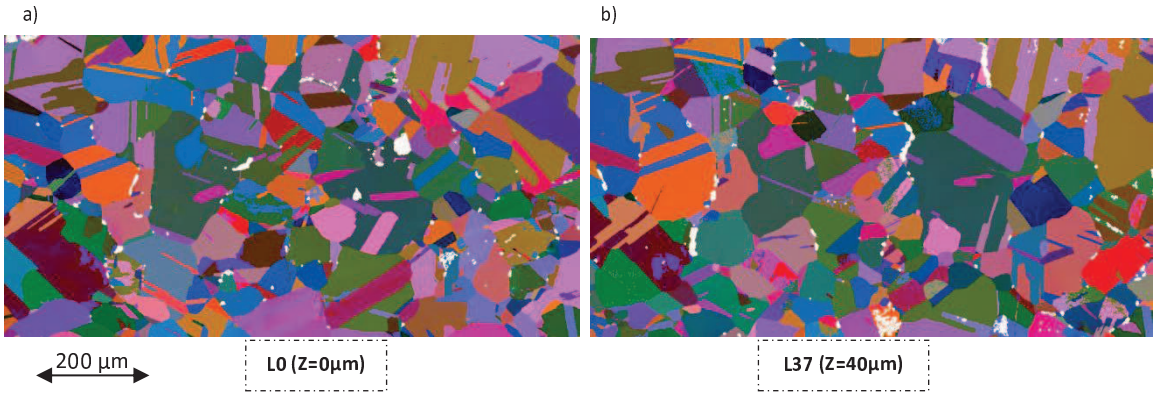

Figure V-33 Example of Euler angle maps of the sample deformed at 773K, 10MPa (a) initial surface and (b) surface after 40 µm of material removal

V.3.3.4.1 Automatic superposition

A Matlab script was developed to automatically register the grains in consecutive layer based on the following criteria:

- Gravity center: the geometrical gravity center of a grain sectioned in two layers, should not be farther than the mean grain size (40 µm)
- Size criteria: the area of the sectioned grain should not change to a large degree. (maximum factor of 4)
- Orientation criteria: The mean orientation of the layer should not change by more than 10°

Based on all these criteria a list of possible grains in the second layer are attributed to one grain in the first layer. Then the one with optimized characteristics is associated to the grain in the

first layer. The registration results were though not always reliable. The majority of the grains were connected correctly, but the presence of twins disturbed the automatic procedure.

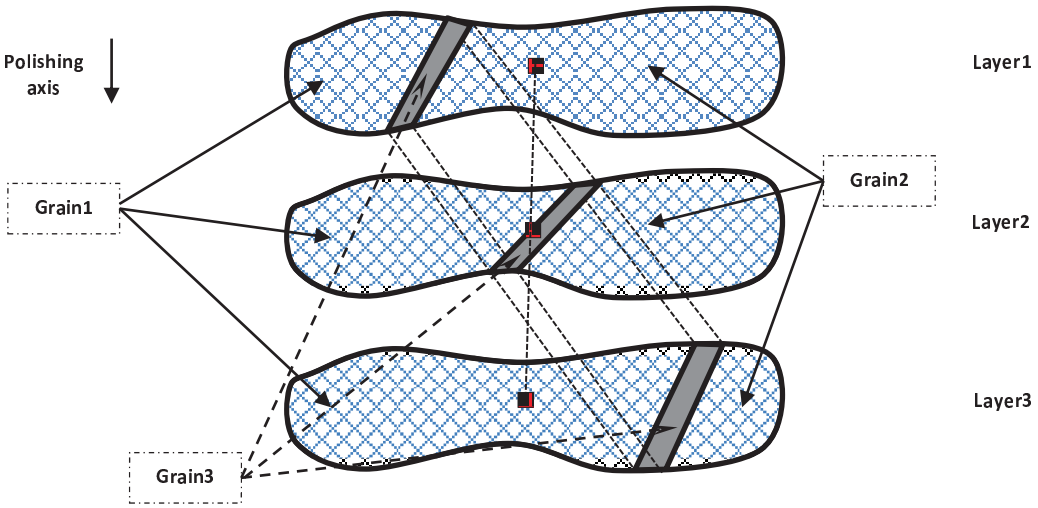

Figure V-34 Schematic drawing of the microstructure containing a twin

The twin boundaries and the grains containing twins (showed as grain3 of Figure V-34) are not necessarily aligned perpendicular to the polished plane. So, registering them from one layer to another is a complex procedure. It was decided to handle the twin problem by a manual checking procedure.

V.3.3.4.2 Manual intervention

For manual intervention a software named "reconstruct" was developed using Matlab (Figure V-35) for which the entry data is the grain label image obtained at section V.3.3.3. This software has the following capabilities:

- Zooms in to the desired level in both layers and navigate freely between layers.
- Attributes the number of the grain in the first layer to the grain in the second layer. Grains with the same number have the same color.
- Attributes a given number to any grain in the first or second layer.
- Visualizes in 3D a selected grain

The registered grains are then examined based on an orientation criterion (disorientation smaller than 10°). The ones that do not meet the conditions are then re-assigned. This procedure is repeated several times until every grain passes the test criteria. The disadvantage of the manual intervention is that it is a very long procedure, but on the other hand the results are trustful.

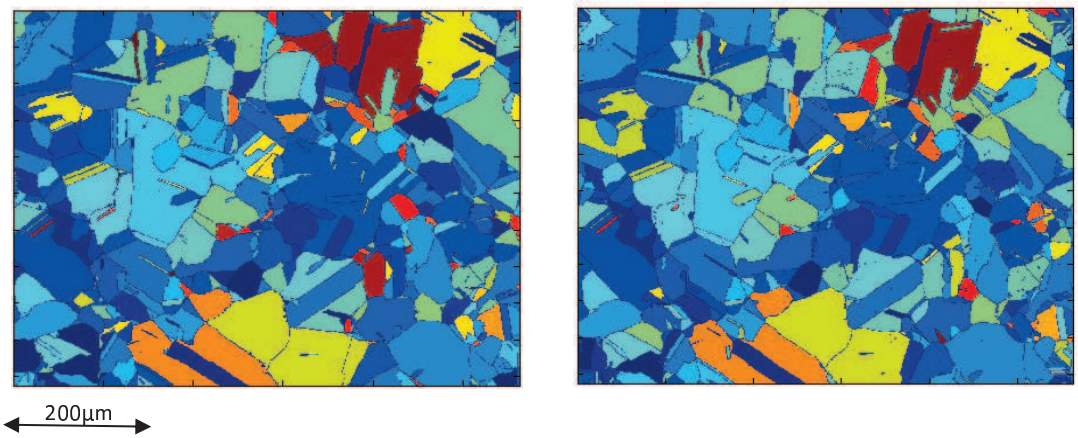

Figure V-35 "Reconstruct" software, developed for manual registration of the grain in different layers

After the registration the grains can be analyzed in three dimensions. The visualization is done by transporting the registered grains image into Avizo. Such a visualization is shown in Figure V-36.

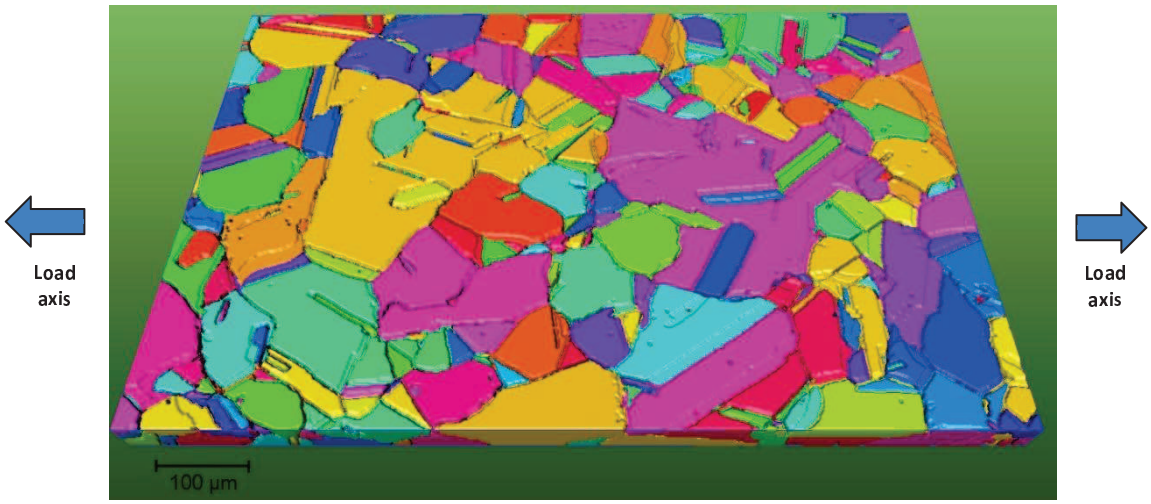

Figure V-36 Three-dimensional grain structure reconstruction - sample deformed at 773K and 10MPa

V.3.4 Coupling the microstructure with crystallographic orientation

After the reconstruction of the grain and void volumes they should be superimposed. Figure V-37 shows the grain structure in transparence to present the creep voids at the GBs. The data alignment presented in section V.3.1, insures that the pores are situated at grain boundaries. Now that the relationship between voids and grains is established we can correlate the different aspects of coupling the microstructure and crystallographic orientation. These analyses are the subject of chapter VI.

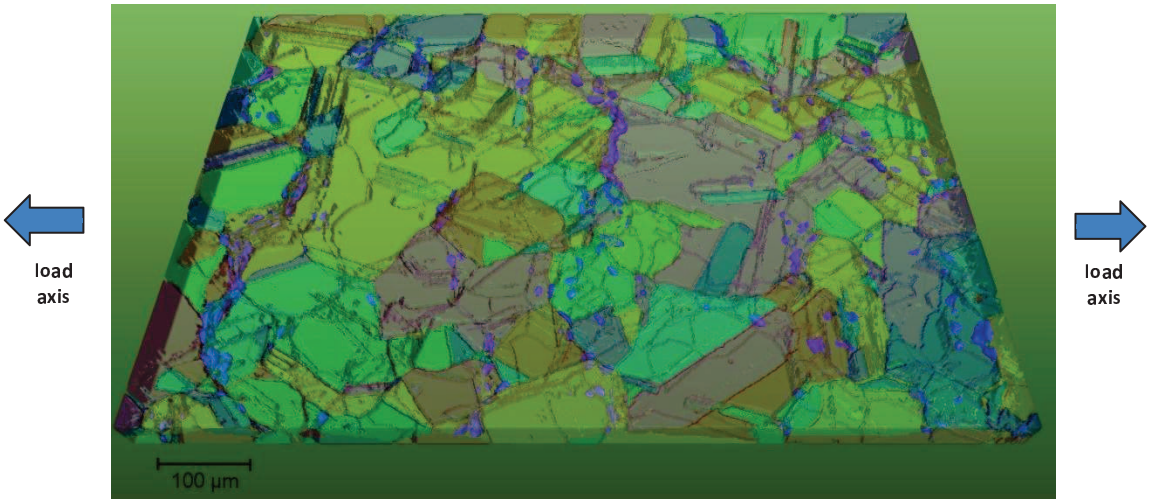

Figure V-37 Three-dimensional grain structure superimposed to the reconstruction of creep voids - sample deformed at 773K and 10MPa

VI Serial sectioning: application to creep voids

VI.1 Introduction

In chapter V a serial sectioning method was developed based on the controlled chemical-mechanical planarization technique. Combining it with an optical profilometer eliminates the necessity to produce sections parallel to each other and renders a more precise shape of the reconstructed features. Finally, a computing procedure was introduced that aligns images from different sources, combine them and builds up 3D representations of the voided and granular structure of a polycrystal. In this chapter, the reconstructed volumes are further analyzed. Using image analysis damage and crystallographic orientation details are extracted from each volume, which is expected to answer the important question on a possible correlation between damage location and the crystallographic orientation of neighbor grains.

VI.2 Thermo mechanical solicitations

VI.2.1 Creep tests

Two type of creep conditions were examined. The first test (T1) was performed at high temperature and low stress (773K, 10MPa) and the second (T2) at lower temperature but higher stress (573K, 80MPa). According to deformation mechanism maps of the literature [75] both conditions correspond to power law creep. Deformation at higher temperature is close, however, to the diffusional flow region, while the second to the power law breakdown creep region (Figure VI-1).

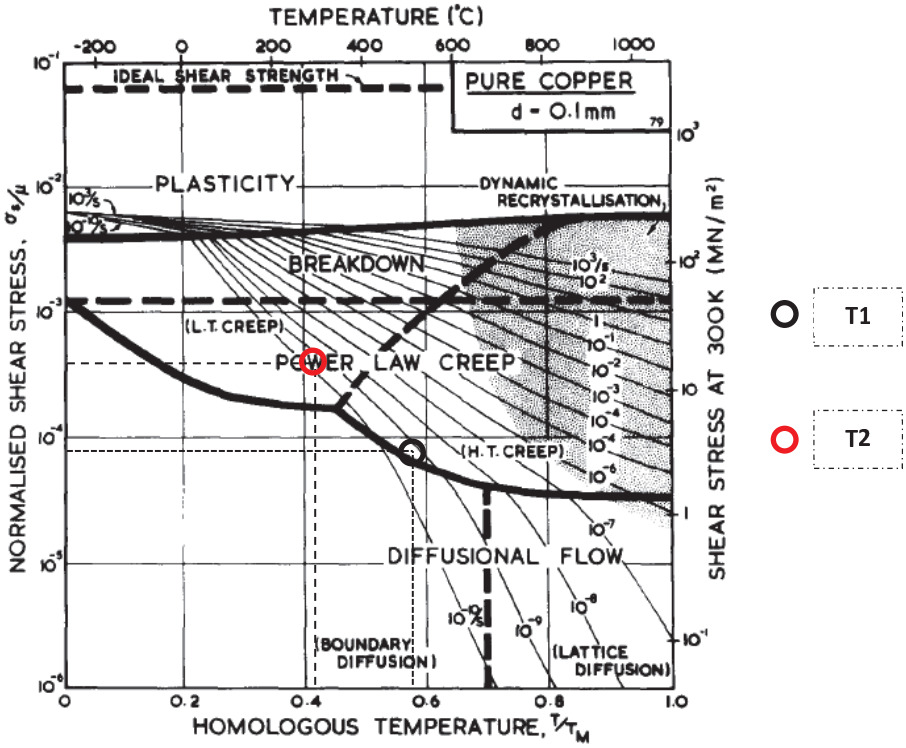

Figure VI-1 The deformation mechanism map for copper, showing the regimes of plastic deformation. Creep conditions T1 and T2 are marked on the map.

It is expected that void growth in T1 is mainly diffusion controlled, while for the T2 condition plasticity controlled growth is more important. Three samples were deformed under each creep condition and the tests were stopped at the end of the first, in the middle of the second and at beginning of the tertiary creep stages. The experimental polishing and imaging procedure was performed on all six samples until a material volume of about 1.2 mm x 0.8 mm x 40 µm was removed. However, as explained in the previous chapter, the development of the computing procedure took a too long time and only the volumes deformed until the beginning of the third creep zone were reconstructed. The creep curves of the reconstructed samples are presented in Figure VI-2.

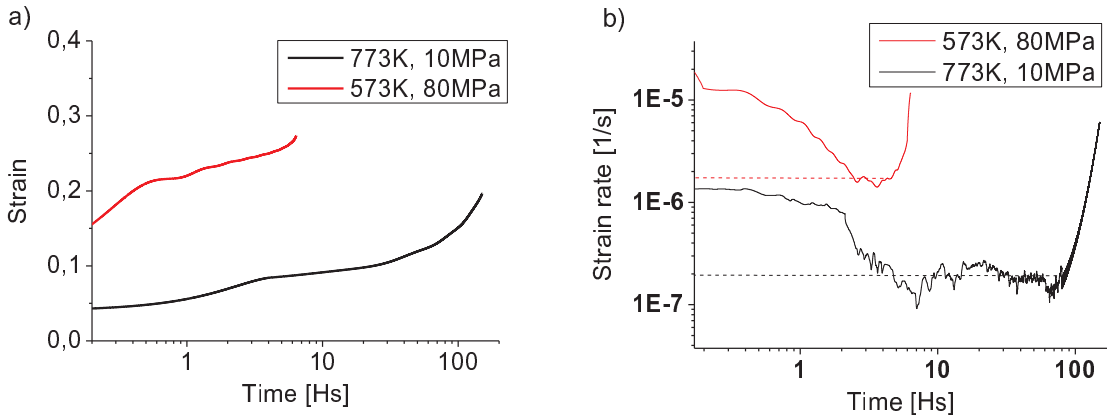

Figure VI-2 Creep curves of the reconstructed samples – creep test stopped in the beginning of the tertiary creep stage

As it can be seen in the Figure VI-2 the deformation at 773 K and 10 MPa takes about 25 times longer time than the creep test at lower temperature and higher stress. The corresponding minimum creep rates are 2.10^{-7} s^{-1} compared to 2.10^{-6} s^{-1}, respectively for T1 and T2.

VI.2.2 Texture evolution during creep

Global EBSD observations were performed on the initial state of the samples after recrystallization and after creep deformation. The texture is presented in terms of pole figures (Figure VI-3). The EBSD scans were done on the sample's longitudinal section, with x_0 parallel to the load axis. It can be noted that texture strength increases during creep deformation (maximum intensity increases from 3 to 9 and 11 for the samples deformed at T1 and T2, respectively). Deformation at T2 conditions leads to a more prominent pole distribution. This indicates that not only dislocation climb, but massive dislocation slip took also place. Since the final texture of the sample deformed at low stress is quite similar to the texture of the sample deformed at high stress one can conclude that dislocation slip took place at higher temperatures, too. This is in agreement with the Weertman's model of power law creep based on a combination of slip and climb mechanism of dislocations [104].

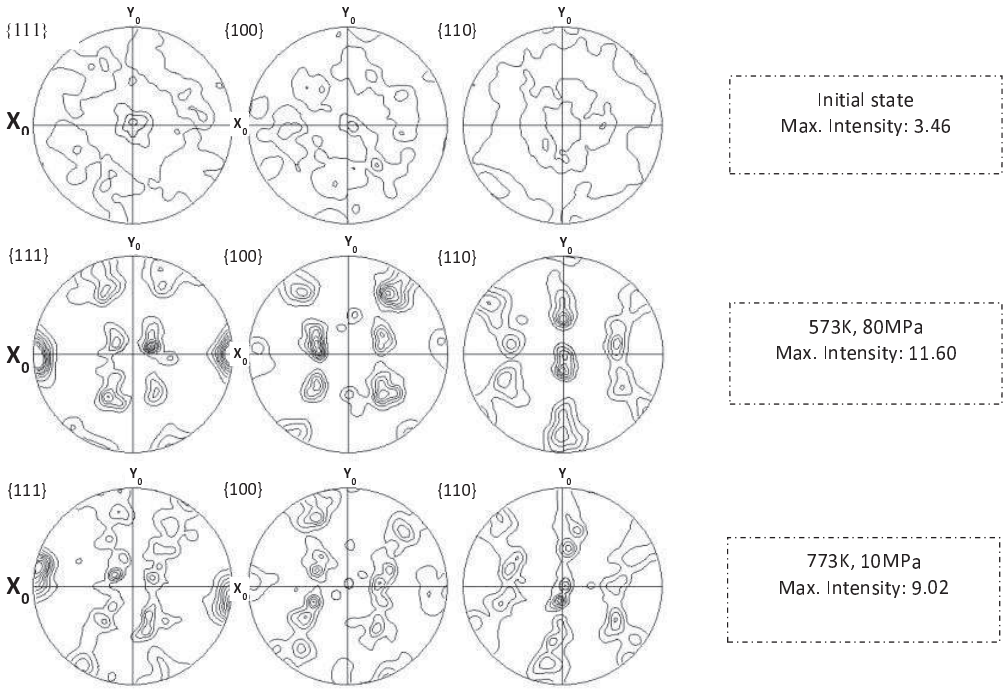

Figure VI-3 Pole figures of the samples at (a) initial state, (b) deformed at 573K and (c) deformed at 773K

Since dislocation slip is dependent on crystallographic orientation and intriguing question to answer is the following: is there any relationship between creep damage and texture, or more precisely between void location at grain boundary and the crystallographic orientation of neighbor grains? The following sections will try to find an answer to this question based on the serial sectioning method for 3D reconstruction.

VI.3 Microstructure analysis

Before extracting the statistics on creep damage the first step is to select the reconstructed creep voids. Patterson et al. [105] developed a method to systematically examine the morphological filters used in post processing of 3D imaging to better understand their effect on the final statistics of the objects therein. Using their technique, the number of voxels needed to render the objects can be determined and assured that they are due to sample heterogeneity as opposed to noise. This method is scale independent, the important parameter being the number of voxels used to render the object of interest. For example quantifying the volume of a spherical pore with a diameter of 1 µm (30 voxels needed to fill the sphere) represents a quantification with a relative standard deviation of about 10%. The quantification error decreases as the volume of the reconstructed pores increases from this minimum level (30 voxels). From the total of 18251 pores found in the sample deformed at T2 condition only 584 passed the volume filter for quantitative analysis. In case of the sample deformed at T1 the corresponding number was 535 from a total of 7369.

Beside voids with a small volume, flat pores are also avoided. Flat pores are the ones which are present only on one layer. The voids retained for analysis are visualized in three dimensions in Figure VI-4 (Avizo). It can be observed that pore distribution is more homogeneous in the sample T1.

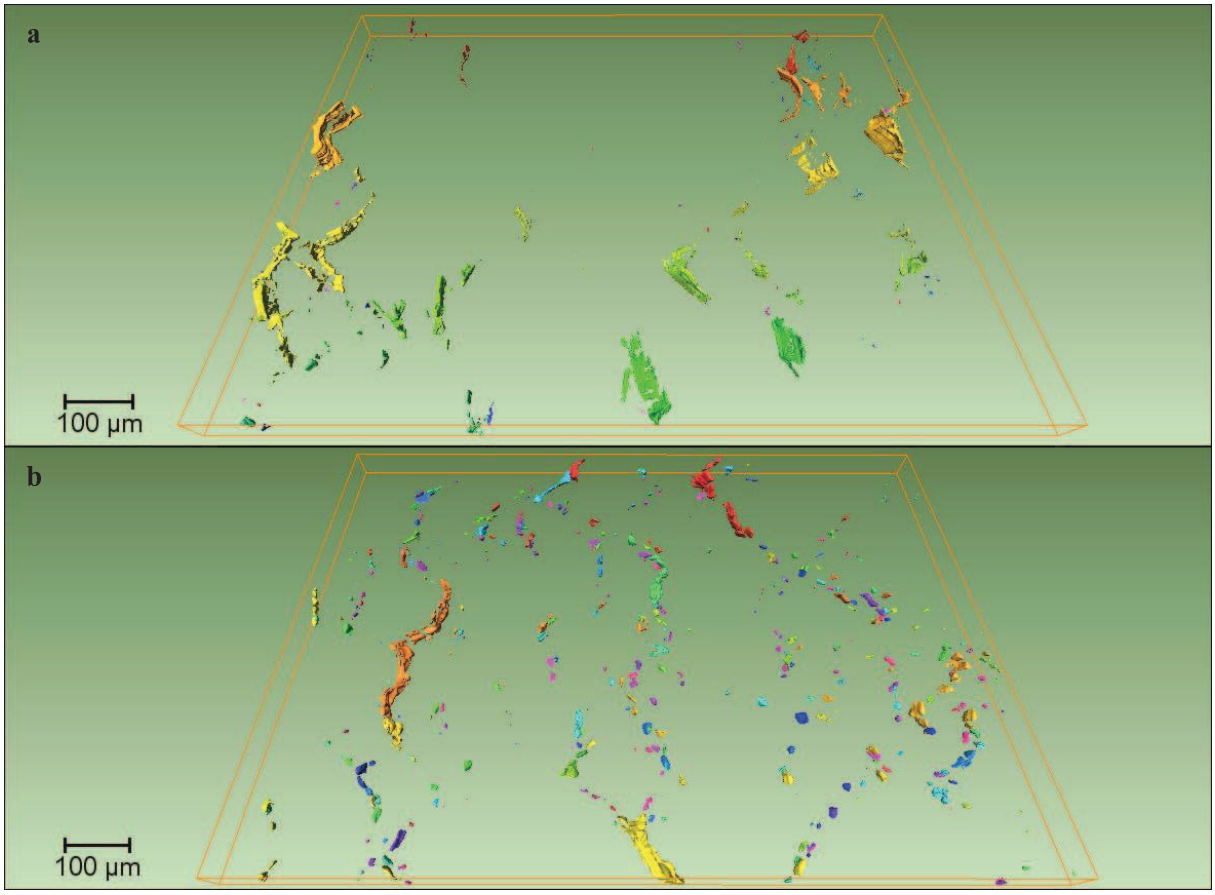

Figure VI-4 Three-dimensional visualization of reconstructed creep voids inside samples deformed at (a) 573 K, 80 MPa (T2 conditions) (b) 773 K, 10 MPa (T1 conditions)

VI.3.1 Quantification of creep void shape

A fast quantification of creep voids can be performed based on two parameters, the volume and the equivalent diameter. For a given void the equivalent diameter represents the diameter of the spherical void with the same volume. Figure VI-5 shows the probability density of the volume and equivalent diameter of the creep voids at each creep condition. For the equivalent diameters, 2D data are obtained from one section and the 3D ones from the reconstructed volume.

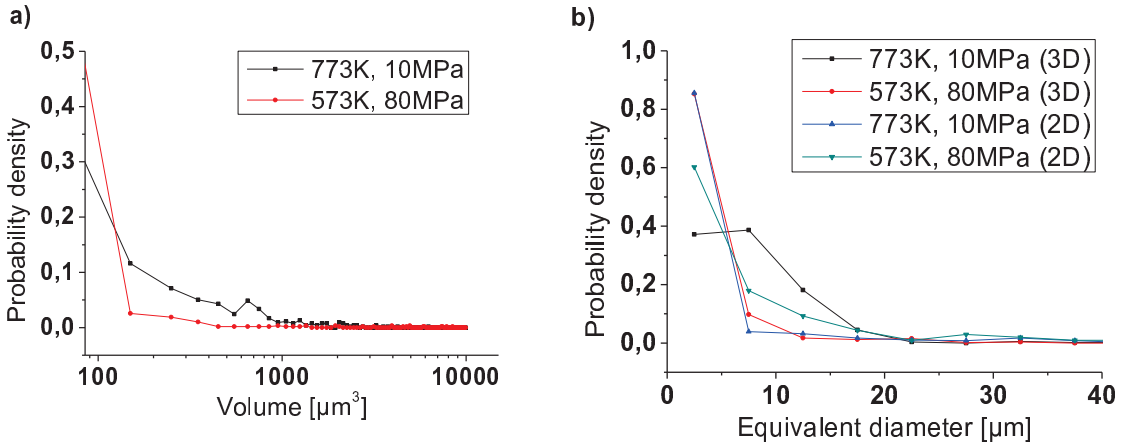

Figure VI-5 Size distribution of creep voids' (a) volume and (b) equivalent diameter

It can be observed that 2D and 3D size void size distributions are not equivalent. Also that the voids present in the sample deformed at higher temperature and lower stress (T1) are bigger, which might be related to the longer creep time of this sample. In practice the voids can be rarely approximated by spheres, which requires a more accurate description of their shapes.

The observations indicate that cavity shape depends on testing conditions, varying from an almost spherical to a crack like morphology for larger cavities. Using synchrotron microtomography, Isaac et al. [68] categorized the pores as followings: spherical, ellipsoidal, rod shape and complex cavities. They have shown that the cavities can be reasonably approximated by general ellipsoids having the same moments of inertia (except for the complex ones). Shape estimation was done according to the following parameters:

$$Elongation = \frac{L}{1/2(B+T)} \qquad \text{Equation VI-1}$$

$$Flatness = \frac{B}{T} \qquad \text{Equation VI-2}$$

where L, B and T are the major, intermediate, and minor ellipsoid semi-axes respectively. The elongation and flatness provide a more quantitative approach to pore shape classification. Since these descriptors cannot provide any information on the complexity of the voids, this parameter will be described as the deviation of the shape of a cavity from its equivalent ellipsoid. The procedure as described by Isaac et al. [68] was implemented by Dzieciol [79] in Matlab and was applied to the voids found in the present reconstructions. Based on these works we describe the shape of a pore as the following (Table VI-1).

Pore shape	Elongation (2L/(B+T))	Flatness(B/T)	Complexity
Sphere	≤ 1.3	≤ 1.3	≤ 0.75
Ellipsoid	1.3 < 2L/(B+T)) ≤ 3	Or > 1.3 if 2L/(B+T) ≤ 1.3	≤ 0.75
Rod	> 3	-	≤ 0.75
Complex	-	-	> 0.75

Table VI-1 Cavity shape descriptors: L, B and T are the major, medium and minor ellipsoid semi-axes of the equivalent ellipsoid, respectively [68]

The shape descriptors were calculated for all the pores of both samples. The distribution of the *elongation* vs. *flatness* is in Figure VI-6-a. It can be observed that there are more pores with a high elongation factor in sample deformed at 573 K, 80 MPa.

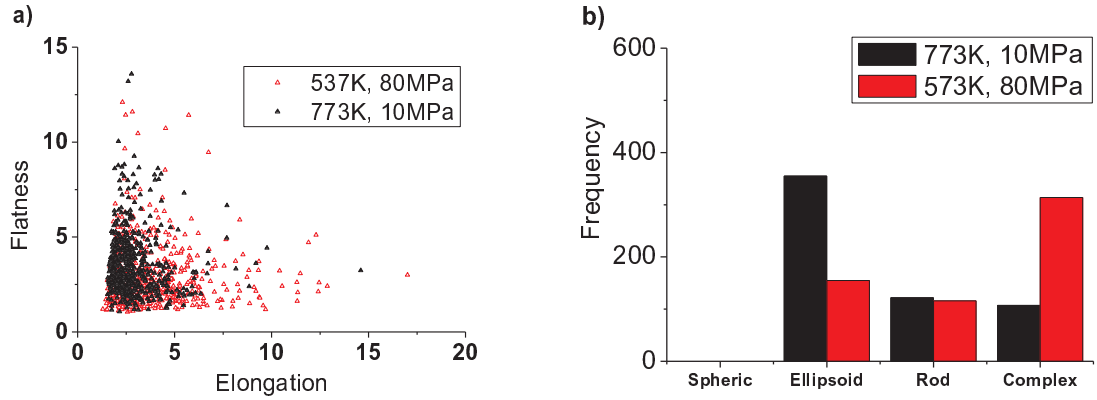

Figure VI-6 (a) Relation between shape descriptors *flatness* and *elongation* (b) voids categorized in different classes

Based on these shape descriptors the distribution of pores in different classes is shown in Figure VI-5-b. It is remarkable that the two deformation conditions lead to very different void shapes. The sample deformed at low stress (10 MPa) contains more ellipsoid like voids, while the one deformed at high stress (80 MPa) has more pores of complex type. This might be caused by coalescence, but also by dislocation slip which is dominant at high stress.

VI.4 3D grain properties

VI.4.1 Grain volumes

The procedure for the reconstruction of the granular structure was described in the section V.3.3. The reconstructed 3D structure of the two samples is shown in Figure VI-7.

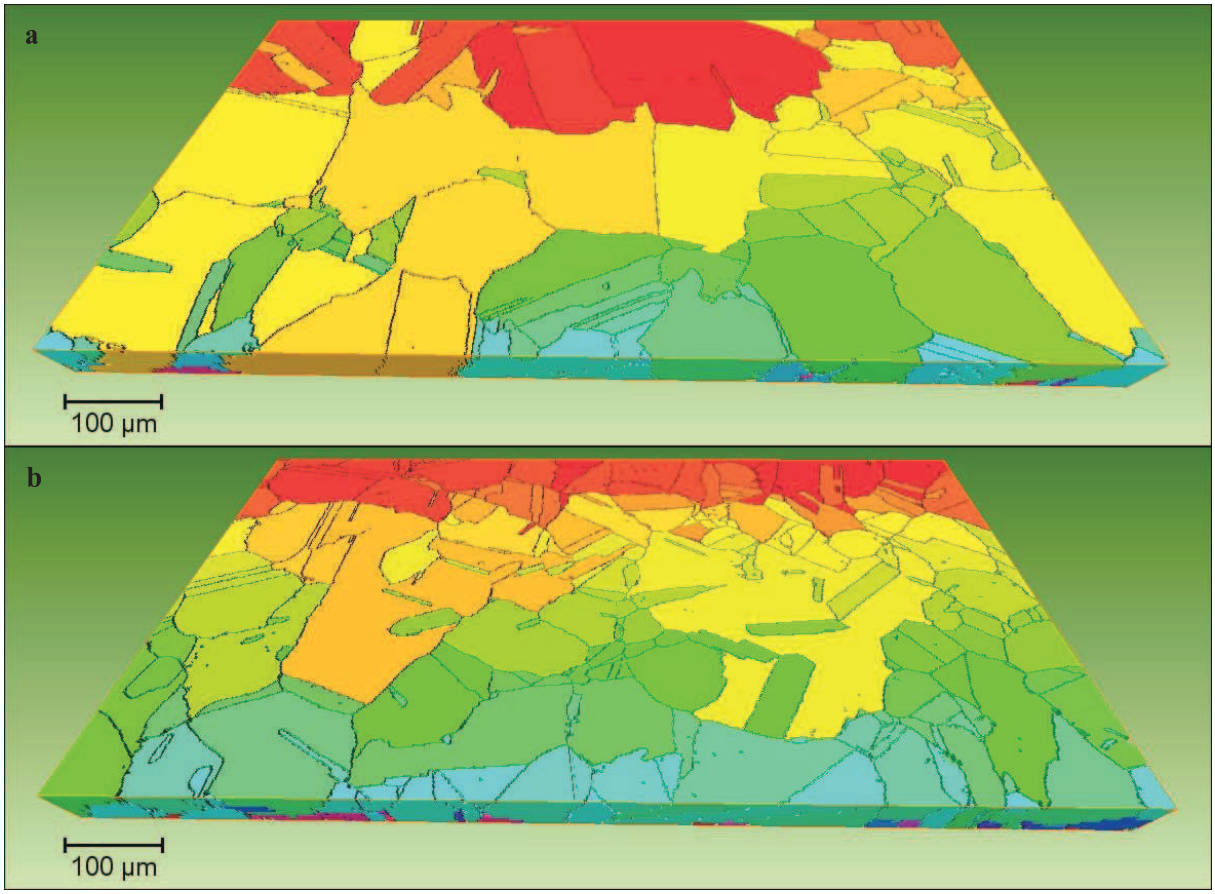

Figure VI-7 Three-dimensional visualization of granular texture reconstructed for samples deformed at (a) 573 K, 80 MPa (T2) (b) 773 K, 10 MPa (T1)

We could identify 364 grains in the sample deformed at 573 K and 705 grains at the sample obtained at 773 K. Despite the fact that many of these grains are not completely reconstructed and the depth of 40 µm permits to see just a part of larger grains, they still can be quantified to extract a more accurate grain size statistics.

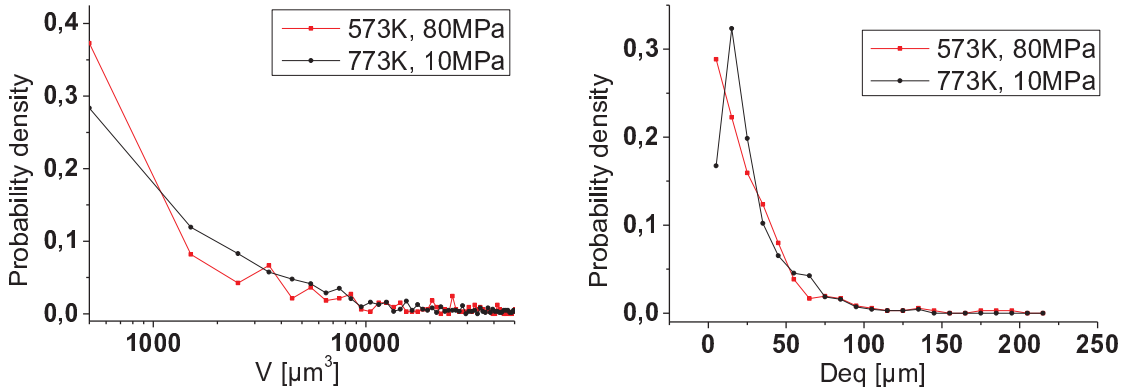

Figure VI-8 Size distribution of reconstructed grains (a) volume and (b) equivalent diameter

Figure VI-8 shows the distribution of the volume of the grains and their sphere equivalent diameter. The size distribution curve of the grains found in the two samples can be considered almost identical. Similarly, the statistical analysis that both grain populations (Table VI-2) indicate that the two samples have the same mean grain size and nearly the same standard deviation. The mean grain size is different from the value of about 40 µm obtained from 2D sections. This may be caused by the insufficient thickness of the analyzed volume.

	Min (D_{eq}) [µm]	Max (D_{eq}) [µm]	Mean (D_{eq}) [µm]	Standard deviation [µm]
573K, 80MPa	3.1	192	27.9	27.6
773K, 10MPa	4.2	138	27.5	22.1

Table VI-2 Comparison of minimum, maximum and mean equivalent diameter of the grains obtained after reconstruction

VI.4.2 Crystallographic orientation

The novel property of the grains is related to their crystallography. Based on EBSD measurements the orientation, the orientation spread and the mostly stressed slip system related to the maximum Schmid factor could be identified.

VI.4.2.1 Mean orientation

To quantify this we have used the ORILIB code developed by Quey [84]. Knowing the mean orientation of each layer, the orientation of a 3D grain was identified as the mean orientation of the of the same grain in all layers. This data will be used to calculate the disorientation/misorientation of neighbor grains. We are aware that is not very accurate but no conclusions will be drawn which require an absolute orientation accuracy better than 3°-5°.

VI.4.2.2 Mean orientation spread

For each grain a mean disorientation parameter was also calculated, which was considered to describe the subdivision of the grain into sub-grains and the content of geometrically necessary dislocations (GNDs). This parameter is the *mean orientation spread*, which represents the mean value of the disorientation of each pixel with regard to the grain average orientation. As grain subdivision takes place during creep, the mean orientation spread is expected to increase with deformation. As explained before (section V.3.3.2, the data alignment procedure), the orientation information can not be accurately matched due to the slightly different positioning of the sample on the microscope stage. So, the orientation calculations are less coherent when the layers are combined. In order to reduce this effect the mean orientation spread was first calculated for each layer separately with regard to the mean orientation of the grain in that layer. Then all these

angles were collected and the three dimensional parameter is considered as the mean value over the layers.

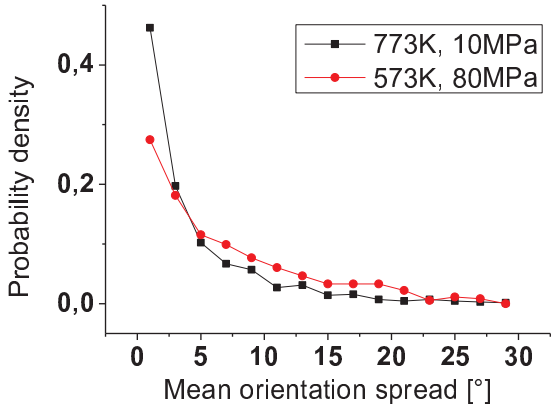

Figure VI-9 Distribution of the mean orientation spread of all the grains in the two analyzed samples

Figure VI-9 shows that the sample deformed at 573 K has more grains with higher value of the orientation spread, which indicates a more heterogeneous intra-granular structure and a higher density of geometrically necessary dislocations (GNDs). At the same time the higher deformation temperature (773 K) and much longer creep time of the T1 sample can lead to more efficient dislocation recovery processes and consequently to a smaller mean orientation spread.

VI.4.2.3 Slip system

The slip systems of a f.c.c crystal were defined in section III.3.4.3 along with the calculation procedure of the Schmid factor. This procedure was then applied to the three dimensional mean orientation of the grains for all the twelve possible slip systems in copper. The active slip system was identified as the system with maximum Schmid factor. The distribution of the maximum Schmid factors and the corresponding slip systems are shown in Figure VI-10. From the point of view of slip activity the two samples can be considered very similar.

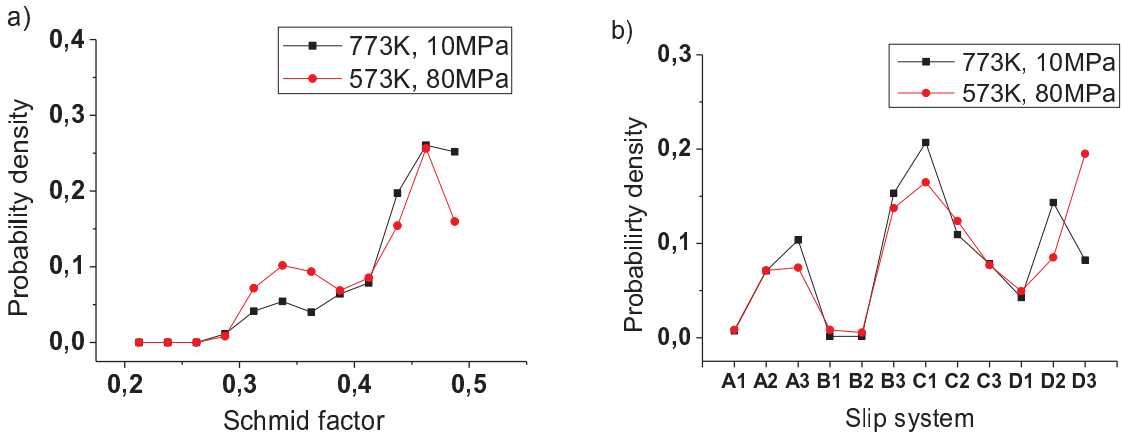

Figure VI-10 Distributions of (a) the maximum Schmid factor and (b) the corresponding slip systems in grains of the analyzed samples

VI.4.3 3D grain boundaries

VI.4.3.1 Grain boundary type detection

Creep voids are always located at the grain boundaries, which implies an analysis according the grain boundary type. Grain boundaries are categorized based on the number of neighbor grains such as: simple, triple and quadruple boundaries shared between two, three and four grains, respectively. Higher order boundaries are also possible to detect, but since their fraction is usually very low they will not be subject of the present study.

GBs are interfaces where crystals of different orientations meet. From an image analysis point of view there are different ways to identify a GB. One of the simplest ways is to attribute them an identifier (ID) code and present them with a specific grey level. As described in section V.3.3.3, a 2D grain structure is stored in a 16 bit image where the zero value indicates the grain boundaries. An example is given in the schematic grain map shown in Figure VI-11. Using a 3x3 filter that runs over the grain boundary pixels and counts the number of different grains within its 8 neighbors a simple method is set up for detecting the grain boundary type. Attributing the number of neighbor grains to each GB pixel a specific image indicating the GB type can be obtained (Figure VI-11-right). The simple and triple boundaries are indicated by the numbers 2 and 3, respectively.

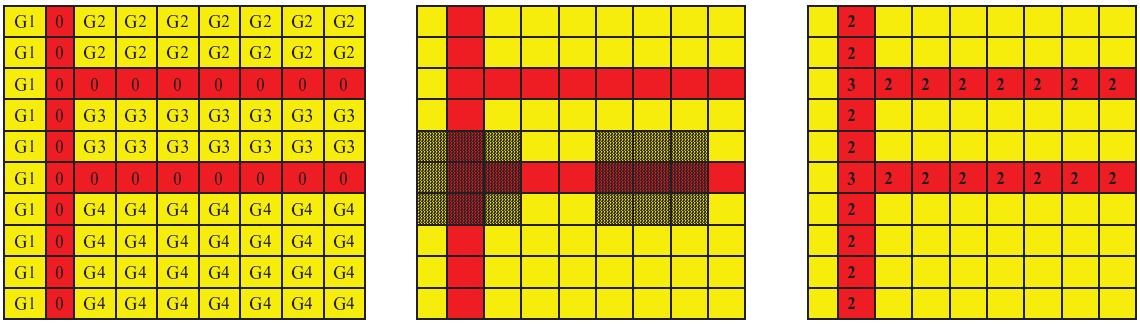

Figure VI-11 Schematic drawing of (Left) the initial grain map with 4 grains in yellow each with a specific ID. Grain boundaries in red (middle) with the 8 neighbor filters running over all of their pixels and (Right) GB type map where the number 2 presents simple and 3 the triple GBs.

To identify the GB type in the reconstructed volumes a slightly different scheme was used. The pixels of each grain were marked by a 3 digit number. While scanning the grain boundaries by the filter a unique neighbor ID to each boundary pixel was assigned by writing the IDs of the grain pixels one near the other. For example, the boundary between grains G1 (ID=112) and G2 (ID=289) is named 112289. This number is unique and all the pixels sharing two grains will have an ID made up of 6 digits. A triple boundary pixel gets a 9 digit ID. They should then be stored on a 32 bit image. After finishing the filtering procedure the GB IDs can be replaced by smaller numerical values.

The GB identification procedure was explained for a two dimensional case. It should be mentioned that the entry images are already registered via the manual registering procedure as explained in section V.3.3.4. Running a two-dimensional filter on an already registered grain map leads already to valuable results for the three-dimensional identification. For example, a pixel on the grain boundary between grains G1 and G2 in layer1 (placed at (x_1, y_1, l_1)), indexed as boundary number 112289 is indexed with the same number in the next layer, too (but at (x_2, y_2, l_2)). Connecting the coordinates of these two voxels links the grain boundary from one layer to the other. Collecting the coordinates of the voxels belonging to the same grain boundary the simple grain boundary voxels should be connected by planes and the triple boundaries by line segments.

VI.4.3.2 Quantification

Grain boundaries were categorized to three groups: Simple, Triple and Quadruple boundaries. The quantification results for the two samples and are presented in Table VI-3.

	573K, 80MPa	773K, 10MPa
Simple boundaries	1180	2723
Triple boundaries	971	2397
Quadruple boundaries	13	44

Table VI-3 Total number of boundaries in each category for both samples

From the point of view of creep damage it is believed that triple junctions play an important role due to the possible concentration of the applied stress around them [7]. In the first step their presence in the consecutive layers was examined. For evaluation purposes the triple GBs identified only on one EBSD layer were not taken into account. Their amount was, however, high of about 45.9% and 56.6% of the total number of triple GBs in the sample deformed at 573 K and 773 K, respectively. After identification the length of triple boundaries was calculated as the sum of the lengths between the coordinates of the same boundary in the consecutive layers. The results are shown in Figure VI-12.

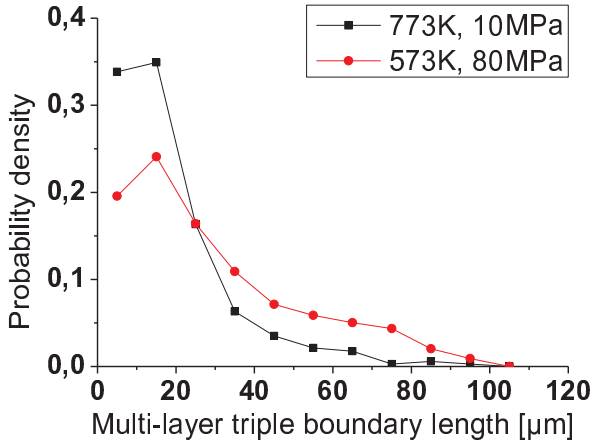

Figure VI-12 Distribution of the length of "multi-layer" triple grain boundaries for both samples

This shows that the triple boundaries present in the sample deformed at 573 K are longer than those of the sample deformed at 773 K. Dividing the total number of triple GB voids by the total length of triple GBs the probability to find a void per unit length of triple GB is obtained. These values are $0.4 \cdot 10^{-3}$ μm^{-1} and $1.3 \cdot 10^{-3}$ μm^{-1} respectively for the samples deformed at 573 K and 773 K. According to this triple boundary pores are more probable in samples deformed at lower stresses.

VI.4.3.3 Grain boundary visualization

Knowing the coordinate of the triple grain boundary sections in all layers it becomes possible to visualize them.

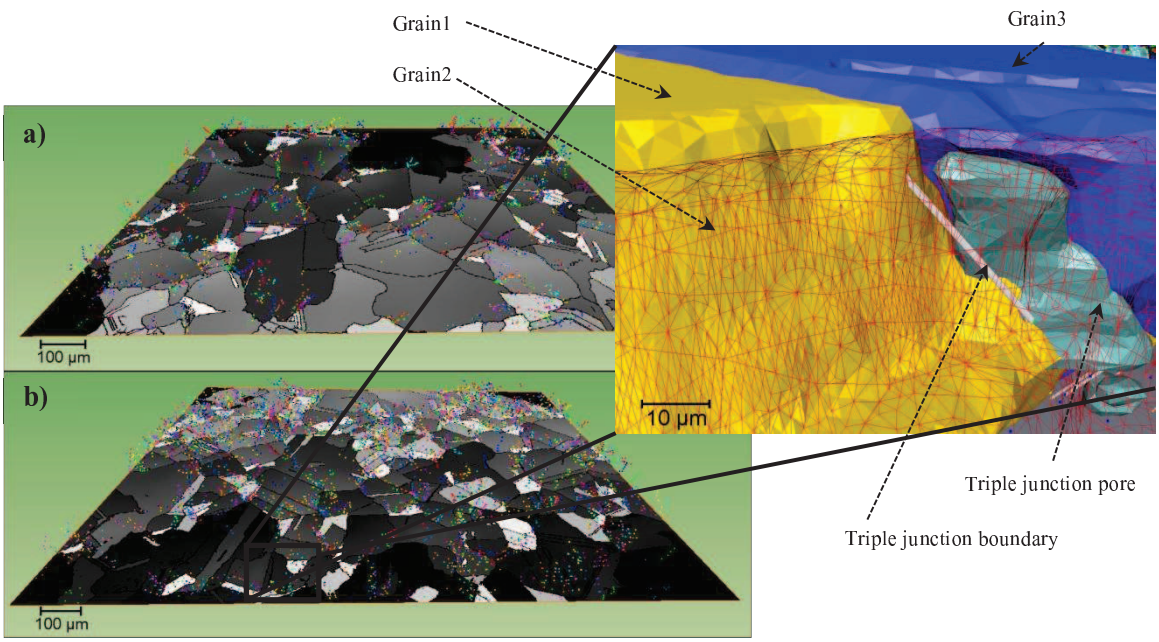

Figure VI-13 Visualization of a 2D layer of grains with corresponding segmented triple grain boundaries at (a) 573 K, 80 MPa and (b) 773 K, 10 MPa - points forming the same boundary are labeled with the same color

Figure VI-13 shows a point cloud of the triple boundaries, where the points with the same color represent the same grain boundary. The inset shows a triple junction at higher magnification. This boundary contains also a pore.

VI.5 Correlation between microstructure and grain crystallography

In this section the creep pores are categorized based on their position with regard to grain boundaries and subsequently quantified. Next, the probability of finding a pore at different grain boundary types will be evaluated and compared for both samples. Finally, the effect of local crystallography on creep damage will be discussed.

VI.5.1 Strategy of correlation

In order to correlate damage to local crystallography the separately reconstructed volumes containing the voids and the grains should be linked. To do so, the voxels of each pore were extracted and stored in a list. Then in the corrected grain map (obtained in section V.3.3.3) the grain Id's superimposed with voids are also extracted. Sorting the unique grain ID's gives the list of the neighbor grains surrounding the pore. The procedure is shown schematically in Figure VI-14. It shows an example of a pore being in contact with three grains and indexed as a triple junction pore.

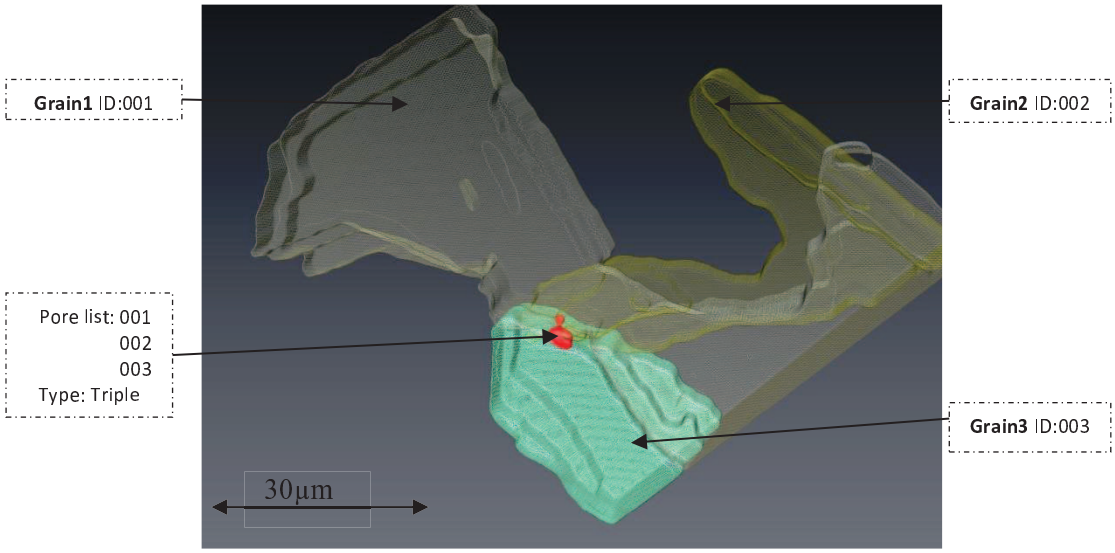

Figure VI-14 Three dimensional reconstruction of a triple junction pore situated between three different grains - sample deformed at 573K, 80MPa

Pores can now be categorized based on the number of surrounding grains. It should be noted that there is a considerable number of voids not be categorized by this method (about 40% of the pores). These voids are located between two consecutive EBSD slices and are the result of a much smaller step size used for taking the SEM images. Software development is under way to take these into account, too.

VI.5.2 Pore types

VI.5.2.1 Pore type quantification

As presented on Figure VI-15, there are less triple boundary pores in both samples than the simple boundary pores. The distribution of the pore size of different categories show, however, that despite their lower population triple boundary voids are larger in both samples.

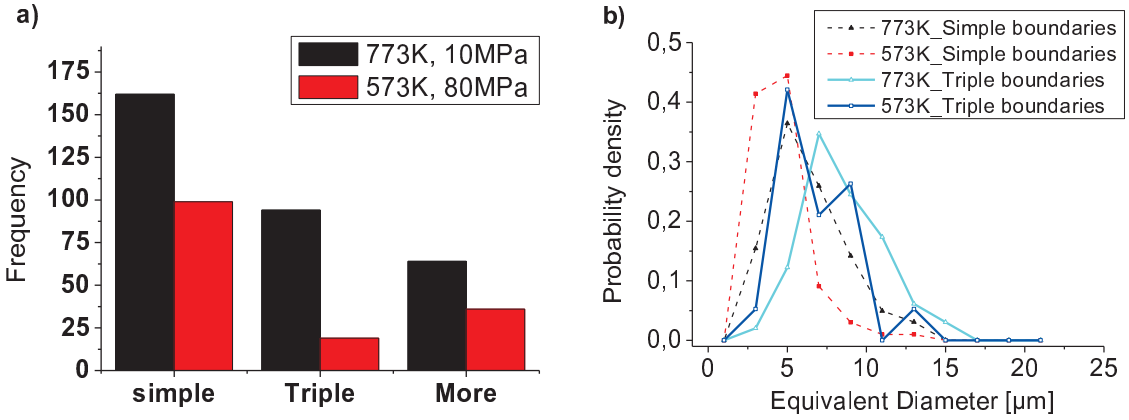

Figure VI-15 (a) Number of different type of creep voids and (b) their size distribution for both samples

Due to this the volume fractions of triple boundary pores become more important than those of simple boundary pores. According to Table VI-4 the volume fraction of triple-boundary pores in the sample deformed at 773 K is by 26% higher than that of simple-boundary pores. The situation is reversed for the sample deformed at 573K where small pores are more numerous. In this

sample the volume fraction of simple boundary pores is by 78% more than that of triple boundary pores.

	Volume of Simple boundary pores/Analysis volume [$\mu m^3/\mu m^3$]	Volume of Triple boundary pores/Analysis volume [$\mu m^3/\mu m^3$]
773K, 10MPa	0.0979 %	0.1238 %
573K, 80MPa	0.0276 %	0.0155 %

Table VI-4 comparison of volume fraction of simple and triple boundary creep voids for both samples

Figure VI-16 visualizes the distribution of creep voids in the two analyzed samples. Damage is more homogeneously distributed in the sample deformed at 773 K.

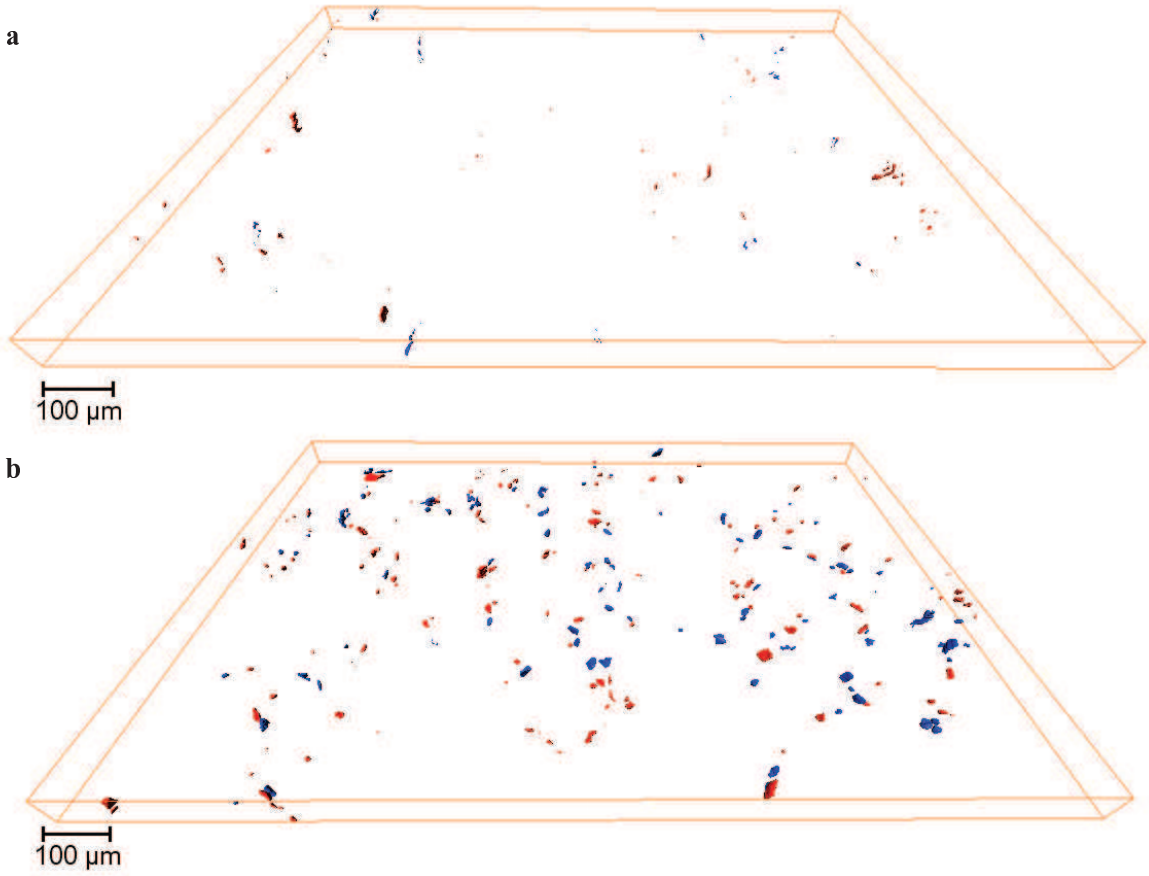

Figure VI-16 Visualization of simple (Red) and triple boundary pores (Blue) for samples deformed at (a) 573 K, 80 MPa and (b) 773 K, 10 MPa

VI.5.3 Probability of different creep void types

After classifying the GBs and voids we can perform the desired statistical analysis regarding the correlation between damage and crystallography. The probability of a creep void on a given boundary type can be calculated as the ratio between the number of damaged grain boundaries of a given type over the total number of grain boundaries of that type. The results for the two samples are presented in Table VI-5.

	573K, 80MPa			773K, 10MPa		
	Simple	Triple	Quadruple	Simple	Triple	Quadruple
Total number of boundaries	1180	971	13	2723	2397	44
Boundaries containing a pore	99	19	10	162	98	40
Occupation ratio [%]	8.3	1.9	77	5.9	4.0	91

Table VI-5 Probability of pore location at simple, triple and quadruple GBs

It can be observed that despite the different number of grain boundaries found in the two samples; both samples show a higher occupation probability for simple boundaries than for triple boundaries. It is interesting to compare the proportion of voids for the two samples as a function of void type. Finding a pore at a simple GB is more probable in the sample deformed at higher stress and the opposite is true for triple boundary voids. Remarkable is in both cases the extremely high probability of damaged quadruple GBs, which reaches nearly 100% for the sample deformed at high temperature and low stress.

VI.5.4 Effect of local crystallography on creep damage

In this section the creep damage of the two samples will be correlated to the crystallographic orientation of surrounding grains. We suggest therefore to analyze the possible influence of:

- The relative disorientation
- The mean orientation spread, and
- The Schmid factor of the neighbor grains.

The different procedures are indicated schematically in Figure VI-17. Disorientation is calculated between each two grains sharing a simple boundary pore. For triple boundary pores, disorientation is calculated between each three pair of grains.

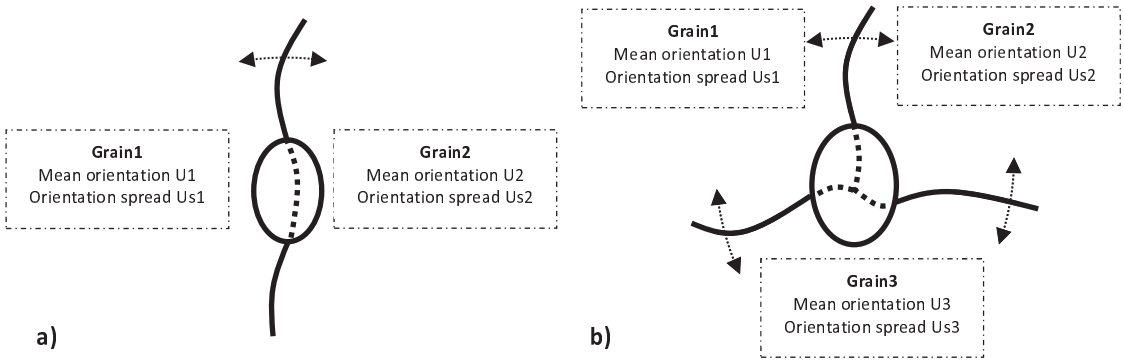

Figure VI-17 Local crystallographic properties around a (a) simple boundary pore or a (b) triple boundary pore

VI.5.4.1 Effect of grain orientation

The distributions of disorientations are presented in Figure VI-18 for sample deformed at 573 K and in Figure VI-19 for sample deformed at 773 K.

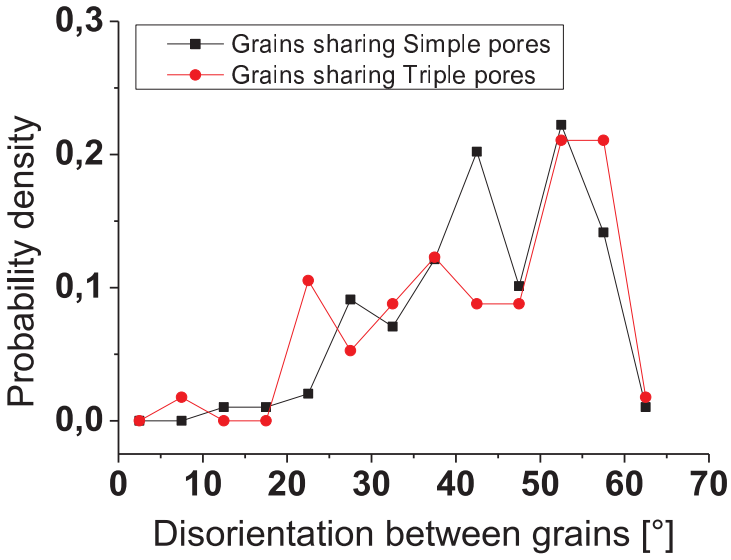

Figure VI-18 Disorientation distribution between grains sharing simple or triple boundary pores - sample deformed at 573 K

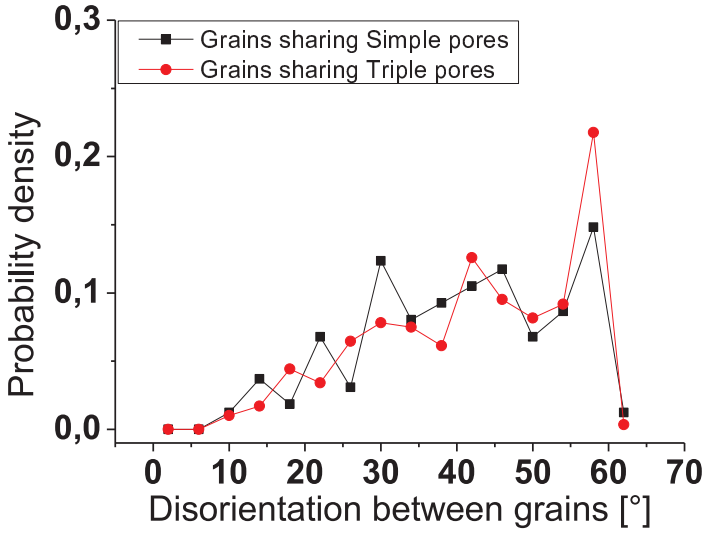

Figure VI-19 Disorientation distribution between grains sharing simple or triple boundary pores - sample deformed at 773 K

It can be observed the distributions of disorientations are close the random distribution of orientations in both samples already present in the initial non-damaged state. This means that there is no special disorientation between neighbor grains that has special influence on pore location.

VI.5.4.2 Effect of grain's mean orientation spread

A mean value of the orientation spread can be calculated for each grain of the deformed samples. We distinguish again two cases, the distribution for all the grains and the distribution for

grains that have a neighbor pore. The results for the two cases are presented in Figure VI-20 and Figure VI-21 for the samples deformed at 573 K and 773 K, respectively.

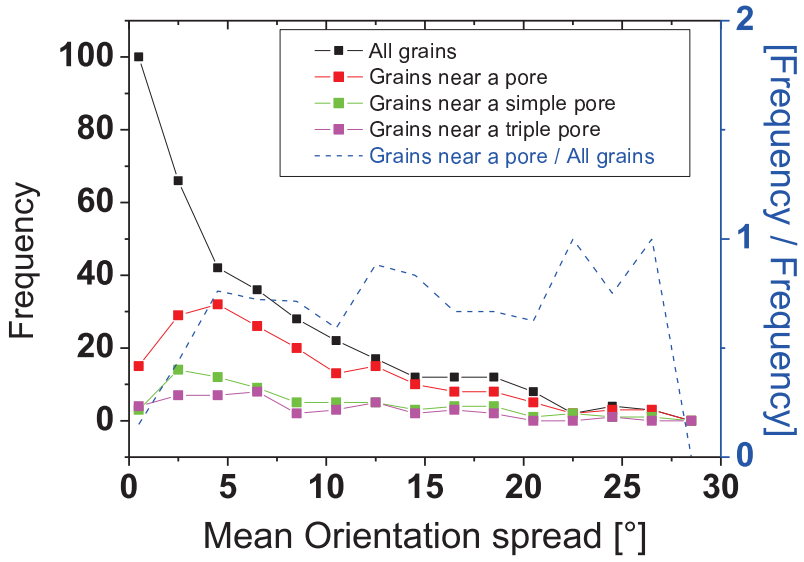

Figure VI-20 Orientation spread distribution of all the grains and for grains sharing simple or triple boundary pores - sample deformed at 573 K

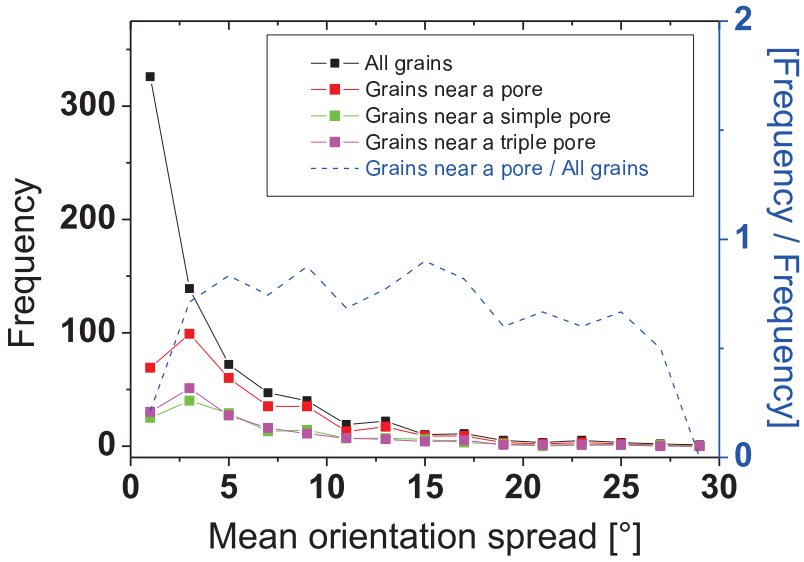

Figure VI-21 Orientation spread distribution of all the grains and for grains sharing simple or triple boundary pores- sample deformed at 773 K

For both samples the majority of grains situated near pores have a mean orientation spread larger than 3-5°. The grains with mean orientation spread below this value have a smaller probability to be located near the pores. Remarkable is however, the insensitivity of pore location to higher values of this parameter. Slip complexity and the GND density inside the grains does not correlate with the presence of voids at their GBs.

VI.5.4.3 Effect of grain slip system

The distribution of the maximum Schmid factor of all the grains are compared with those of grains having a pore as neighbor and are presented in Figure VI-22 and Figure VI-23, respectively for the samples deformed at 573 K and 773 K.

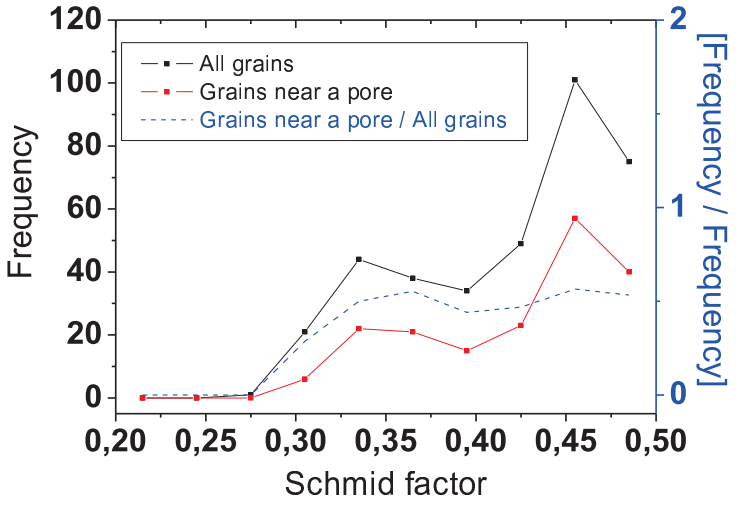

Figure VI-22 Distribution of Schmid factors for grain boundaries sharing a simple or triple boundary pore - sample deformed at 573 K

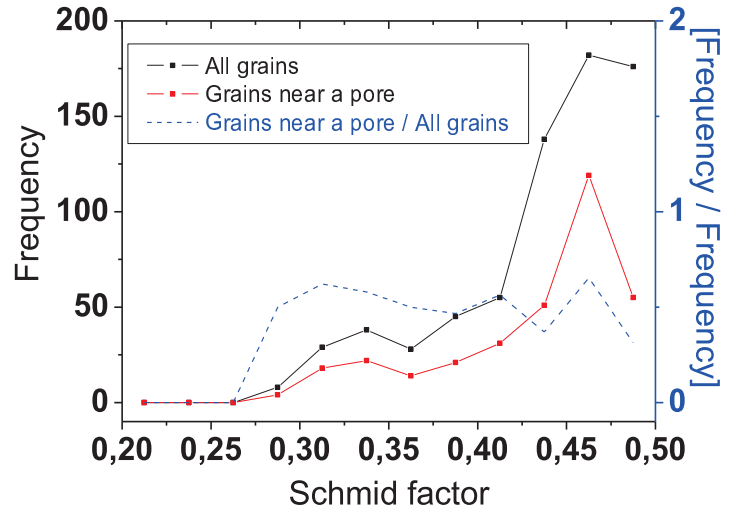

Figure VI-23 Distribution of Schmid factors for grain boundaries sharing a simple or triple boundary pore - sample deformed at 773 K

It can be observed that for both samples that the Schmid factor of grains having a pore in their neighborhood has a very similar distribution as the distribution for all the grains. This indicates damage nucleation/growth does not depend on any particular slip system, a results that is equivalent with insensitivity of void location to the absolute orientation of the grains.

A summary of all results obtained on both samples are presented in the Table VI-6.

Creep	**Creep conditions**	573 K, 80 MPa (T2)	773 K, 10 MPa (T1)
	Test abortion	After 6h (creep stage III)	After 150h (creep stage III)
	Steady state deformation rate	2E-06 [1/s]	2E-07 [1/s]
	Growth mechanism of voids	Plasticity controlled growth	Diffusion controlled growth
Creep voids	**Number of voids** (V>30voxels, non-flat)	584	535
	Void distribution	Highly inhomogeneous	More homogeneous
	Void shape description	Complex pores - highly elongated	Ellipsoidal pores - less elongated
	Damage state due to void shape	Void coalescence	Void growth
Texture	**Number of grains - fraction with a pore in its vicinity**	364 - 51,9%	705 - 50,6%
	Mean grain size (D_{eq}) [µm]	27.88	27.84
	Grain size distribution	Identical as T1	Identical as T2
	Orientation spread distribution	Majority for higher orientation spreads	Majority for lower orientation spreads
	Schmid factor distribution	Identical as T1	Identical as T2
	Dominant active slip system	D3 (-111)[1-10]	C1 (1-11)[110]
	Pole figure max intensity	11,6	9,02
GBs	**Number of simple GB**	1180	2723
	Number of triple GB	971	2394
	Simple GB occupation ratio	8.3%	5.9%
	Triple GB occupation ratio	1.9%	4.0%
	Distribution of triple GB length	Majority for longer boundaries	Majority for shorter boundaries
Void - Crystal	**Number of simple GB voids**	99	162
	Number of triple GB voids	19	98
	Probability of triple GB void per unit length of triple GB [μm^{-1}]	0.39E-03	1.30E-03
	Volume fraction of simple GB voids	0.0276 %	0.0979 %
	Volume fraction of triple GB voids	0.0155 %	0.1238 %
	Dominant void type (Number)	Simple GB voids	Simple GB voids
	Dominant void type (volume)	Simple GB voids	Triple GB voids
	Void size distribution	Majority of bigger pores are at triple GBs; Majority of smaller ones are at simple GBs	Majority of bigger pores are at triple GBs, Majority of smaller ones are at simple GBs
	Void growth conclusion	Simple GB voids grow faster	Triple GB voids grow faster
	Distribution of disorientation	Grains with a neighbor pore : Random	Grains with a neighbor pore : Random
	Distribution of orientation spread	Orientation spread >3° for majority of grains have a neighbor pore	Orientation spread >3° for majority of grains have a neighbor pore
	Distribution of Schmid factor	Similar distribution for all the grains and grains having a neighbor pore	Similar distribution for all the grains and grains having a neighbor pore

Table VI-6 Summary of comparison between results obtained of samples at different creep conditions

VI.6 Conclusion to serial sectioning

a) Particularity of the method:

Chapter V presented the conventional serial sectioning procedure, its strong points and its problems. To be able to present comparable results to those obtained by synchrotron X-ray tomography, the conventional serial sectioning method was modified. Nearly all the steps were personalized to assure accurate results.

The experimental procedure was improved by embedding the sample in a polymer resin, which stabilizes the sample, equalizes the charge distribution and eases the manipulation during the long sectioning procedure. Polishing was done with the CMP method, which insures the material removal homogeneously at desired low rates. This increases the reconstruction resolution. The material removal was checked by an optical profilometer. The sections no longer need to be parallel as the developed local height technique combined with the reconstruction methods can produce three- dimensional visualization of the surface components generated from non-parallel sections.

A personalized computation technique was used to align data of different layers and obtained by different detectors. This gave two different reconstruction volumes: one for the creep voids and the second one for the surrounding grains. The alignment technique superimposed these two volumes in a way that damaged zones of the sample can be correlated to the surrounding crystallography data.

b) Application on creep voids

The 3D analysis revealed important differences between the two investigated samples, but also between the repartition of voids on different GB types within one specimen. These differences are considered to be related to the different nucleation and growth mechanisms of voids. We point out first that the number and the probability to find a void per unit length of triple boundary increases with increasing temperature and with decreasing creep stress. This behavior is similar to the change in the contribution of GBS to the total creep strain rate [106], and suggests that GBS should be responsible for void nucleation at triple junctions. The fact that almost all quadruple GBs are damaged confirms the importance of GBS for void nucleation.

The second result concerns the higher volume fraction of triple boundary voids compared to those at simple boundaries, which should be related to the mechanisms of void growth. Since triple junction pores are in contact with more GBs than simple GB voids, indeed creep plasticity, GB diffusion and GBS should be more effective in this case.

More simple GB voids are formed at higher stresses, which suggests an increasing contribution of plastic slip for their nucleation.

Remarkable is the insensitivity of creep damage on the crystallographic orientation of grains adjacent to voids as evidenced by the nearly identical distribution of Schmid factors in the two samples. Similarly, the disorientation between void neighbor grains has no significant influence on damage. No real correlation could be found between the presence of a void at the GB and the average GND density within the neighbor grains.

VII Conclusions and perspectives

Present work has tried to clarify some aspects of creep damage by using two advanced characterization techniques. In situ tomography is an excellent method for the investigation of specimens undergoing deformation and allows a good characterization of the kinematics of creep damage. The rapidity of this technique (3 minutes per scan at ESRF ID15) permitted a four dimensional analysis of creep deformation. Damage was identified as the area fraction of voids present on each tomography slice perpendicular to creep axis. The image correlation algorithm, permitted to follow the evolution of damage in a given slice over all reconstructed volumes. The local and global evolution of cavities area fraction was checked against the Cocks and Ashby model. It was found that the model overestimates creep lifetime and underestimates damage development. The importance of the initial damage heterogeneity and the role of damage localization were also emphasized. It was found that the amplitude of the largest damage fluctuation increases parabolically as a function of cavities mean area fraction.

It is known that creep cavities nucleate and grow at grain boundaries. Since power law creep is related to the glide and climb of dislocations it was assumed that crystallographic orientation of grains might play a significant role in damage nucleation and evolution. Despite its powerful capacities, conventional tomography does not provide any information on local crystallography. The deformed state of the creep deformed samples does not authorize the use of modern tomography techniques like DCT or 3DXRD. Therefore it was decided the development of a destructive 3D reconstruction method capable to identify the granular structure of the damaged crystal and to associate the voids to different grain boundary types.

An improved serial sectioning method based on surface profilometry was developed, which allows the accurate measurement of the removed local material thickness. The initial goal was the removal of 1 µm per cycle up to a total thickness of 40 µm. The samples were additionally imaged by SEM and by EBSD. Characterization was performed with a large field of view (1.2 x 0.8 mm^2) on two samples deformed under very different temperature and stress conditions, when plastic creep (lower temperature and high stress) and grain boundary diffusion (high temperature and low stress) can be considered as the main mechanisms of cavity growth. The 3D reconstructions enabled identifying the creep voids and the grains of the polycrystal.

Effect of crystal orientation on creep damage was analyzed based on three factors:

- Mean orientation spread: It was shown for both samples that grains having a neighbor pore have a mean orientation spread of more than 3°, however, only 60-80% of such grains have a pore in their neighborhood.
- Highest Schmid factor: The distribution of the highest Schmid factor showed an identical tendency for both samples, this parameter has no influence on damage.
- Disorientation of void neighbor grains: Random distribution of disorientation was observed for grains sharing a simple or triple GB creep void. It means that disorientation of neighbor grains does not influence creep damage.
- The higher fraction of triple GB pores in the sample deformed under T1 conditions is attributed to mechanism of grain boundary sliding, more probable in this sample as the applied temperature is higher and the stress is much lower than for T2 conditions. This result is in good agreement with literature data on GBS [106].

- Topological aspects seems to be more important than crystallographic ones. Voids grow faster at triple boundaries than at simple ones.

As perspectives the following suggestions are made:

- From an experimental point of view the material removal procedure (CMP) is quite reliable, but the chemical aspect was not enough studied in this work. Colloidal silica slurry can be combined with additional chemical components to increase the removal rate and decrease the polishing time. This will improve the efficiency of the method.
- It is suggested that the influence of crystallography is a more local effect than a global one. The scale, on which we performed our analysis, is suitable to extract statistical results. We propose 3D high resolution (angular and spatial) EBSD acquisitions using static FIB-SEM ion beam milling on single cavities.
- It can be also interesting to see the relationship of any extracted data from this method and the single void growth rate obtained by in-situ μCT. It would be interesting to determine the growth rate of voids located at simple GBs and at triple junctions.

References[1]

[1] "Library of failures," *Surescreen*, 2013. [Online]. Available: http://www.surescreen.com/scientifics/library-of-failures.php.

[2] F. C. Monkman and N. J. Grant, "Empirical relation between rupture life and minimum creep rate in creep-rupture tests," *Proc. ASTM*, vol. 56, pp. 593–620, 1956.

[3] J. D. Meakin, "The Creep of Face-centered Cubic Metals with Special Reference to Copper," *Acta Metall.*, vol. 7, pp. 614–627, 1959.

[4] H. E. Evans, *Mechanisms of Creep Fracture*. Elsevier Applied Science Publishers, London, 1984.

[5] A. Needleman and J. . Rice, "Plastic creep flow effects in the diffusive cavitation of grain boundaries," *Acta Metall.*, vol. 28, no. 10, pp. 1315–1332, Oct. 1980.

[6] A. C. F. Cocks and M. F. Ashby, "On creep fracture by void growth," *Prog. Mater. Sci.*, vol. 27, no. 3–4, pp. 189–244, Jan. 1982.

[7] H. Riedel, "Fracture at high temperatures," in in *Materials Research and Engineering*, Springer, 1987, p. 418.

[8] M. E. Kassner and M. T. Perez-Prado, *Fundamentals of Creep in Metals and Alloys*, Elsevier. Elsevier, 2004, p. 272.

[9] S. Afshar and M. Biscondi, "Intergranular cavitation observed during OFHC copper bicrystal creep," *Scr. Metall.*, vol. 20, no. 5, pp. 707–711, May 1986.

[10] G. H. Edward and M. F. Ashby, "Intergranular fracture during power-law creep," *Acta Metall.*, vol. 27, no. 9, pp. 1505–1518, Sep. 1979.

[11] C. Zener, *The micro mechanismes of fracture*. Americain society for metals (ASM), 1948, pp. 3–31.

[12] M. Tanaka and H. Iizuka, "On the initiation of wedge-type cracks at grain-boundary triple junctions during high-temperature creep," *J. Mater. Sci.*, vol. 20, no. 1, pp. 9–16, Jan. 1985.

[13] J. N. Greenwood, D. . Miller, and J. . Suiter, "Intergranular cavitation in stressed metals," *Acta Metall.*, vol. 2, no. 2, pp. 250–258, Mar. 1954.

[14] I.-W. Chen and A. S. Argon, "Diffusive growth of grain-boundary cavities," *Acta Metall.*, vol. 29, no. 10, pp. 1759–1768, Oct. 1981.

[15] C. Gandhi and R. Raj, "Intergranular fracture in bicrystals—II," *Acta Metall.*, vol. 30, no. 2, pp. 505–511, Feb. 1982.

[1] Reference style : IEEE – Table extracted by Mendeley software

[16] A. Ayensu and T. G. Langdon, “The inter-relationship between grain boundary sliding and cavitation during creep of polycrystalline copper,” *Metall. Mater. Trans. A*, vol. 27, no. 4, pp. 901–907, Apr. 1996.

[17] R. Raj and M. F. Ashby, “Intergranular fracture at elevated temperature,” *Acta Metall.*, vol. 23, no. 6, pp. 653–666, Jun. 1975.

[18] M. H. Yoo and H. Trinkaus, “Crack and cavity nucleation at interfaces during creep,” *Metall. Trans. A*, vol. 14, no. 3, pp. 547–561, Mar. 1983.

[19] B. F. Dyson, “Continuous cavity nucleation and creep fracture,” *Scr. Met. States)*, vol. 17, no. 19, pp. 31–38, 1983.

[20] M. E. Kassner, R. S. Rosen, and G. a. Henshall, “Delayed mechanical failure of silver-interlayer diffusion bonds,” *Metall. Trans. A*, vol. 21, no. 12, pp. 3085–3100, Dec. 1990.

[21] D. Hull and D. E. Rimmer, “The growth of grain-boundary voids under stress,” *Philos. Mag.*, 1959.

[22] M. V. Speight and W. Beere, “Vacancy Potential and Void Growth on Grain Boundaries,” *Met. Sci.*, vol. 9, no. 1, pp. 190–191, Jan. 1975.

[23] J. W. Hancock, “Creep cavitation without a vacancy flux,” *Met. Sci.*, vol. 10, pp. 319–325, 1976.

[24] A. C. F. Cocks and M. F. Ashby, “Intergranular fracture during power-law creep under multiaxial stresses,” *Mater. Sci. Technol.*, vol. 14, no. 8–9, pp. 395–402, 1980.

[25] H. C. Cho, J. Yu, and I. S. Park, “Creep cavitation in a NiCr steel,” *Metall. Trans. A*, vol. 23, no. 1, pp. 201–210, Jan. 1992.

[26] C. T′e-Jer and J. R. Rice, “The shape of intergranular creep cracks gro′ing by surface diffusion,” *Acta Metall.*, vol. 21, no. 12, pp. 1625–1628, Dec. 1973.

[27] F. A. McClintock, “A Criterion for Ductile Fracture by the Growth of Holes,” *J. Appl. Mech.*, vol. 35, no. 2, p. 363, 1968.

[28] B. Budiansky, J. W. Hutchinson, and S. Slutsky, “Void growth and collapse in viscous solids,” *Mechanics of Solids*, vol. 21, no. 4. Pergamon Press, pp. 13–45, 1982.

[29] K. Dzieciol, A. Borbély, F. Sket, A. Isaac, M. Di Michiel, P. Cloetens, T. Buslaps, and A. R. Pyzalla, “Void growth in copper during high-temperature power-law creep,” *Acta Mater.*, vol. 59, no. 2, pp. 671–677, Jan. 2011.

[30] B. Budiansky and O’Connell, “elastic-moduli of a cracked solid,” *Int. J. solids Struct.*, vol. 12, pp. 81–97, 1976.

[31] A. Borbély, F. . Csikor, S. Zabler, P. Cloetens, and H. Biermann, “Three-dimensional characterization of the microstructure of a metal–matrix composite by holotomography,” *Mater. Sci. Eng. A*, vol. 367, no. 1–2, pp. 40–50, Feb. 2004.

[32] M. . Kral and G. Spanos, “Three-dimensional analysis of proeutectoid cementite precipitates,” *Acta Mater.*, vol. 47, no. 2, pp. 711–724, Jan. 1999.

[33] R. . Sidhu and N. Chawla, “Three-dimensional microstructure characterization of Ag3Sn intermetallics in Sn-rich solder by serial sectioning,” *Mater. Charact.*, vol. 52, no. 3, pp. 225–230, Jun. 2004.

[34] P. Clement, J. P. Angeli, and A. Pineau, “SHORT CRACK BEHAVIOUR IN NODULAR CAST IRON,” *Fatigue Fract. Eng. Mater. Struct.*, vol. 7, no. 4, pp. 251–265, Oct. 1984.

[35] M. Herbig, A. King, P. Reischig, H. Proudhon, E. M. Lauridsen, J. Marrow, J.-Y. Buffière, and W. Ludwig, “3-D growth of a short fatigue crack within a polycrystalline microstructure studied using combined diffraction and phase-contrast X-ray tomography,” *Acta Mater.*, vol. 59, no. 2, pp. 590–601, Jan. 2011.

[36] K.-S. Cheong, K. J. Stevens, Y. Suzuki, K. Uesugi, and A. Takeuchi, “The effects of microstructure on creep behaviour—A study through synchrotron X-ray tomography,” *Mater. Sci. Eng. A*, vol. 513–514, pp. 222–227, Jul. 2009.

[37] J. Lambert, A. R. Chambers, I. Sinclair, and S. M. Spearing, “3D damage characterisation and the role of voids in the fatigue of wind turbine blade materials,” *Compos. Sci. Technol.*, vol. 72, no. 2, pp. 337–343, Jan. 2012.

[38] R. Abbasi, L. Renversade, K. Dzieciol, A. Borbély, and A. R. Kaysser-Pyzalla, “Damage fluctuations in creep deformed copper studied with synchrotron X-ray microtomography,” *Int. J. Mater. Res. (formerly Zeitschrift fuer Met.*, vol. 103, no. 02, pp. 228–233, Feb. 2012.

[39] W. Ludwig, A. King, P. Reischig, M. Herbig, E. M. Lauridsen, S. Schmidt, H. Proudhon, S. Forest, P. Cloetens, S. R. Du Roscoat, J. Y. Buffière, T. J. Marrow, and H. F. Poulsen, “New opportunities for 3D materials science of polycrystalline materials at the micrometre lengthscale by combined use of X-ray diffraction and X-ray imaging,” *Mater. Sci. Eng. A*, vol. 524, no. 1–2, pp. 69–76, Oct. 2009.

[40] H. Toda, Z. A. Bin Shamsudin, K. Shimizu, K. Uesugi, A. Takeuchi, Y. Suzuki, M. Nakazawa, Y. Aoki, and M. Kobayashi, “Cavitation during high-temperature deformation in Al–Mg alloys,” *Acta Mater.*, vol. 61, no. 7, pp. 2403–2413, Apr. 2013.

[41] H. F. Poulsen, S. Garbe, T. Lorentzen, D. Juul Jensen, F. W. Poulsen, N. H. Andersen, T. Frello, R. Feidenhans’l, and H. Graafsma, “Applications of high-energy synchrotron radiation for structural studies of polycrystalline materials.,” *J. Synchrotron Radiat.*, vol. 4, no. Pt 3, pp. 147–54, May 1997.

[42] N. Jia, Z. H. Cong, X. Sun, S. Cheng, Z. H. Nie, Y. Ren, P. K. Liaw, and Y. D. Wang, “An in situ high-energy X-ray diffraction study of micromechanical behavior of multiple phases in advanced high-strength steels,” *Acta Mater.*, vol. 57, no. 13, pp. 3965–3977, Aug. 2009.

[43] C. M. Hefferan, J. Lind, S. F. Li, U. Lienert, A. D. Rollett, and R. M. Suter, “Observation of recovery and recrystallization in high-purity aluminum measured with forward modeling analysis of high-energy diffraction microscopy,” *Acta Mater.*, vol. 60, no. 10, pp. 4311–4318, Jun. 2012.

[44] W. Ludwig, P. Reischig, A. King, M. Herbig, E. M. Lauridsen, G. Johnson, T. J. Marrow, and J. Y. Buffière, “Three-dimensional grain mapping by x-ray diffraction contrast

tomography and the use of Friedel pairs in diffraction data analysis.," *Rev. Sci. Instrum.*, vol. 80, no. 3, p. 033905, Mar. 2009.

[45] V. Jantou, M. Turmaine, G. D. West, M. a Horton, and D. W. McComb, "Focused ion beam milling and ultramicrotomy of mineralised ivory dentine for analytical transmission electron microscopy.," *Micron*, vol. 40, no. 4, pp. 495–501, Jun. 2009.

[46] M. K. Miller and R. G. Forbes, "Atom probe tomography," *Mater. Charact.*, vol. 60, no. 6, pp. 461–469, Jun. 2009.

[47] B. H. McCormick, "Brain tissue scanner enables brain microstructure surveys," *Neurocomputing*, vol. 44–46, pp. 1113–1118, Jun. 2002.

[48] R. Marschallinger, "A method for three-dimensional reconstruction of macroscopic features in geological materials," *Comput. Geosci.*, vol. 24, no. 9, pp. 875–883, Nov. 1998.

[49] E. Schroeder-Reiter, F. Pérez-Willard, U. Zeile, and G. Wanner, "Focused ion beam (FIB) combined with high resolution scanning electron microscopy: a promising tool for 3D analysis of chromosome architecture.," *J. Struct. Biol.*, vol. 165, no. 2, pp. 97–106, Feb. 2009.

[50] M. Li, S. Ghosh, O. Richmond, H. Weiland, and T. . Rouns, "Three dimensional characterization and modeling of particle reinforced metal matrix composites: part I," *Mater. Sci. Eng. A*, vol. 265, no. 1–2, pp. 153–173, Jun. 1999.

[51] K. M. Wu and M. Enomoto, "Three-dimensional morphology of degenerate ferrite in an Fe–C–Mo alloy," *Scr. Mater.*, vol. 46, no. 8, pp. 569–574, Apr. 2002.

[52] N. Chawla, V. V. Ganesh, and B. Wunsch, "Three-dimensional (3D) microstructure visualization and finite element modeling of the mechanical behavior of SiC particle reinforced aluminum composites," *Scr. Mater.*, vol. 51, no. 2, pp. 161–165, Jul. 2004.

[53] J. E. Spowart, "Automated serial sectioning for 3-D analysis of microstructures," *Scr. Mater.*, vol. 55, no. 1, pp. 5–10, Jul. 2006.

[54] E. Barry, "Three-dimensional reconstruction of microstructures in α + β Titanium alloys," The Ohio State University, 2008.

[55] W. Hauffe, "Sputtering by particle Bombardment," in in *Topics in Applied Physics*, vol. 64, 1991, pp. 305–338.

[56] Z. Asghar, G. Requena, H. P. Degischer, and P. Cloetens, "Three-dimensional study of Ni aluminides in an AlSi12 alloy by means of light optical and synchrotron microtomography," *Acta Mater.*, vol. 57, no. 14, pp. 4125–4132, Aug. 2009.

[57] A. A. Wahab and M. V. Kral, "3D analysis of creep voids in hydrogen reformer tubes," *Mater. Sci. Eng. A*, vol. 412, no. 1–2, pp. 222–229, Dec. 2005.

[58] D. J. Rowenhorst, A. Gupta, C. R. Feng, and G. Spanos, "3D Crystallographic and morphological analysis of coarse martensite: Combining EBSD and serial sectioning," *Scr. Mater.*, vol. 55, no. 1, pp. 11–16, Jul. 2006.

[59] S. Morito, Y. Edamatsu, K. Ichinotani, T. Ohba, T. Hayashi, Y. Adachi, T. Furuhara, G. Miyamoto, and N. Takayama, "Quantitative analysis of three-dimensional morphology of martensite packets and blocks in iron-carbon-manganese steels," *J. Alloys Compd.*, pp. 2–7, Feb. 2012.

[60] C. Gupta, H. Toda, C. Schlacher, Y. Adachi, P. Mayr, C. Sommitsch, K. Uesugi, Y. Suzuki, A. Takeuchi, and M. Kobayashi, "Study of creep cavitation behavior in tempered martensitic steel using synchrotron micro-tomography and serial sectioning techniques," *Mater. Sci. Eng. A*, vol. 564, pp. 525–538, Mar. 2013.

[61] S. Birosca, J. Y. Buffiere, F. a. Garcia-Pastor, M. Karadge, L. Babout, and M. Preuss, "Three-dimensional characterization of fatigue cracks in Ti-6246 using X-ray tomography and electron backscatter diffraction," *Acta Mater.*, vol. 57, no. 19, pp. 5834–5847, Nov. 2009.

[62] E. Maire, O. Bouaziz, M. Di Michiel, and C. Verdu, "Initiation and growth of damage in a dual-phase steel observed by X-ray microtomography," *Acta Mater.*, vol. 56, no. 18, pp. 4954–4964, Oct. 2008.

[63] L. Babout, E. Maire, and R. Fougères, "Damage initiation in model metallic materials: X-ray tomography and modelling," *Acta Mater.*, vol. 52, no. 8, pp. 2475–2487, May 2004.

[64] J. R. Rice and D. M. Tracey, "On the ductile enlargement of voids in triaxial stress fields∗," *J. Mech. Phys. Solids*, vol. 17, no. 3, pp. 201–217, Jun. 1969.

[65] a. Weck, D. S. Wilkinson, and E. Maire, "Observation of void nucleation, growth and coalescence in a model metal matrix composite using X-ray tomography," *Mater. Sci. Eng. A*, vol. 488, no. 1–2, pp. 435–445, Aug. 2008.

[66] A. Hosokawa, D. S. Wilkinson, J. Kang, and E. Maire, "Effect of triaxiality on void growth and coalescence in model materials investigated by X-ray tomography," *Acta Mater.*, vol. 60, no. 6–7, pp. 2829–2839, Apr. 2012.

[67] A. Pyzalla, B. Camin, T. Buslaps, M. Di Michiel, H. Kaminski, A. Kottar, A. Pernack, and W. Reimers, "Simultaneous tomography and diffraction analysis of creep damage.," *Science*, vol. 308, no. 5718, pp. 92–5, Apr. 2005.

[68] A. Isaac, F. Sket, W. Reimers, B. Camin, G. Sauthoff, and A. R. Pyzalla, "In situ 3D quantification of the evolution of creep cavity size, shape, and spatial orientation using synchrotron X-ray tomography," *Mater. Sci. Eng. A*, vol. 478, no. 1–2, pp. 108–118, Apr. 2008.

[69] A. Isaac, K. Dzieciol, F. Sket, M. di Michiel, T. Buslaps, A. Borbély, and A. R. Pyzalla, "Investigation of creep cavity coalescence in brass by in-situ synchrotron X-Ray microtomography," in *Developments in X-Ray Tomography*, 2008, vol. 7078, p. 70781J–70781J–10.

[70] F. Sket, A. Isaac, K. Dzieciol, G. Sauthoff, A. Borbély, and A. R. Pyzalla, "In situ tomographic investigation of brass during high-temperature creep," *Scr. Mater.*, vol. 59, no. 5, pp. 558–561, Sep. 2008.

[71] F. Sket, K. Dzieciol, A. Isaac, A. Borbély, and A. R. Pyzalla, "Tomographic method for evaluation of apparent activation energy of steady-state creep," *Mater. Sci. Eng. A*, vol. 527, no. 7–8, pp. 2112–2120, Mar. 2010.

[72] H. U. Hong, B. S. Rho, and S. W. Nam, "Correlation of the M23C6 precipitation morphology with grain boundary characteristics in austenitic stainless steel," *Mater. Sci. Eng. A*, vol. 318, no. 1–2, pp. 285–292, Nov. 2001.

[73] A. A. Wahab, C. R. Hutchinson, and M. V. Kral, "A three-dimensional characterization of creep void formation in hydrogen reformer tubes," *Scr. Mater.*, vol. 55, no. 1, pp. 69–73, Jul. 2006.

[74] S. Mahadevan and D. Casasent, "Automated image processing for grain boundary analysis.," *Ultramicroscopy*, vol. 96, no. 2, pp. 153–62, Aug. 2003.

[75] H. J. Frost and M. F. Ashby, *Deformation-mechanism maps: The plasticity and creep of metals and ceramics*, 1st editio. Pergamon Press (Oxford Oxfordshire and New York), 1982, p. 166.

[76] "Components of synchrotron," *Diamond light source*, 2013. [Online]. Available: http://www.diamond.ac.uk/Home/Technology/Components.html.

[77] J. Hsieh, *Computed Tomography: Principles, Design, Artifacts, and Recent Advances*. SPIE Press, 2003, p. 387.

[78] S. W. Smith, "Chapter 25: Special Imaging Techniques," in in *The Scientist and Engineer's Guide to Digital Signal Processing*, California Technical Publishing, 1997.

[79] K. Dzieciol, "Four dimentional characterization of creep cavity growth in copper," Universität Bochum, 2010.

[80] L. Reimer, *Scanning electron microscopy*. Springer, 1998, p. 534.

[81] F. Robaut, F. Brisset, F. Grillon, J. Ruste, and M. Repoux, *Microscopie électronique à balayage et Microanalyses*. EDP Sciences, 2009, p. 892.

[82] H. J. Bunge, *Texture analysis in Materials Science: Mathematical Methods*. Butterworth-Heinemann, 1982, p. 616.

[83] N. C. K. Lassen, "Automatic crystal orientation determination from EBSPs," *Micron Microsc. Acta*, vol. 23, no. 1–2, pp. 191–192, Jan. 1992.

[84] R. Quey, "Orientation Library: A collection of routines for orientation manipulation." 2008.

[85] F. J. Humphreys, P. S. Bate, and P. J. Hurley, "Orientation averaging of electron backscattered diffraction data," *J. Microsc.*, vol. 201, no. 1, pp. 50–58, Jan. 2001.

[86] J. C. Glez and J. Driver, "Orientation distribution analysis in deformed grains," *J. Appl. Crystallogr.*, vol. 34, no. 3, pp. 280–288, May 2001.

[87] E. Schmid and W. Boas, *Kristallplastizität mit Besonderer Berücksichtigung der Metalle*. Springer, 1935.

[88] J. S. Wang, L. Martinez, and W. D. Nix, “A study of intergranular cavity growth controlled by the coupling of diffusion and power law creep,” *Acta Metall.*, vol. 31, no. 6, pp. 873–881, Jun. 1983.

[89] H. Nechad, A. Helmstetter, R. El Guerjouma, and D. Sornette, “Creep Ruptures in Heterogeneous Materials,” *Phys. Rev. Lett.*, vol. 94, no. 4, p. 045501, Jan. 2005.

[90] M. Di Michiel, J. M. Merino, D. Fernandez-Carreiras, T. Buslaps, V. Honkimäki, P. Falus, T. Martins, and O. Svensson, “Fast microtomography using high energy synchrotron radiation,” *Rev. Sci. Instrum.*, vol. 76, no. 4, p. 043702, 2005.

[91] B. Sankur, “Survey over image thresholding techniques and quantitative performance evaluation,” *J. Electron. Imaging*, vol. 13, no. 1, p. 146, Jan. 2004.

[92] E. De Castro and C. Morandi, “Registration of Translated and Rotated Images Using Finite Fourier Transforms,” *IEEE Trans. Pattern Anal. Mach. Intell.*, vol. PAMI-9, no. 5, pp. 700–703, Sep. 1987.

[93] A. Isaac, K. Dzieciol, F. Sket, and A. Borbély, “In-Situ Microtomographic Characterization of Single-Cavity Growth During High-Temperature Creep of Leaded Brass,” *Metall. Mater. Trans. A*, vol. 42, no. 10, pp. 3022–3030, Jul. 2011.

[94] A. Pyzalla, B. Camin, B. Lehrer, M. Wichert, A. Koch, K. Zimnik, E. Boller, and W. Reimers, “In-situ observation of creep damage in Al-Al2O3 MMCs by synchrotron X-ray tomography,” in *International Centre for Diffraction Data*, 2006, pp. 73–78.

[95] E. Maire, V. Carmona, J. Courbon, and W. Ludwig, “Fast X-ray tomography and acoustic emission study of damage in metals during continuous tensile tests,” *Acta Mater.*, vol. 55, no. 20, pp. 6806–6815, Dec. 2007.

[96] L. Babout, E. Maire, J. Y. Buffière, and R. Fougères, “Characterization by X-ray computed tomography of decohesion, porosity growth and coalescence in model metal matrix composites,” *Acta Mater.*, vol. 49, no. 11, pp. 2055–2063, Jun. 2001.

[97] M. Li, S. Ghosh, T. N. Rouns, H. Weiland, O. Richmond, and W. Hunt, “Serial Sectioning Method in the Construction of 3-D Microstructures for Particle-Reinforced MMCs,” *Mater. Charact.*, vol. 41, no. 2–3, pp. 81–95, Aug. 1998.

[98] M. A. Wall, A. J. Schwartz, and L. Nguyen, “A high-resolution serial sectioning specimen preparation technique for application to electron backscatter diffraction,” *Ultramicroscopy*, vol. 88, no. 2, pp. 73–83, Jul. 2001.

[99] X. Zhao, Y. Yin, B. Yang, B. Zhu, and X. Tian, “Level set and geodesic active contours based measurement of material removal between serial sections,” *Comput. Mater. Sci.*, vol. 39, no. 4, pp. 857–861, Jun. 2007.

[100] S. Raghavan, M. Keswani, and R. Jia, “Particulate Science and Technology in the Engineering of Slurries for Chemical Mechanical Planarization,” *KONA powder Part. J.*, vol. 26, pp. 94–105, 2008.

[101] K. Dzieciol, “Pmeter: Automated alignement of topography maps.” 2012.

[102] Vsg Avizo, “Avizo Analysis Software for Scientific and Industrial Data,” 2013. [Online]. Available: http://www.vsg3d.com/avizo/overview.

[103] A. Borbély, C. Maurice, and J. H. Driver, “Rotation axis analysis of deformed crystals by X-rays and electrons,” *J. Appl. Crystallogr.*, vol. 41, no. 4, pp. 747–753, Jun. 2008.

[104] J. Weertman, “Theory of Steady-State Creep Based on Dislocation Climb,” *J. Appl. Phys.*, vol. 26, no. 10, p. 1213, 1955.

[105] B. M. Patterson, J. P. Escobedo-Diaz, D. Dennis-Koller, and E. Cerreta, “Dimensional quantification of embedded voids or objects in three dimensions using X-ray tomography.,” *Microsc. Microanal.*, vol. 18, no. 2, pp. 390–8, Apr. 2012.

[106] T. G. Langdon, “Grain boundary sliding revisited: Developments in sliding over four decades,” *J. Mater. Sci.*, vol. 41, no. 3, pp. 597–609, Feb. 2006.

École Nationale Supérieure des Mines
de Saint-Étienne

NNT : 2013 EMSE 0706

Kévin ABBASI

X-RAY TOMOGRAPHY AND SERIAL SECTIONING INVESTIGATION OF CREEP DAMAGE IN COPPER

Speciality : Materials science

Keywords : X-ray tomography, Creep, Damage, Serial sectioning, EBSD

Abstract :

Power law creep damage is one of the most intriguing unsolved phenomena of materials science. Models based on continuum mechanics generally predict a much higher strain to failure, as well as a much longer creep lifetime than experimentally observed values. This thesis highlights two aspects of this problematic by analyzing creep damage in copper using in situ synchrotron tomography and 3D reconstruction of the damaged polycrystal structure by serial sectioning.

Damage in terms of the area fraction of voids was first identified in slices of tomographic reconstructions of creep deformed copper. The local and global evolution of cavities area fraction was checked against the Cocks and Ashby model and it was found that the model overestimates creep lifetime and underestimates damage development. The importance of the initial damage heterogeneity and the role of damage localization are also emphasized. It was found that the amplitude of the largest damage fluctuation increases parabolically as a function of cavity's mean area fraction.

An improved serial sectioning method based on surface profilometry was developed, which allows the accurate measurement of the removed local material thickness. The 3D reconstructions enabled identifying the creep voids and the grains of the polycrystal. It was shown that with the exception of the void shape, the relationship between void location at a given grain boundary and crystallographic orientation of the neighbor grains is similar in samples deformed by different creep mechanisms. The relative population of creep voids is higher at simple grain boundaries than at triple junctions. Voids found at a triple boundary, however, are larger.

École Nationale Supérieure des Mines
de Saint-Étienne

NNT : 2013 EMSE 0706

Kévin ABBASI

ETUDE DE L'ENDOMMAGEMENT EN FLUAGE DE CUIVRE PAR TOMOGRAPHIE A RAYONS X ET POLISSAGES SUCCESSIFS

Spécialité: Sciences et génie des matériaux

Mots clefs : Tomographie à rayons X, Fluage, Endommagement, Sectionnement sérielle, EBSD

Résumé :

Les modèles basés sur la mécanique des milieux continus prévoient généralement une déformation à la rupture plus élevée, ainsi qu'une durée de vie en fluage beaucoup plus longue que les valeurs observées expérimentalement. Cette thèse met en évidence deux aspects de cette problématique en analysant l'endommagement à l'aide de tomographie in situ à rayons X de synchrotron et reconstruction 3D de la structure polycristalline par polissages successifs.

L'endommagement en termes de fraction surfacique des cavités a été identifié dans les couches de reconstructions tomographiques perpendiculairement à l'axe de déformation. L'évolution de la fraction surfacique des cavités a été comparée avec le modèle de prédiction de Cocks et Ashby. Ce dernier surestime la durée de vie en fluage et sous-estime l'état de l'endommagement. L'importance de l'hétérogénéité initiale de l'endommagement et l'effet de localisation de l'endommagement est également souligné. L'amplitude de la plus grande fluctuation surfacique augmente de façon parabolique en fonction de la fraction surfacique moyenne.

Une méthode de sectionnement sériel améliorée basée sur la profilométrie de surface a été développée. Elle permet la mesure précise de l'épaisseur du matériau enlevée localement. Les analyses ont montré que l'emplacement des cavités par rapport aux joints de grains et l'orientation cristallographique des grains au voisinage est similaire pour les échantillons déformé par différents mécanismes de fluage. La population relative des cavités de fluage présente aux joints de grains simples est supérieure à celle présente aux joints triples. Les cavités trouvées aux joints triples, cependant, sont plus grandes.